Mass accretion rate fluctuations in black hole X-ray binaries

Rapisarda, S.

Publication date
2017
Document Version
Final published version
License
Other

Mass accretion rate fluctuations in Black Hole X-ray Binaries

ACADEMISCH PROEFSCHRIFT

ter verkrijging van de graad van doctor
aan de Universiteit van Amsterdam
op gezag van de Rector Magnificus
Prof. dr. ir. K.I.J. Maex
ten overstaan van een door het College voor Promoties ingestelde
commissie, in het openbaar te verdedigen in de Agnietenkapel
op woensdag 28 juni 2017, te 10:00 uur

door

Stefano Rapisarda

geboren te Catania, Italië

Promotiecommissie:

Promotor:	Prof. dr. M. B. M. van der Klis	University of Amsterdam
Copromotor:	dr. A. R. Ingram	University of Amsterdam
Overige leden:	Prof. dr. W. Hermsen	University of Amsterdam
	Prof. dr. R. A. M. J. Wijers	University of Amsterdam
	Prof. dr. S. B. Markoff	University of Amsterdam
	Prof. dr. R. M. Mendez	University of Groningen
	dr. P. Uttley	University of Amsterdam

Faculteit der Natuurwetenschappen, Wiskunde en Informatica

The research described in this thesis was supported by the Netherlands Organisation for Scientific Research (NWO) and carried out at the Anton Pannekoek Institute for Astronomy (API), University of Amsterdam.

Cover: *Tentative Ripple* by Jan Fordyce

Contents

1 Introduction

I

X-ray binaries are unique laboratories in which to study the physics of matter in extreme conditions. A neutron star has a density similar to that of an atomic nucleus, it can have strong magnetic fields, and the gravitational acceleration at its surface is $\sim 10^{12}$ m/s^2. In a stellar mass black hole, several solar masses (> 3 M$_\odot$) are concentrated in a single point (the gravitational singularity) preventing information from escaping a virtual boundary called the event horizon (the locus of points at which even light cannot escape). If the black hole rotates, it drags the spacetime around it causing tilted orbits to precess (Lense-Thirring effect). Ultra-dense matter, strong magnetic fields, distorted spacetime; such extreme conditions are impossible to reproduce in any laboratory on Earth.

These Compact Objects (neutron stars and black holes) are elusive inhabitants of our Universe (their radius is of the order of a few tens of km), however, their compactness makes *accretion* a highly efficient mechanism to produce high-energy radiation. When a neutron star or a black hole has a companion star, under certain conditions, it can accrete material from it. The material falling onto the compact object emits X-ray radiation and acts as a tracer for the properties of the spacetime around the object and for the properties of the object itself. Despite their compactness and their distance, the large amount of gravitational potential energy converted into radiation makes these compact objects detectable by our satellites and identifiable as the primary component of an *X-ray binary* (the luminosity of an X-ray binary can be $\sim 10^4$ times larger than the total energy output of the Sun). The analysis of this X-ray radiation can give important clues about the behavior of matter in extreme conditions and, ultimately, about the fundamental laws of physics, including general relativity and quantum mechanics.

This challenging purpose requires a detailed characterization of the accretion flow, i.e. of how the matter that has been torn off the companion star accretes onto the compact object. This requires determination of the flow geometry, the heating and cooling mechanisms in the accreting plasma, the role of magnetic fields in the flow, the flow boundary conditions, etc...

from the mere count of X-ray photons: an enormous challenge. In last 45 years, astronomers intensively studied the puzzling phenomenology of X-ray binaries. However, there still does not exist a self-consistent model for accretion onto compact objects able to describe all the complex X-ray binary phenomenology.
In this thesis I focus on the simplest case of accretion: black hole X-ray binaries. Black holes do not possess a solid surface (like neutron stars), so that material falls onto them without interacting with any barrier. In particular, I focus on modelling the short timescale variability ($\approx$ 0.01-100 s) that carries information about the regions that are closest to the black hole. For studying this variability, we applied for the first time systematically and quantitatively the hypothesis of *propagating mass accretion rate fluctuations* in the accretion flow. This hypothesis was first proposed by Lyubarskii (1997) and rapidly became popular in the X-ray binary community as one of the best physical scenarios for consistently explaining many of the observational properties of these systems. Verifying the applicability of this hypothesis to X-ray binary observations represents a very important step towards a global understanding of these systems.
In the following sections of this introduction, I briefly describe black hole X-ray binaries, the techniques used to study X-ray radiation, their phenomenology, and the propagating mass accretion rate fluctuations scenario.

1.1 Black Hole X-ray Binaries

A stellar mass Black Hole (BH) is a compact object resulting from the gravitational collapse of a massive star. A *Black Hole X-ray Binary* (BHB) is a system consisting of a BH and a star orbiting around it. Eventually, because of either the evolution of the companion star or the decrease of the orbital separation between the two objects, the BH accretes material from the companion. The mode of the mass transfer depends both on the mass ratio between the BH and the companion star and on the orbital separation between the components of the system. If the companion is a massive star ($\geq$ 10 $M_{\odot}$, e.g an O/B star), it can lose material in the form of strong stellar wind that then accretes onto the BH. In this case, the system is called *High-Mass X-ray Binary* (HMXB). If the mass of the companion is smaller than the BH mass ($\sim$ 1 $M_{\odot}$) and the companion fills its Roche lobe, the material flows through the inner Lagrangian point (L1) towards the BH. In this case, the system is called *Low-Mass X-ray Binary* (LMXB).
In these accreting systems, the material has enough angular momentum to not fall directly onto the BH, forming an *accretion disc* around the BH. Because of viscosity mechanisms, the angular momentum in the disc is transported outwards from the inner regions, so that the matter moves to closer and closer orbits until it finally accretes onto the BH. A mass m moving from very large radii to a certain radius r around the BH experiences a variation of gravitational potential energy $\Delta E = G\mathrm{M_{BH}}m/r$. For Keplerian rotation, the kinetic energy of the mass m is $E_{kin} = 1/2 \quad mv_{kep}^2 = 1/2 \quad mG\mathrm{M_{BH}}/r$. This means that, when material

Figure 1.1: Artistic impression of an accretion disc. Credit: Gabriel Pérez, SMM (IAC)

accretes, half of its potential energy is converted into kinetic energy (its rotational speed increases towards the BH) and the other half is available to be radiated. If this entire half is radiated, the luminosity of a disc extending from very large radii to the radius r is:

$$L = \frac{1}{2}\frac{G\mathrm{M_{BH}}\dot{m}}{r} \tag{1.1}$$

The disc luminosity depends both on the mass of the central object $\mathrm{M_{BH}}$, on the *mass accretion rate* $\dot{m}$, and on the radius r. The energy released per unit area, and because of this the temperature of the disc plasma and the emission, all increase towards the BH. In the inner part of the disc the temperature is $\sim 10^7$ K, so that the radiation emitted is in the X-ray band. Disc instabilities on large length scales cause long timescale variations ($\sim$ days-months) in the observed X-ray flux. Local fluctuations in the mass accretion rate are supposed to be responsible for much of the observed short timescale variability ($\approx$ 0.01-100 s). Fig. 1.1 shows an artistic representation of an accretion disc.
The position of BHBs in the galaxy follows the nature of the companion: in HMXBs the companion is a young star, so these systems are concentrated in the galactic plane and in the arms of the Galaxy. LMXBs have much older companions, so they are found mainly in the galactic bulge and in globular clusters.

1.2 Instrumentation

X-ray photons coming from space are absorbed by the Earth's atmosphere. In order to collect X-ray photons, the detectors are placed at high altitude by balloons, sounding rockets, and satellites. Since the discovery of the first cosmic X-ray sources in the 60's, more and more

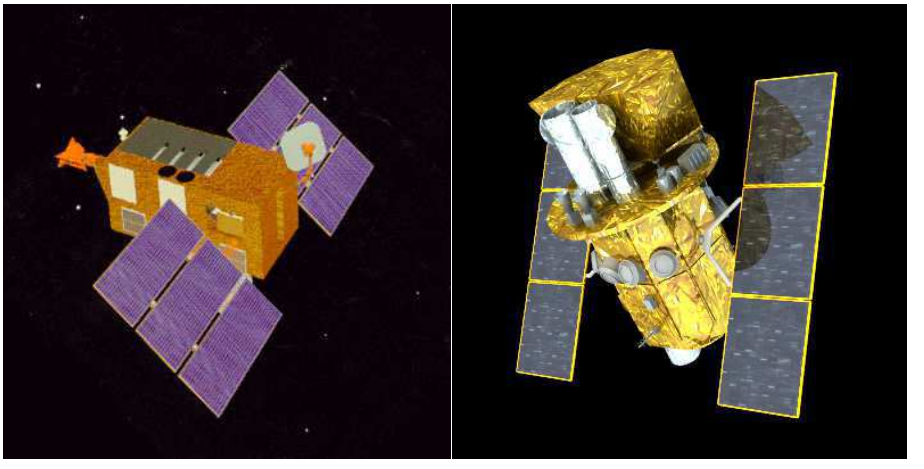

Figure 1.2: The Rossi X-ray Timing Explorer (left) and the Swift Gamma-Ray Burst Mission (right)

sophisticated instruments have been sent into space to investigate high energy phenomena. In this thesis we used archival data from two of them: the *Rossi X-ray Timing Explorer* (RXTE) and the *Swift Gamma-Ray Burst Mission* (*Swift*). In the following sections we briefly summarize the characteristics of these two instruments.

1.2.1 RXTE

The *Rossi X-ray Timing Explorer* (RXTE, Bradt et al. 1993, Fig. 1.2) was launched on December 30, 1995 and decommissioned on January 5, 2012. On board of the satellite there were two pointed instruments, the *Proportional Counter Array* (PCA, Jahoda et al. 1996) and the *High Energy X-ray Timing Experiment* (HEXTE, Rothschild et al. 1998). A third instrument, the *All-Sky Monitor* (ASM, Levine et al. 1996) could scan 80% of the sky every orbit of the satellite and was used to locate X-ray outbursts.
In this thesis we used data from the PCA. The PCA consisted of an array of five identical proportional counter units (PCUs). The PCUs were sensitive in the 2-60 keV energy range with a combined effective area of ≈ 6500 cm^2. The field of view of the instrument was ≈ 1 degree, the energy resolution was $\approx 18\%$ at 6 keV, and the time resolution was ≈ 1 μs.
During the 17 years that RXTE was operational, because of component degradation and impact of micro-meteorites on the detectors, the technical capabilities of the PCA diminished. Partly in order to compensate for this, the PCU gain was readjusted several times. From the launch of the satellite to the decommissioning date, 5 different gain epochs have been defined separated by gain adjustments. In the analysis of data spanning different gain epochs, the associated changes in instrumental response must be taken into account.

1.2.2 Swift

The *Swift Gamma-Ray Burst Mission* (Gehrels et al. 2004, Fig. 1.2) was conceived as a multi-wavelength observatory dedicated to the study of gamma-ray bursts. However, *Swift* data were remarkably useful also in the study of X-ray binaries. *Swift* was launched on November 20, 2004 and, at the time of writing, it is still operating. On board of the satellite there are three instruments: the *Burst Alert Telescope* (BAT), the *Ultraviolet/Optical Telescope* (UVOT), and the *X-ray Telescope* (XRT).
In this thesis, we used data from the XRT (Burrows et al. 2005). The XRT is a focusing X-ray telescope that is sensitive in the 0.2-10 keV range. X-ray photons are focused onto and collected by a CCD detector (600 x 602 pixels). The effective area of the instrument is 110 cm^2, the field of view is 23.6 x 23.6 arcmin, and the resolution is 18 arcsec.
The XRT can operate in different modes. In this thesis we analyzed data collected in the Windowed Timing mode (WT), conceived to perform timing analysis with an imaging instrument. In this mode the field of view is restricted to the central 8 arcmin and the 2D picture collected by the CCD is "squeezed" in a single 1D strip of data. In this mode most spatial information is lost, however the settings described above allow to obtain a shorter read-out time compared to other modes and therefore a higher time resolution which in this mode is improved to $\approx$ 1.7 ms.

1.3 Techniques

The region emitting X-ray photons in a BHB is too small to be resolved with telescopes. The most effective way to study these objects is to measure with a counting detector arrival time and energy of photons, i.e. to analyze time series (or light curves) in different energy bands and, averaging the counts over different time intervals, energy spectra.
Flux variations on different time scales can be interpreted in terms of changes in the geometry and other properties of the accreting flow. In particular, the short time scale (or rapid) variability ($\approx$ 0.01-100 s) is thought to originate in a region close to the BH and is a fundamental element to track and investigate the physical changes of the accreting system. The amplitude of the rapid variability is usually few percent of the total flux and it is affected by Poisson counting noise so that high count rate data are necessary to properly characterize such variability. The rapid variability is a stochastic process, so we are more interested in average properties than in a single realization of the process.
Fourier analysis represents a fundamental tool to study the properties of the rapid variability (van der Klis 1989). Switching from time to frequency domain, it is possible to measure the average properties of the signal of the source above the counting noise. In the following sections I describe the Fourier products computed and analyzed in this thesis: the Power Spectrum, the Cross-Spectrum, and the Coherence.

1.3.1 Power Spectrum

In our analysis, a light curve $x(t)$ is divided into different contiguous segments of identical length ($x_i(t)$, see Fig. 1.3 left-top panel). The Fourier transform is applied to each segment using the Fast Fourier Transform algorithm (FFT, e.g. Press et al. 1992). In this way we switch from the time to the frequency domain ($x_i(t) \Rightarrow X_i(\nu)$; we follow the convention that uppercase symbols represent the Fourier transform of the corresponding lowercase symbols). The length of the segments T determines the lowest frequency that can be observed and the frequency resolution: $\delta\nu = 1/T$. The highest observable frequency is called Nyquist frequency ($\nu_{\rm Ny}$) and it depends on the time resolution of the light curve δt: $\nu_{\rm Ny} = 1/2\delta t$. It follows that for investigating high- and low-frequency variability we need high resolution data and long light curve segments, respectively.

The *power spectrum* is the squared modulus of the computed complex Fourier amplitudes ($P_i(\nu) = |X_i(\nu)|^2 = X_i^*(\nu)X_i(\nu)$, where $*$ denotes complex conjugation). We normalize the power spectrum by a factor $2/X_i(\nu_0)$, where $X_i(\nu_0)$ is the zero-frequency component. $X_i(\nu_0)$ is a real number and it is equal to the total number of photons detected in the light curve segment $x_i(t)$. This normalization is called *Leahy normalization* (Leahy et al. 1983). After normalization, we have a number of Leahy normalized power spectra equal to the initial number of light curve segments. We average the power spectra $P_i(\nu)$ obtaining a single power spectrum $P(\nu)$; we can also average over the logarithmically spaced frequency bins of this total power. Using the Leahy normalization, the Poisson noise level of the average power spectrum $P(\nu)$ is ≈ 2 (see Fig. 1.3 bottom-left panel). If all variability in the light curves is stochastic, and the number of averaged power spectra times the number of averaged frequency bins is large enough, the uncertainties will be Gaussian with relative error $\sigma_P/P = 1/\sqrt{NB}$, where N is the number of power spectra averaged and B the number of consecutive frequency bins averaged. Finally, we apply the *fractional root-mean-square (rms) normalization* multiplying the Leahy-normalized noise-subtracted power spectrum by $(total\ counts)/(source\ counts)^2$. With this normalization the integral of the power spectrum over all the frequencies is equal to the $fractional\ rms$ of the initial light curve (see Fig. 1.3 bottom-right panel).

Looking at the power spectrum, we can recognize different structures or features (Fig. 1.3 bottom panels). Peaked features are called *quasi-periodic oscillations* (QPOs) and features spread over several decades in frequency are called broad band noise. The power spectral features observed in BHBs can be quantified fitting the power spectrum with several Lorentzians (see Nowak 2000; Belloni, Psaltis & van der Klis 2002 for details). Considering the centroid frequency ν_0 and the half width at half maximum Δ of the Lorentzian, we can define a maximum frequency $\nu_{max} = \sqrt{\nu_0^2 + \Delta^2}$ and a quality factor $Q = \nu_0/2\Delta$. ν_{max} is the frequency at which the component contributes most of its power per logarithmic frequency interval and Q is useful to quantitatively distinguish between QPOs (by convention, $Q > 2$) and broad band noise ($Q < 2$).

In this thesis, the computed rms-normalized power spectra are plotted on a logarithmic scale

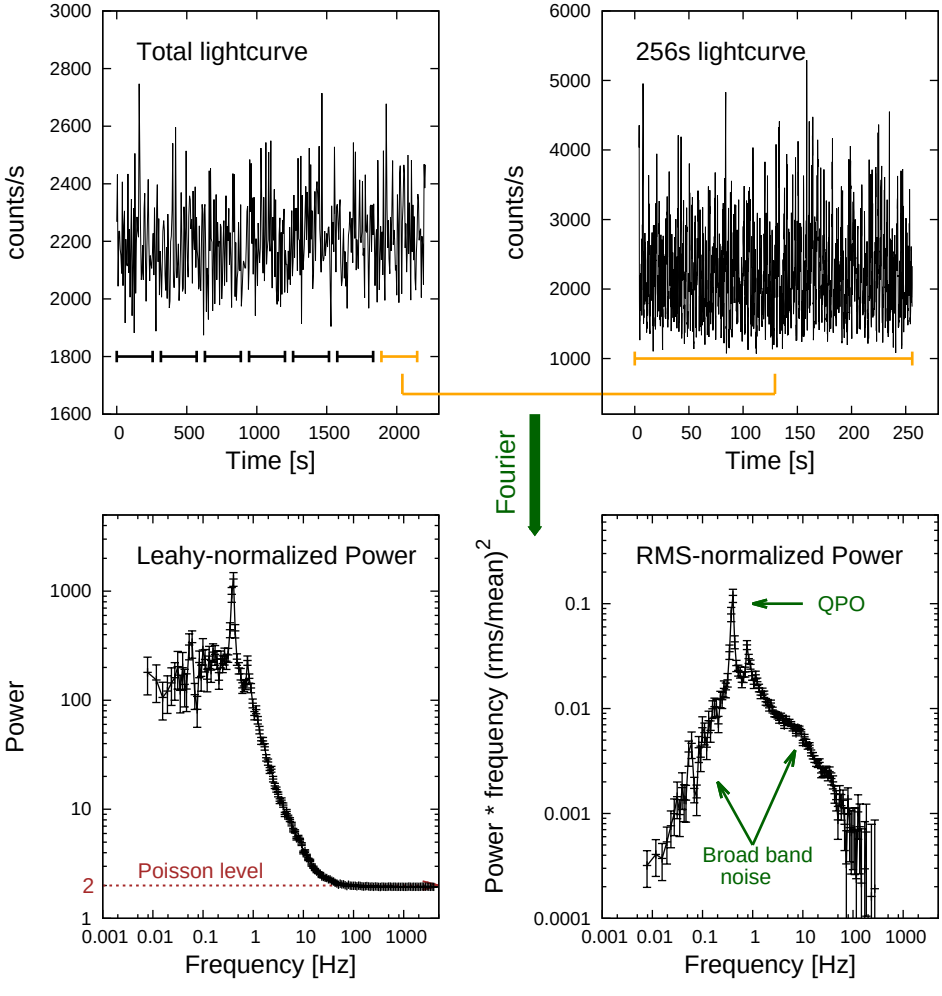

Figure 1.3: These four plots show the steps we followed in our analysis for computing the Power Spectrum. We divide a light curve into a number of contiguous segments (in this case, 7 segments of 256s). From each segment we compute a Leahy-normalized power spectrum. We see that the Poisson noise level is ≈ 2. We average the powers, we subtract the Poisson noise, and we finally apply the fractional rms normalization. We plot the power spectrum in the $\nu P(\nu)$ representation in order to visually estimate more easily the rms distribution.

and in the Power*Frequency [(rms/mean)^2] representation. Using this convention, we can have a more immediate idea of the rms contribution at each frequency. In this representation, in Log-Log plots, Lorentzian functions are symmetric around ν_{max} and their amplitude can be expressed in terms of fractional rms (%).

1.3.2 Cross-spectrum and phase lag

The *cross-spectrum* is a useful tool to determine the relation between two simultaneous time series (e.g. collected from two different energy bands at the same time).

If we observe statistically significant features at the same frequency in two different power spectra, it is important to understand and quantify if these features are related to one another and, if this is the case, which is the kind of relation between the two. Computing the *cross-correlation* of two time series ($c(t)$), we can quantify to what degree the two series are *correlated*: we can measure their correlation as a function of the phase shift between the two. If we consider two time series $x_1(t)$ and $x_2(t)$, the Fourier transform of the cross-correlation between the two is $C(\nu) = X_1(\nu)^* X_2(\nu)$. This is the *cross-spectrum* between $x_1(t)$ and $x_2(t)$. $C(\nu)$ is a complex quantity and the cross-spectral amplitude (or simply cross-amplitude) is $A(\nu) = \sqrt{\mathrm{Re}[C(\nu)]^2 + \mathrm{Im}[C(\nu)]^2}$. The argument of the cross-spectrum is the *phase lag* between the two time series ($\phi = \arctan\{\mathrm{Im}[C(\nu)]/\,\mathrm{Re}[C(\nu\}$). The real part of the cross-spectrum is the in-phase signal, while the imaginary part is the π/2 out-of-phase signal. When $\mathrm{Im}[C(\nu)]$ is zero, there is no lag or a lag of $n\pi$ (where n is a positive integer).

In this thesis, we computed cross-spectra considering simultaneous light curves in two energy bands (soft and hard band). We conducted the same ensemble averaging and rebinning procedure described in the previous section for the case of the power spectrum. The details of the normalizations we applied to the cross-spectrum are described in Chapter 3.

1.3.3 Coherence

The *coherence* is a measure of the degree of *linear* correlation between two time series. Considering two processes producing two different time series $x_1(t)$ and $x_2(t)$ (realizations of the processes), the coherence function is defined in the following way (Vaughan & Nowak 1997):

$$\gamma^2(\nu) = \frac{|\langle C(\nu)\rangle|^2}{\langle |X_1(\nu)|^2\rangle \langle |X_2(\nu)|^2\rangle} \tag{1.2}$$

The angle brackets indicate an average over many realizations (in our case, light curve segments). The coherence depends both on the cross-spectrum between the two time series $C(\nu)$ and on the power spectra of the two series, $|X_1(\nu)|^2$ and $|X_2(\nu)|^2$.

As expressed in Eq. 1.2, the coherence is computed on averaged quantities. If two time series are perfectly coherent, the phase difference between their Fourier amplitudes will be always the same for every realization of the two processes. In this case $|\langle C(\nu)\rangle|^2 =$

$\langle |X_1(\nu)|^2 \rangle \langle |X_2(\nu)|^2 \rangle$ and the coherence $\gamma^2(\nu) = 1$. If the phase difference is uniformly and randomly distributed for every realization of the two processes, the time series are uncorrelated ($\langle C(\nu) \rangle = 0$) and therefore also incoherent ($\gamma^2(\nu) = 0$).

1.4 LMXB phenomenology

X-ray astronomy is a relatively young research field. The first cosmic X-ray sources were discovered in the 60's and were intensively studied only in the last decades. Thanks to missions like the *XMM-Newton observatory*, the *INTEGRAL* satellite, the *Chandra observatory*, *Swift*, and RXTE, we now have a large amount of data describing BHB phenomenology. The purpose of the following sections is giving a general overview of the main observable characteristics of these systems.

1.4.1 Persistent and transient

BHBs can be divided in *persistent* and *transient* sources. In persistent sources, the X-ray emission is always detected, but it generally shows variations in both luminosity and photon energy distribution. Transient sources spend most of the time in *quiescence*, when their X-ray luminosity is very low. In most cases, the system discovery occurs only when the transient goes into *outburst*, increasing its X-ray luminosity by several orders of magnitude on a time scale of days. At this point, the source becomes easily detectable by our instruments and is identified as an X-ray transient. On a time scale of weeks/months, the transient goes back to quiescence.
Once identified, it is possible to observe BHBs with optical telescopes. If the companion emission is not too weak, one can measure the mass function of the system and so a lower limit to the compact object mass. If this limit is larger than 3 $M_\odot$, the compact object is identified as a BH. When the companion is too faint, but the source shows the observational characteristics of a BHB, the compact object is identified as a BH candidate. In this thesis we analyzed the behavior of 3 transients (MAXI J1543-564, hosting a BH candidate; MAXI J1659-152 and XTE J1550-564, hosting BHs) and one persistent source (Cygnus X-1, hosting a BH).

1.4.2 Canonical states and spectral emission

During an outburst, different BHBs show a similar behavior. The detailed properties of the sources differ from one another in terms of luminosity, spectral energy distribution, and variability, but for all of them it is possible to identify general *states* with specific spectral and timing characteristics (e.g. Tananbaum et al. 1972; Miyamoto et al. 1993; Nowak 1995; Homan et al. 2001; Belloni et al. 2005; Remillard & McClintock 2006; Belloni 2010; Gilfanov 2010; Done 2010). A typical outburst usually begins in the *low-hard state* (LHS). In this state the luminosity is still low, but rapidly increasing. The energy spectrum is hard, i.e.

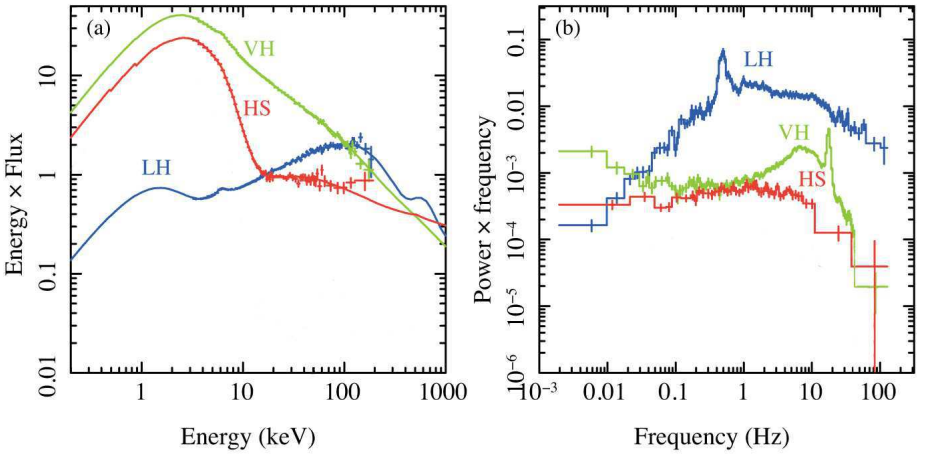

Figure 1.4: Different spectral state energy spectra (a) and corresponding characteristic power spectra (b). The blue line corresponds to the Low-Hard State, the red line to the High-Soft State, and the green line to the Very-High State (from Done 2010).

dominated by a power law with photon index $\Gamma \approx 1.5$ and a cut-off at ≈ 100 keV. At high luminosity, the source is in the *high-soft state* (HSS). The energy spectrum in the HSS is dominated by a thermal component peaking at ≈ 1 keV. At the end of the outburst, the source usually returns to the LHS. The source can also show states with properties in between the ones I just described. The *intermediate state* (IMS) is similar to the LHS but with a stronger thermal component in the energy spectrum (Ebisawa et a. 1994; Belloni et al. 1996) and luminosity sometimes higher than the HSS. In some cases, the source is observed in a *very high state* (VHS, Miyamoto et al. 1991). This state is characterized by high luminosity and an energy spectrum with both a strong thermal component and a (soft) power law ($\Gamma \approx 2.5$). Fig. 1.4(a) shows different spectral distributions in different states.

State transitions indicate physical changes in the structure of the accretion flow, so it is very important to systematically study the differences and similarities between outbursts of the same, and of different sources. An effective way to display the evolution of an outburst is plotting the observations in a *hardness-intensity diagram* (HID). Hardness is defined as the count ratio between a hard and a soft energy band (e.g. 16-20/2-6 keV). If the spectrum of the source is dominated by the soft thermal component, it occupies the left region of the HID. On the other hand, if the energy spectrum is dominated by the hard non-thermal component, it is located on the right side of the HID. When the two components coexist, the source occupies intermediate positions. A "complete" outburst usually follows a "q" shape in the diagram: from LHS (lower-right corner of the diagram) the luminosity rapidly increases, so the source moves to the upper region of the diagram. As luminosity increases, the emission

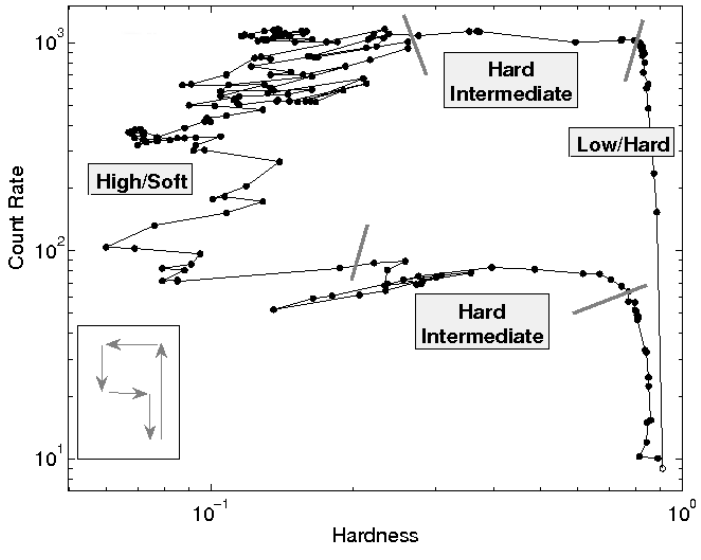

Figure 1.5: Evolution of a BHB outburst represented in the Hardness-Intensity diagram (from Belloni 2010).

becomes softer, so the source moves to the left region of the diagram, toward the HSS. In the final phase of the outburst, the luminosity decreases and then the emission hardens again; the source is back to the LHS. Fig. 1.5 shows the evolution in the HID of an outburst of GX 339-4 that took place in 2006. This source is often used as a prototype of transient BHB behavior. Despite this similar behavior, we note that different sources can show just some of the states described here, transit from one state to another and back several times, enter the same state with different luminosities (*hysteresis*), and show "failed" or "incomplete" outbursts (Tetarenko et al. 2016). Recent studies have shown that the HID shape depends on the inclination of the source (Munoz-Darias et al. 2013).

Different spectral states can be characterized by radio emission associated with the presence of a jet (e.g. Fender, Belloni & Gallo 2004). Steady radio emission is observed in the LHS. In the transition from LHS to HSS, a radio outburst can be observed. After that, the radio emission becomes undetectable until the source goes back to the LHS.

In addition to thermal and non-thermal components, energy spectra of BHBs show characteristic reflection features. These features are the result of hard photons reprocessed in and re-emitted from the disc (the "reflector"). This process produces a fluorescent Kα Fe line at 6.4 keV, an Fe K-edge at 7.1 keV, and a "hump" above $\approx$ 20 keV (e.g. George & Fabian 1991; Gilfanov et al. 2000). The amplitude of the reflection features is correlated with the slope of the power law describing the hard radiation incident on the disc (Zdziarski, Lubinski

& Smith 1999).

1.4.3 Rapid variability

The spectral states described in the previous section are also characterized by very different rapid variability (see Fig. 1.4*b*). The timing characteristics of the source are also used to better define states and state transitions (e.g. Tananbaum et al. 1972; van der Klis et al. 1987a; Miyamoto et al. 1993; Nowak 1995; Homan et al. 2001; Pottschmidt et al. 2003; Fender et al. 2009; Belloni 2010). In the LHS, we observe broad band noise with $\approx 30\%$ fractional rms amplitude and narrow QPOs with frequency between ≈ 0.1 and 15 Hz. As the spectrum becomes softer, all the characteristic frequencies of the power spectral features increase in correlation, while their amplitudes decrease. In particular, the QPO frequency is correlated with the low frequency break of the broad band noise (Wijnands & van der Klis 1998). In the HSS the observed noise is weak (few %) and QPOs are rarely observed.
BHBs show also a time lag between the soft and hard band (e.g. Nolan et al. 1981; van der Klis et al. 1987b; Miyamoto & Kitamoto 1989; Maccarrone, Coppi & Poutanen 2000). Usually the hard emission lags the soft emission. The time lag is both frequency and energy dependent, with an approximately logarithmic relation between lag amplitude and energy separation.
Another important element in this puzzling phenomenology is the *linear* relation between the amplitude of the fluctuations at different time scales and the count rate (Uttley & McHardy 2001; Uttley, McHardy & Vaughan 2005; Heil, Vaughan & Uttley 2012). This means that the amplitude of the rapid variability is correlated with much slower flux variations. This relation is an important element for modeling the rapid variability, in particular it rules out models producing the variability through addition of independent stochastic shots.

1.5 Modelling

At present, there is no self-consistent global theory of accretion onto a BH (and, more in general, onto a compact object). The main challenge is reproducing self-consistently the variations observed on long time scales (light curve and spectral states during an outburst) and the rapid variability characteristics. Thanks to the large amount of observations collected in the last decades, it was possible to identify the main emission mechanisms that are responsible for the observed energy spectrum. Emission mechanisms such as blackbody emission, Comptonization, pair production, fluorescence, all play a role. However, studying stochastic processes is a different challenge. Understanding the origin of the rapid variability is fundamental for validating any model used to explain the energy spectral behavior of the source and, in general, for studying the geometry of the accreting system. In the following sections, we summarise the latest and main achievements in the energy spectral and rapid variability modeling.

1.5.1 Energy spectra

From BHB phenomenology we know that the energy spectrum is characterized by a thermal and a non-thermal component that becomes more or less dominant at different luminosities, depending on the spectral state of the system. The details about how the gravitational potential energy is dissipated in the regions producing such emission are still not well defined. However, the origin of the thermal component has been identified as an optically thick, geometrically thin disc (Shakura & Sunyaev 1973). In the disc, the gas orbits around the BH in nearly Keplerian orbits. The orbiting material transports angular momentum outward by *viscosity*. In the Shakura-Sunyaev model, the mechanism responsible for the viscosity is not specified, but the viscosity is assumed to be proportional to the gas pressure through an *ad hoc* parameter α. This assumption is also known as the α *prescription*. Later, it has been found that the Magneto Rotational Instability (MRI, Balbus & Hawley 1998) can be the physical origin of the viscosity. This process destabilizes orbits when the accretion disc is characterized by differential rotation and a weak vertical magnetic field. In the Shakura-Sunyaev disc, the gravitational energy is converted into heat by viscosity. The disc temperature increases towards smaller radii so that the spectrum produced by the thin disc is a multi-temperature blackbody. This model has been used successfully to fit the thermal soft component observed in the IMS, VHS, and HSS.

The best emission process for explaining the non-thermal component is Compton up-scattering of soft photons. An optically thin region containing hot electrons can up-scatter cyclo-synchrotron photons from the same region or soft photons coming from the thin disc (Sunyaev & Truemper 1979; Sunyaev & Titarchuk 1980; Titarchuk 1994). In this interaction, the seed photons gain enough energy to produce the hard non-thermal (power-law) emission observed in the energy spectra. The geometry of this optically thin region is still a matter of debate, even though it is generally accepted that the region is located close to the BH. Different scenarios include a "corona" located above and below the accretion disc, a compact geometrically thick accretion flow located between the inner radius of the disc and the BH, and the base of a jet. Combining the accretion disc with an optically thin corona or flow, it is possible to reproduce most of the observed BHB energy spectra.

1.5.2 The truncated disc model

A plausible scenario to qualitatively explain the changes in energy spectral shape during an outburst is the *truncated disc model* (e.g. Esin, McClintock & Narayan 1997; Done, Gierlisnki & Kubota 2007). According to this model, an optically thick geometrically thin disc is truncated at a certain radius $r_{\rm o}$. Inside this radius, accretion takes place through an optically thin geometrically thick *hot flow*. The truncated disc is generally assumed to be a Shakura-Sunyaev disc and the hot flow an Advection Dominated Accretion Flow (ADAF, Narayan and Yi 1995). Initially, the disc is assumed to be truncated far away from the BH and, as mass accretion rate (so luminosity) increases, the truncation radius moves towards

the BH, down to the last stable orbit allowed by general relativity (ISCO, Innermost Stable Circular Orbit).
Using the truncated disc model, the transition between the spectral states is explained as a consequence of changes in the mass accretion rate. A typical outburst begins in the LHS: the mass accretion rate is low and the disc is truncated far away from the BH, so that the multi-temperature blackbody emission is low and (almost) undetectable. In this state, the energy spectrum is dominated by the hard non-thermal emission originating in the optically thin hot flow. When mass accretion rate increases, the disc moves towards the BH. As the truncation radius decreases, more and more disc photons illuminate and cool down the hot flow, so that the electron temperature of the flow decreases (with consequent increase of the power law index). The amount of reflection depends both on the characteristics of the reflector (ionization of the disc) and on the solid angle subtended by the disc from the hot flow, so that the model also predicts the observed correlation between the amount of reflection and the variation in the photon index of the power law (e.g. Gilfanov 2010). When the truncation radius approaches the BH, the disc temperature increases, the soft thermal component becomes dominant in the energy spectrum, the non-thermal component weakens, and all the characteristic frequencies observed in the power spectrum increase. In the HSS, the truncation radius is close to the ISCO, so that the energy spectrum is almost entirely dominated by the multi-temperature blackbody emission (e.g. Kubota & Done 2004).

1.5.3 Propagating mass accretion rate fluctuations

The idea of *propagating mass accretion rate fluctuations* in the accretion flow was first proposed by Lyubarskii (1997) for explaining the characteristics of the rapid variability in BHBs. The luminosity of the accretion flow depends on mass accretion rate, so on viscosity. Lyubarskii proposes that independent viscosity fluctuations arise at different radii and lead to corresponding fluctuations in mass accretion rate. The time scale of these fluctuations is assumed to be a function of radius, with short time scale fluctuations arising close to the BH and long time scale fluctuations stirred up at large radii. Because of accretion, the fluctuations propagate towards the BH. The mass accretion rate fluctuations at each radius are then the product of fluctuations arising locally and fluctuations propagated from larger radii. In this way, the emission from the region close to the BH is characterized by both high-frequency variability (generated locally) and low-frequency variability (stirred up at and propagated from large radii). Fig. 1.6 shows schematically the process of propagating fluctuations.
The propagating mass accretion rate fluctuations scenario can qualitatively explain several observational characteristics of the rapid variability in BHBs: the large amplitude X-ray variations observed over several decades of time-scale (Churazov, Gilfanov & Revnitsev 2001), the linear rms-flux relation (Uttley & McHardy 2001), and the hard phase lag. In particular, Kotov et al. (2001) showed that the hard phase lag observed in Cygnus X-1 can be reproduced by propagating fluctuations. Their phenomenological model is based on Lyubarskii's

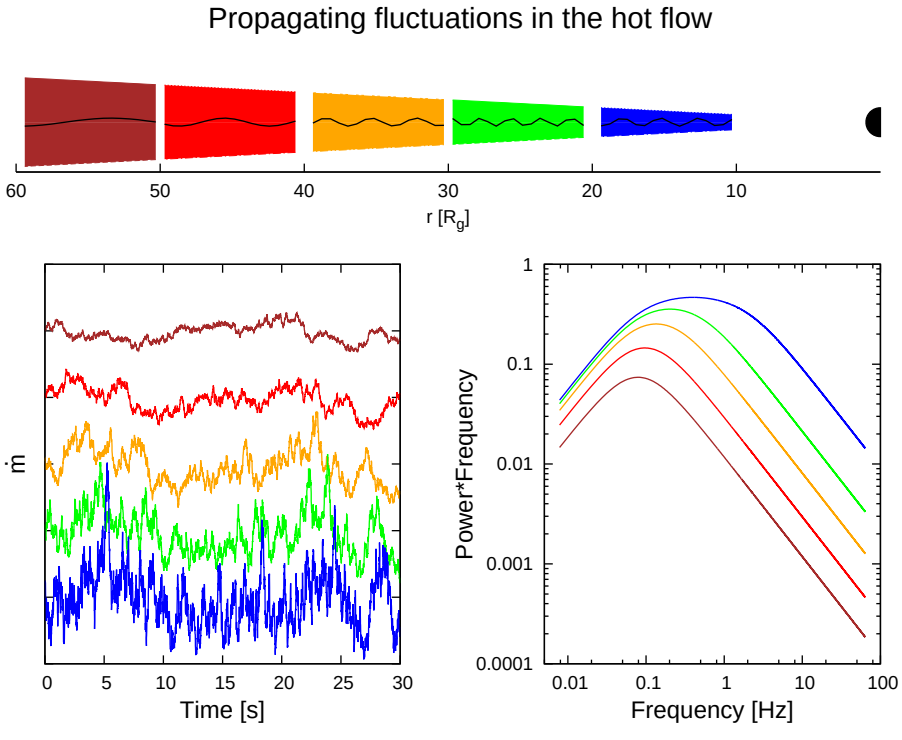

Figure 1.6: (Top) Schematic representation of the propagating fluctuations process. Mass accretion rate fluctuations (bottom-left panel) propagate from the outer (brown) to the inner (blue) region of the hot flow. The bottom-right panel shows the power spectrum of the fluctuations at different radii.

scenario and on the assumption that the energy spectrum emitted at each radius becomes progressively harder moving towards the BH. Propagating fluctuations can also explain the high coherence of the variability observed across a broad range of energy bands (Vaughan & Nowak 1997; Nowak et al. 1999a).

Starting from the Lyubarskii (1997) scenario and the Kotov et al. (2001) phenomenological model, Arevalo & Uttley (2006) used a Monte Carlo simulation to reproduce the rapid variability observed in BHBs and AGNs. With this model, they investigated the predicted power and phase lag spectrum varying fundamental parameters of the accreting system such as emissivities in the soft and hard band, disc scale-height factor, and input variability at each radius. Fitting model predictions to the ratio between hard and soft power spectrum and the phase lag spectrum of Cygnus X-1, they found good general agreement between data and the model. Ingram & Done (2011, 2012) made a further step in this direction. Their phenomenological model is computationally very similar to Arevalo & Uttley (2006), but it

combines propagating mass accretion rate fluctuations with the truncated disc model. Fluctuations propagating in the hot flow produce the broad band noise in the power spectrum and precession of the entire hot flow produces the QPO (Lense-Thirring precession, Stella & Vietri 1998; Ingram, Done & Fragile 2009). The Ingram & Done (2012) model is also based on results from numerical simulations of the accreting flow (Fragile et al. 2007). In particular, the surface density profile in the flow, which determines the characteristic time scale of the fluctuations at each radius, is extrapolated from these simulations.
The model PROPFLUC described in Ingram & van der Klis (2013) is a further refinement of the model of Ingram & Done (2012). In Arevalo & Uttley (2006) and in Ingram & Done (2012), the power spectrum is estimated by averaging many realizations (light curves) of a defined process. Ingram & van der Klis (2013) found an analytic formula for estimating analytically the power and cross-spectrum. In this way, it is possible to fit large data sets with much less computational steps compared to previous versions of the model.

1.6 Thesis outline

If correct, propagating fluctuations models can be the key to interpret rapid variability characteristics in terms of physical parameters. However, quantitative and systematic applications of these models have been few and incomplete.
In this thesis, we fit jointly the power spectrum in a soft and hard energy band, and the cross-spectrum between these two bands with the model PROPFLUC. This represents the maximum information that can be extracted by first- and second-order Fourier analysis from two energy bands (excluding higher order cumulants: the bi-spectrum, tri-spectrum, etc). Compared to previous works, our physical model is the first one predicting simultaneously power and cross-spectra in different energy bands and the first one to have been systematically applied to different sources and spectral states. For these reasons, our work represents the most stringent test for the propagating fluctuations hypothesis up to date.
Our analysis develops in the following way:

Chapter 2: we tested the hypothesis of mass accretion rate fluctuations propagating only in the hot flow with the BHB MAXI J1543-564 using RXTE data. We fitted the full power spectrum of the source both with a multi-Lorentzian and the PROPFLUC model. We described the rising part of the outburst in terms of PROPFLUC physical parameters tracing, in particular, the evolution of the truncation radius.

Chapter 3: we updated PROPFLUC including the hypothesis of mass accretion rate fluctuations propagating from the disc. We tested the code on the BHB MAXI J1659-152 using *Swift* data. We also fitted simultaneously, for the first time, power spectra in two energy bands and the cross-spectrum between these two bands. We compared the fits obtained considering fluctuations propagating only in the hot flow with the ones obtained including disc variability.

For most of our observations, including disc variability leads to a better fit. We also found good agreement between the truncation radius values obtained with PROPFLUC and spectral fitting.

Chapter 4: we further updated PROPFLUC including the hypothesis of extra variability arising in the hot flow, damping, and different propagation speeds. This represents the most sophisticated version of the model PROPFLUC up to date. We applied the model to two observations of the BHB XTE J1550-564 using high quality RXTE data. We found quantitative and qualitative disagreement between model and data, and concluded that such discrepancies are intrinsic to the propagating fluctuations scenario.

Chapter 5: we applied the model PROPFLUC to the BHB Cygnus X-1. Contrary to XTE J1550-564, Cygnus X-1 is a persistent source and does not show mid- and high-frequency QPOs. We attempted to fit the data in the hard state, soft state, and in the transition between these two states. We found good quantitative description of the hard and soft state in terms of propagating fluctuations, but we could not obtain a similarly satisfactory result for the transition. The lack of QPOs and the surface density profile predicted by PROPFLUC in the soft and hard state, suggest that the BH spin may be aligned with the inner accretion disc and therefore probably with the rotational axis of the binary system.

I

2

Evolution of the hot flow of MAXI J1543-564

S. Rapisarda, A. Ingram and M. van der Klis

Monthly Notices of the Royal Astronomical Sociaty, 440, 2882

Abstract

We present a spectral and timing analysis of the black hole (BH) candidate MAXI J1543-564 during its 2011 outburst. As shown in previous work, the source follows the standard evolution of a (BH) outburst. During the rising phase of the outburst we detect an abrupt change in timing behaviour associated with the occurrence of a type-B quasi-periodic oscillation (QPO). This QPO and the simultaneously detected radio emission mark the transition between hard and soft intermediate state. We fit power spectra from the rising phase of the outburst using the recently proposed model PROPFLUC. This assumes a truncated disc / hot inner flow geometry, with mass accretion rate fluctuations propagating through a precessing inner flow. We link the PROPFLUC physical parameters to the phenomenological multi-Lorentzian fit parameters. The physical parameter dominating the QPO frequency is the truncation radius, while broad-band noise characteristics are also influenced by the radial surface density and emissivity profiles of the flow. In the outburst rise we found that the truncation radius decreases from $r_{\rm o} \approx 24$ to 10 $R_{\rm g}$, and the surface density increases faster than the mass accretion rate, as previously reported for XTE J1550-564. Two soft intermediate state observations could not be fitted with PROPFLUC, and we suggest that they are coincident with the ejection of material from the inner regions of the flow in a jet or accretion of these regions into the BH horizon, explaining the drop in QPO frequency and suppression of broad-band variability preferentially at high-energy bands coincident with a radio flare.

2.1 Introduction

Transient black hole binaries (BHBs) display outbursts exhibiting several states, characterized by both spectral and timing properties (e.g. Belloni et al. 2005; Remillard & McClintock 2006; Belloni 2010; Gilfanov 2010). During the outburst, sources typically follow a 'q' shaped, anti–clockwise track on a plot of X-ray flux versus spectral hardness ratio (hardness–intensity diagram: hereafter HID), with the quiescent state occupying the bottom-right corner. The initial transition from hard (LHS) to soft (HSS), via intermediate states, occurs when the power-law component of the spectrum is observed to soften (photon index $\Gamma \sim 1.7$–2.4) and a disc blackbody component (peaking in soft X-rays) becomes increasingly prominent. A power spectral analysis of the rapid variability reveals a quasi-periodic oscillation (QPO), which shows up as narrow harmonically related peaks, superimposed on broad-band continuum noise. The QPO fundamental frequency is observed to increase from ≈ 0.1 to 10 Hz during the transition from the hard state, after which the X-ray emission becomes very stable in the soft state. Power spectral evolution correlates tightly with spectral evolution, with all the characteristic frequencies increasing with spectral hardness (e.g. Wijnands & van der Klis 1998; Psaltis, Belloni & van der Klis 1999; Homan et al. 2001). QPOs observed coincident with broad-band noise are defined as type-C QPOs (Remillard et al. 2002; Casella et al. 2005). Type-B QPOs (Wijnands, Homan & van der Klis 1999), typically with a frequency of $\approx$ 6–10 Hz, are observed in the intermediate state when the broad-band noise suddenly disappears. These features quickly evolve into type-A QPOs (Wijnands, Homan & van der Klis 1999), which are broader and weaker. Since the sudden suppression of the broad-band noise hints a large physical change in the system, intermediate state observations displaying type-C QPOs are classified as hard intermediate state (HIMS) and those displaying type-A or B QPOs as soft intermediate state (SIMS). Additionally, a large radio flare, indicative of a jet ejection event, is often observed to be coincident with the onset of the SIMS (Fender, Belloni & Gallo 2004), although this is not always exact (Fender, Belloni, & Gallo 2005).

The spectral and timing properties of BHBs can be described by *the truncated disc model* (e.g. Esin, McClintock & Narayan 1997; Done, Gierliński & Kubota 2007) where an optically thick, geometrically thin accretion disc which produces the multitemperature blackbody spectral component (Shakura & Sunyaev 1973) truncates at some radius, $r_{\rm o}$, larger than the innermost stable circular orbit (ISCO). In the region between this truncation radius $r_{\rm o}$ and an inner radius $r_{\rm i}$ ($r_{\rm o} > r_{\rm i} > r_{ISCO}$), accretion takes place via a hot, optically thin, geometrically thick accretion flow (hereafter inner flow). Compton up-scattering of cool disc photons by hot electrons in the flow produces the power-law spectral component (Thorne & Price 1975; Sunyaev & Truemper 1979). In the hard state $r_{\rm o}$ is large ($\approx 60\ R_{\rm g}$, where $R_{\rm g} = GM/c^2$ is a gravitational radius), so only a small fraction of the disc photons illuminates the flow, giving rise to a weak direct disc component and hard power-law emission. As the average mass accretion rate increases during the outburst, $r_{\rm o}$ decreases, so more direct disc emission is seen and a greater luminosity of disc photons cool the flow, resulting in softer power law emission. When $r_{\rm o}$ reaches the ISCO, the direct disc emission completely dominates the spectrum and

the transition to the soft state is complete.
This scenario is the framework of the propagating fluctuations model PROPFLUC (Ingram & Done 2011, 2012, hereafter ID11, ID12; Ingram & Van der Klis 2013, hereafter IK13), a model that can reproduce power density spectra by combining the effects of the propagation of mass accretion rate fluctuations in the inner flow (Lyubarskii 1997; Arevalo & Uttley 2006), responsible for generating the broad-band noise, with solid-body Lense–Thirring (LT) precession of this flow (Fragile et al. 2007; Ingram, Done & Fragile 2009), producing QPOs. Mass accretion rate fluctuations are generated throughout the inner flow, with the contribution to the rms variability from each region peaking at the local viscous frequency (e.g. Lyubarskii 1997; Churazov, Gilfanov & Revnivtsev 2001; Arevalo & Uttley 2006), thus the fast variability originates from the inner regions and the slow variability from the outer regions. As material is accreted, fluctuations propagate inwards, modulating the faster variability generated in the inner regions. Emission is thus highly correlated from all regions of the flow, giving rise to the observed linear rms–flux relation (Uttley & McHardy 2001; Uttley, McHardy & Vaughan 2005).
In this paper, we present a spectral and timing analysis of the source MAXI J1543-564 during its 2011 outburst. The source, discovered by MAXI/GSC (the Gas Slit Camera of the Monitor of ALL-sky X-ray Image; Matsuoka et al. 2009) on 2011 May 08 (Negoro et al. 2011), was first analysed by Stiele et al. (2012). Their analysis showed that the outburst evolution follows the usual BHBs behaviour, the exponential flux decay is interrupted by several flares, and during the transition from LHS and HSS a type-C QPO is observed. Looking at other wavelengths, Miller-Jones et al. (2011) report the detection of radio emission at MJD 55695.73. In this work, we analyse the spectral and timing properties of the source in different energy bands, and we use the power density spectra of the rising phase of the outburst to systematically explore for the first time the capabilities of PROPFLUC.

2.2 Observations and data analysis

We analysed data from the RXTE Proportional Counter Array (Jahoda et al. 1996) using 99 pointed observations collected between May 10 and 2011 September 30. Each observation consisted of between 300 and 4750 s of useful data.
We used Standard 2 mode data (16 s time resolution) to calculate a hard colour (HC) as the 16.0–20.0 / 2.0–6.0 keV count rate ratio and define the intensity as the count rate in the 2.0–20.0 keV band. All the observations were background subtracted and all count rates were normalized by the corresponding Crab values closest in time to the observations.
We used the $\approx$ 125 μs time resolution Event mode and the $\approx$ 1 μs time resolution Good-Xenon mode data for Fourier timing analysis. We constructed Leahy-normalized power spectra using 128 s data segments and 1/8192 s time bins to obtain a frequency resolution of 1/128 Hz and a Nyquist frequency of 4096 Hz. After averaging these power spectra per observation, we subtracted the Poisson noise using the method developed by Klein-Wolt et

al. (2004), based on the expression of Zhang et al. (1995), and renormalized the spectra to power density P_ν in units of (rms / mean)^2 Hz^{-1}. In this normalization the fractional rms of a variability component is directly proportional to the square root of its integrated power density: rms $= 100\sqrt{\int_0^\infty P_\nu d\nu}$ %. No background or dead-time corrections were made in computing the power spectra. This procedure was performed in four different energy bands: 2.87–4.90 keV (band 1), 4.90–9.81 keV (band 2), 9.81–20.20 keV (band 3), and the full 2.87-20.20 keV (band 0). The power spectra were fitted using a multi-Lorentzian function in which each Lorentzian contributing to the fit function is specified by a characteristic frequency $\nu_{max} = \sqrt{{\nu_0}^2 + (\mathrm{FWHM}/2)^2}$ (Belloni, Psaltis & van der Klis 2002), and a quality factor $Q = \nu_0/\mathrm{FWHM}$, where FWHM is the full width at half-maximum and ν_0 is the centroid frequency of the Lorentzian. All the power spectra shown in this paper were plotted using the power times frequency representation (νP_ν), in order to visualize ν_{max} as the frequency where the Lorentzian maximum occurs.

2.3 Results

The light curve of the source is shown in Fig. 2.1(a), where the 2–20 keV intensity is plotted versus time (MJD) for each pointed observation.
We subdivided the evolution of the outburst in five parts. In the first part of the outburst (MJD 55691–55696) the source rises to maximum intensity ($\approx$ 68 mCrab) in 5 d from the beginning of the RXTE observations. The second part (first grey area, MJD 55696–55713) is characterized by an intensity decay that is not smooth, but interrupted by four additional peaks with intensities between $\approx$ 47 and $\approx$ 58 mCrab. The third part (MJD 55713–55725, between the two grey areas) does not show any intensity peak but only a gradual decay. The following period (MJD 55725–55744, second grey area) is characterized by a broad maximum and several additional intensity peaks (between $\approx$ 34 and $\approx$ 42 mCrab) less luminous compared to those of the first grey area. Finally, the last part (MJD 55744–55834) consists of a relatively smooth decay until the end of the observations.

2.3.1 Color diagrams

Fig. 2.2 shows the HID, where the average intensity of each observation is plotted versus the HC. The source follows a counterclockwise path, starting and ending in the right (hard) part of the diagram at different luminosities. This is the usual behaviour observed for BH outbursts. In order to better follow the spectral evolution of the source along the outburst, we also plotted in Fig. 2.1(c) the HC versus time.
In the first observation the source is harder than Crab (HC = 1.71) and in the following six observations softens continuously, while at the same time its intensity increases from $\approx$ 24 to $\approx$ 68 mCrab. For the remaining observations the source remains in the soft part of the HID (HC$\leq$0.5) except for the very last observation, where it goes back to a colour harder than Crab (HC = 1.31$\pm$0.16).

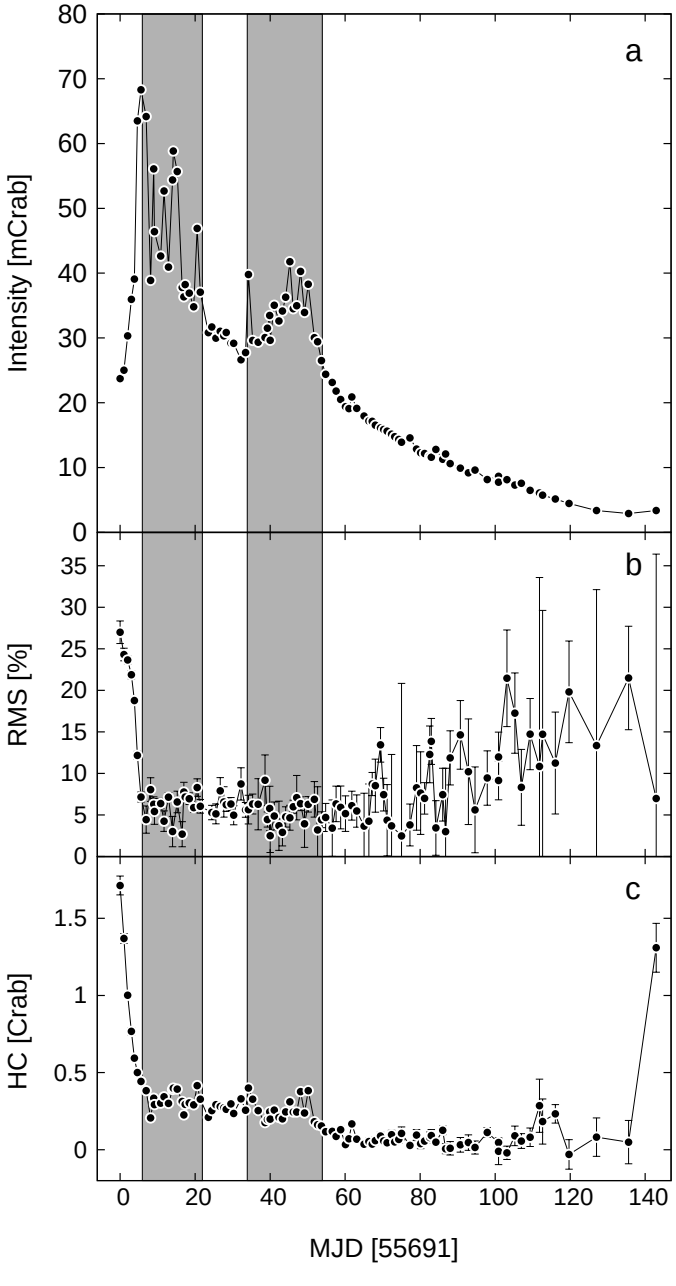

Figure 2.1: a) Intensity [mCrab], b) rms [%], c) and HC [Crab] versus time for the 99 pointed observations. The grey rectangular areas divide the light curve in five time intervals characterized by different long-term luminosity variability. Data points are plotted with 1σ error bars.

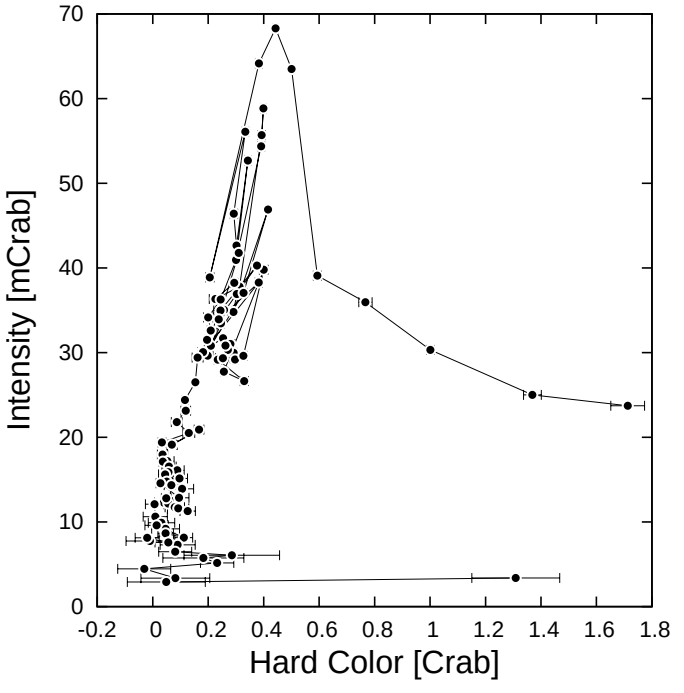

Figure 2.2: HC versus Intensity normalized to the Crab. Points represent average intensity and HC for each observation. 1σ error bars are plotted for the HC.

As can be noted in Fig. 2.1(c), the transitions between hard and soft spectrum happen on short time-scales ($\approx$ 10 d) compared to the time spent by the source in the soft state ($\approx$ 125 d). However, while the initial transition from hard to soft state is simultaneous with a quick change in intensity (+ 188%), the final transition (last observation) from soft to hard spectrum is characterized by a fractional intensity change of only + 16%, i.e. increasing when the source gets harder.

2.3.2 Time variability

The 1/129–10 Hz rms values as computed from the power spectra in band 0 are reported in Fig. 2.1(b). The first five observations, during which the source rapidly becomes softer and brighter are characterized by rms values of $\approx$ 19–27%. In the remaining observations the rms values are between $\approx$ 2 and $\approx$ 10% with few exceptions.
Integrated rms is systematically higher for higher energies. From the beginning of the observations, as the intensity increases, integrated rms decreases independently from photon energy, but the rms decrease trend is different between energy bands. In order to better show these differences, we plotted in Fig. 2.5 the total fractional rms of the first seven observa-

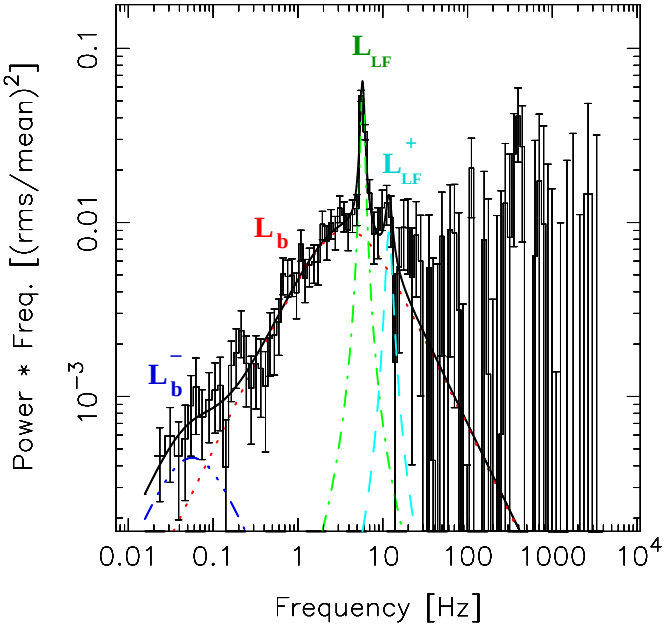

Figure 2.3: Multi-Lorentzian fit of the fifth power spectrum. Four main components were identified: a main QPO $L_{\rm LF}$, its harmonic $L^{+}_{\rm LF}$, a broad-band noise component $L_{\rm b}$, and another broad component at lower frequency $L^{-}_{\rm b}$.

tions for all the energy bands. Band 1 (red) shows a smooth and continuous rms decrease with time, while in band 2 (green) and band 3 (blue), the rms decrease is characterized by a "jump" between observations 5 and 6 (Δrms $\approx -9\%$ in band 2, Δrms $\approx -11\%$ in band 3). Observation 6 is also characterized by the detection of radio emission, indicated by the orange arrow.

QPOs and broad-band features

Only in the first seven observations we detect QPOs ($Q > 2$) and/or broad-band components ($Q < 2$) in at least some energy bands. We used the power spectrum of the fifth observation in band 0 (MJD 55694.884, Fig. 2.3) as a reference to identify four significant ($\sigma > 3$, single-trial) components: a main QPO L_{LF}, its harmonic L^{+}_{LF}, a broad-band noise component $L_{\rm b}$, and another broad-band component $L^{-}_{\rm b}$ at lower frequency. In our analysis we reported all components with single trial significance $\sigma \geq 3$ and additionally those components with sig-

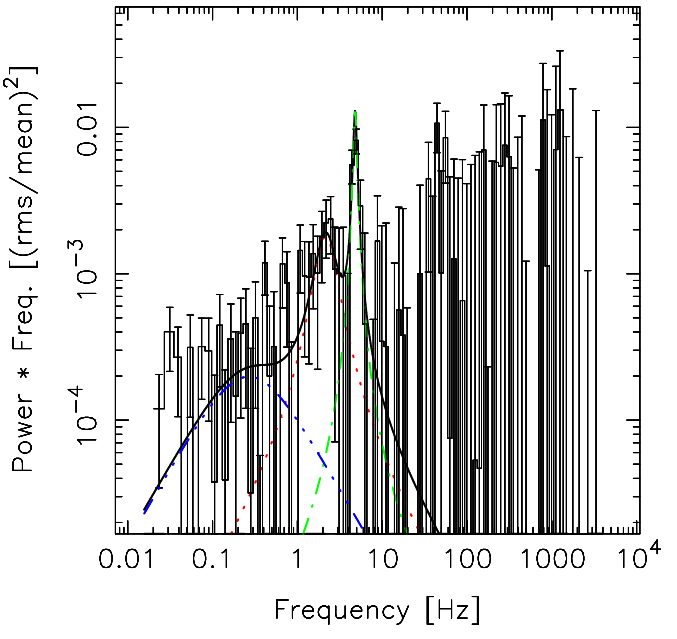

Figure 2.4: Lorentzian fit of observation seven showing a type-B QPO.

nificance between 2σ and 3σ that could be identified as L_{LF}, L_{LF}^{+}, $L_{\rm b}$, or $L_{\rm b}^{-}$. Table 2.1 shows ν, Q, rms, significance (σ) and reduced χ^2 for every fitted component in the seven observations analysed (1–7) for all the energy bands. We also report the 99.87% upper limits calculated fixing ν and Q to values equal to the most significant corresponding component between the energy bands fitted in the same observation. Empty lines mean that no components were fitted and no upper limit could be determined.

Figs 2.6(g) and (h) show the frequencies of the fitted QPOs (triangles for L_{LF}, diamonds for L_{LF}^{+}), broad-band components (squares for $L_{\rm b}$, circles for $L_{\rm b}^{-}$), and unidentified narrow ($Q > 2$) components (pentagons), and their rms versus time in band 0, respectively. Solid symbols indicate significant components and open symbols components with significance between 2σ and 3σ. The 2–3σ unidentified component of observation 6 (see Table 2.1, bottom) is included in our plot because its characteristic frequency matches with the subharmonic frequency of the identified component L_{LF}. Similarly, two 2–3σ unidentified components fitted in observation 7 (Fig. 2.4) were reported, as one matches with the subharmonic frequency of L_{LF}, and the other with $L_{\rm b}$. Squares and circles were slightly shifted to the right for clarity.

Always referring to band 0, in the first five observations one significant low frequency QPO (L_{LF}) was fitted for each spectrum and only the third observation shows a significant harmonic (L_{LF}^{+}). The L_{LF} frequency increases with time from $\approx$ 1.1 to $\approx$ 5.8 Hz while its rms decreases from $\approx$ 17% to $\approx$ 10% (see Table 2.1). Observation 7 shows a significant QPO with ν_{max} = 4.7 Hz (Fig. 2.4). The peak characteristics (ν_{max} = 4.7 Hz, Q = 9, rms $\approx$ 4.8)

of and the low 1/128–10 Hz rms ($\approx 7.2\%$) associated with this QPO, are characteristics of type-B QPOs (e.g. Casella et al. 2005). Considering also the 2–3 σ QPO fitted in observation 6 (ν_{max} = 5.7 Hz, $\sigma \approx 2.5$), in observations 6 and 7 L_{LF} frequency and rms are not anti-correlated anymore. The characteristic frequency of L_{LF} decreases from ≈ 5.8 to ≈ 4.7 Hz while the rms still decreases from ≈ 6 to $\approx 5\%$.

One significant broad-band component ($L_{\rm b}$) with ν_{max} in the interval $\approx$ 2–4 Hz was fitted in observations 1–6. The rms of this component decreases with time (from 20 to 9%), with a clear decreasing trend observable only in observations 5 and 6, while its ν_{max} remains almost in the same frequency range (around 3 Hz). In observations 5–7, we fitted another broad-band component ($L_{\rm b}^{-}$) characterized by an increasing ν_{max} (from observation 5 to 7) in the interval $\approx$ 0.06–0.66 Hz and rms between 2 and 4%.

The timing features in the other energy bands are reported in Figs. 2.6(a)–(f). Similarly to panels (g) and (h), plots (a) and (b), (c) and (d), and (e) and (f) show frequency and rms evolution for power spectral components fitted in bands 1, 2, and 3, respectively. No significant characteristic frequency shift was detected between energy bands in any power spectral component, while the rms values are systematically higher for higher energies (Table 2.1). In band 1, L_{LF} frequency increases with time (from ≈ 1.1 to ≈ 6.5 Hz) in the first six observations while no significant QPO was fitted in observation 7. The behaviour of L_{LF} characteristic frequency in bands 2 and 3 is mostly identical to band 1 for observations 1–5, but we observe some differences in observations 6 and 7. The 2–3σ QPO ($\sigma \approx 2.2$) fitted in observation 6 (band 2) seems to break the anti-correlation between frequency and rms shown in observations 1–5, but in band 3 the QPO frequency error bar is too big to infer any trend. However, the anti–correlation is evident in observation 7, where a significant QPO was fitted in bands 2 and 3 with lower characteristic frequency compared to observation 5. The rms of L_{LF} in band 1 decreases as the QPO frequency increases, but in bands 2 and 3 this trend is progressively weaker. Indeed, in band 3 the L_{LF} rms slightly oscillates around ≈ 17 and $\approx 11\%$ in the first five observations and decreases to $\approx 11\%$ only in the last two observations.

The broad-band component ($L_{\rm b}$) frequency slightly varies around ≈ 5 Hz in observations 3–5 (band 1), while no significant broad-band components were fitted in observations 6 and 7. In band 2, $L_{\rm b}$ frequency shows a clear decreasing trend only in the last three observations ($\nu \approx$ 4.4–1.6 Hz), while does not show any clear trend in band 3. $L_{\rm b}$ rms decreases smoothly with time in band 1 (from ≈ 22 to $\approx 15\%$), but it does not show the same trend in the other two energy bands. In band 2 we observe a clear decrease of $L_{\rm b}$ rms only in observations 5–6 (from ≈ 20 to $\approx 7\%$) and in band 3 it oscillates between 22 and 27%.

Apart from the full energy, $L_{\rm b}^{-}$ was fitted only in observation 5 (band 1) and 6 (band 1–3), but it is significant just at low photon energy (band 1, observation 6). L_{textb}^{-} frequency and rms behaviour in band 1 is mostly identical to band 0.

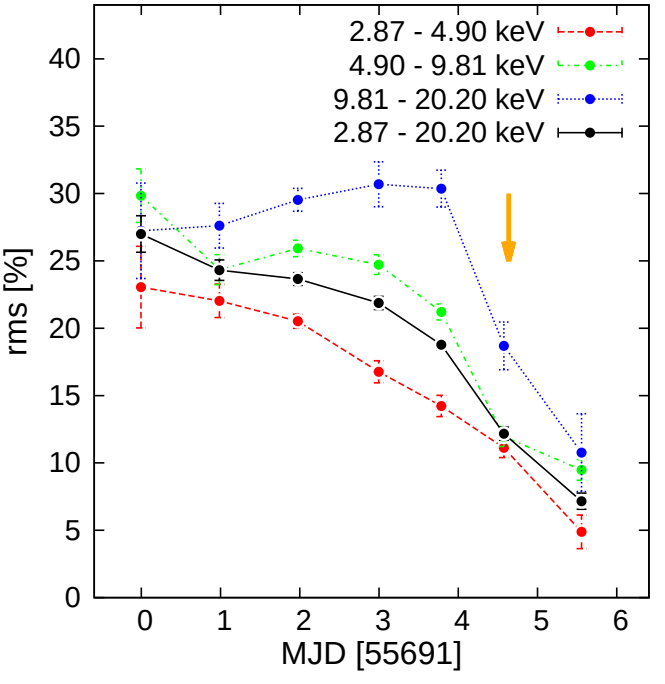

Figure 2.5: Fractional integrated 1/128–10 Hz rms versus time in the first seven observations for the bands considered. The orange arrow represents the time of the radio emission. All values are plotted with 1σ error bars.

2.4 Model fitting

We fit the power spectra of the first five observations using PROPFLUC (ID11; ID12; IK13). Whereas original explorations of the model (ID11; ID12) used computationally intensive Monte Carlo simulations, IK13 developed an exact analytic version of the model, allowing us for the first time to explore its capabilities systematically. We also investigate the relation between the values we obtained from the previously described phenomenological fitting of several Lorentzians (Sections 2.2 and 2.3) and the model physical parameters (see table 2 in ID12 for a summary and description of all the physical parameters).

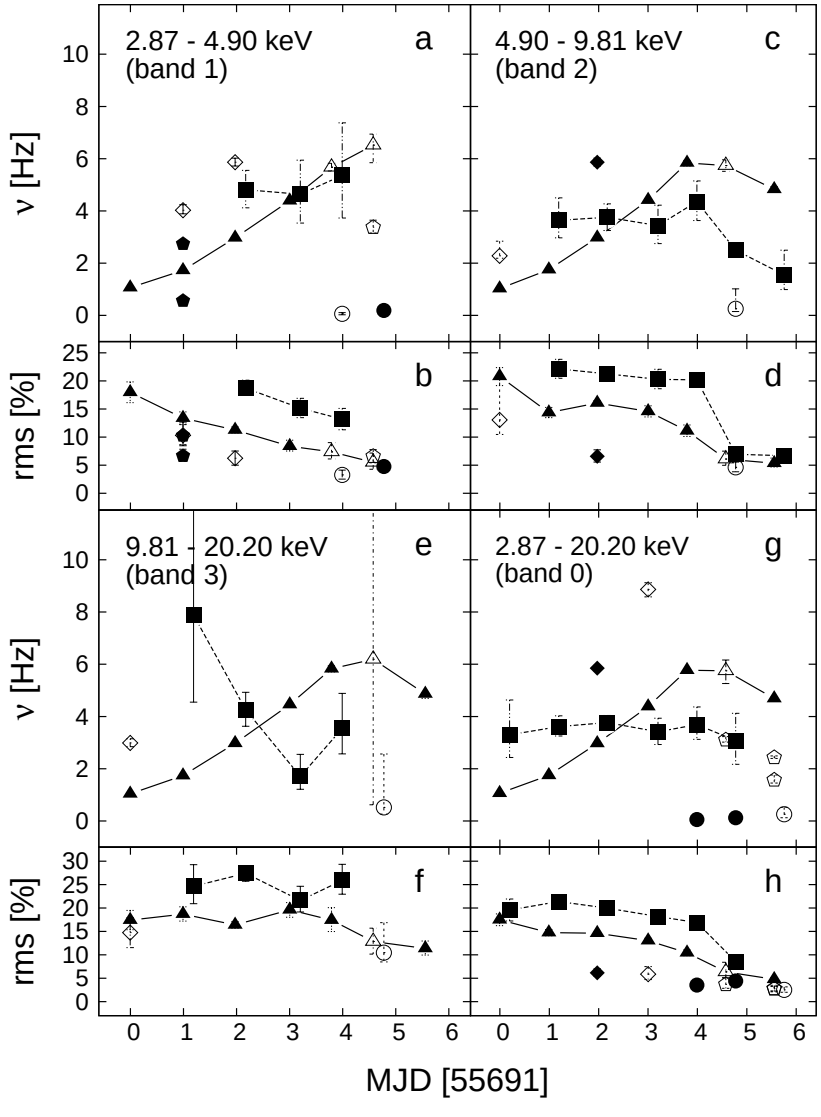

Figure 2.6: Characteristic frequency and rms of L_{LF} (triangles), L_{LF}^{+} (diamonds), $L_{\rm b}$ (squares), $L_{\rm b}^{-}$ (circles), and other significant unidentified components (pentagons) fitted in the first seven observations in all the energy bands ($L_{\rm b}$ and $L_{\rm b}^{-}$ have been shifted slightly to the right with respect to the original position for clear reading). Open symbols indicate components with significance between 2 and 3 σ, while full symbols stand for $\sigma > 3$ significant components. All values are plotted with 1σ error bars.

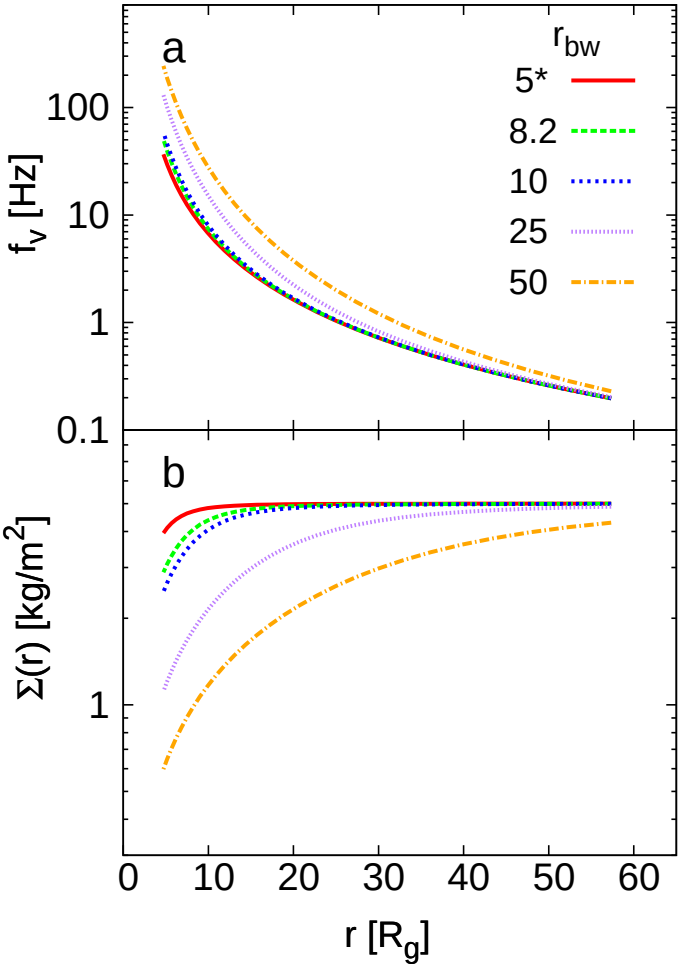

Figure 2.7: Viscous frequency (a) and surface density profile (b) versus inner flow radius computed varying r_{bw} (Fig. 2.8*b*).

2.4.1 The model

PROPFLUC (Section 2.1) parametrizes the flow surface density profile, which is required to calculate both the precession frequency and local viscous frequency, as a bending power law[1]:

$$\Sigma(r) = \frac{\Sigma_0 \dot{M}_0}{cR_g} \frac{x^\lambda}{(1+x^\kappa)^{(\zeta+\lambda)/\kappa}} \tag{2.1}$$

[1]ID12 showed that this surface density profile describes that measured from Fragile et al. (2007)'s simulations.

where $x = r/r_{\rm bw}$ and $r_{\rm bw}$ is a break radius such that $\Sigma(r) \sim r^{-\zeta}$ for $r \gg$ rbw and $\Sigma(r) \sim r^{-\lambda}$ for $r \ll r_{\rm bw}$, with the sharpness of the break controlled by the parameter κ (Fig. 2.7b shows $\Sigma(r)$ examples for different $r_{\rm bw}$ values). Here, $\dot{M}_0$ is the average mass accretion rate over the course of a single observation and Σ_0 is a dimensionless normalization constant. Throughout this paper, we employ the convention that $r \equiv R/R_{\rm g}$ is radius expressed in units of $R_{\rm g}$. The surface density drop off at the bending wave radius, $r_{\rm bw}$, is due to the torque created by the radial dependence of LT precession ($\nu_{\rm LT} \propto \sim r^{-3}$); i.e. essentially the inner regions try to precess quicker than the outer regions. Outside $r_{\rm bw}$, bending waves (pressure waves) strongly couple the flow together but inside $r_{\rm bw}$, material falls quickly towards the BH (Lubow et al. 2002; Fragile et al. 2007). The precession frequency of the flow is given by (Liu & Melia 2002):

$$\nu_{prec} = \nu_{qpo} = \frac{\int_{r_i}^{r_o} f_{LT} f_k \Sigma(r) r^3 dr}{\int_{r_i}^{r_o} f_k \Sigma(r) r^3 dr} \tag{2.2}$$

where f_k is the Keplerian orbital frequency and $f_{\rm LT}$ is the point particle LT precession frequency at r (ID11). The bending wave radius carries information about the shape of the inner flow because it is dependent on the scaleheight factor of the flow, h/r:

$$r_{bw} = 3(h/r)^{-4/5} a_*^{2/5} \tag{2.3}$$

where a_* is the dimensionless spin parameter.
If the mass is conserved on long time-scales, the viscous frequency can be expressed as (Frank, King & Raine 2002; ID12):

$$\nu_{visc}(r) = \frac{\dot{M}_0}{2\pi R^2 \Sigma(r)} \tag{2.4}$$

PROPFLUC assumes that the power spectrum of mass accretion rate fluctuations generated at r is a zero-centred Lorentzian cutting off at the viscous frequency. The model splits the flow up into rings and assumes that a constant fractional variability, F_{var}, is generated per decade in radius. The resolution of the model is set by the number of rings per decade in radial extent, N_{dec}; i.e. the interval between $r = 10$ and 100 is split into N_{dec} rings. Consequently, the fractional variability in the mass accretion rate, $\dot{M}(r,t)$, at each ring is $F_{var}/\sqrt{N_{dec}}$, so that N_{dec} of these time series multiplied together has a fractional variability F_{var}. The emitted luminosity from a ring at r_n is then assumed to be $\propto r_n^{2-\gamma} \Sigma(r_n) \dot{M}(r_n,t)$, where the emissivity index $\gamma > 2$ is a model parameter, and the total emitted luminosity is simply the sum of the contributions from each ring. Thus, the low frequency break in the power spectrum corresponds roughly to $\nu_{visc}(r_{\rm o})$ (Churazov, Gilfanov & Revnivtsev 2001; Ingram & Done 2010). The high frequency break, however, does not correspond to $\nu_{visc}(r_i)$ because interference between radiation from different rings in the flow has a significant influence on the shape of the broad-band noise at high frequencies (ID11; IK13). The emissivity index also clearly affects the shape of the high frequency noise: increasing γ increases the amount of high frequency noise in the power spectrum.

2.4.2 Exploration of model parameters

To better understand the relation between the phenomenological parameters derived from Lorentzian power spectral fit characteristics and the physical parameters of PROPFLUC, and to provide guidance in fitting this model to observed power spectra whose rough characteristics are known, we compute model power spectra with a Nyquist frequency of 128 Hz and vary one by one the main parameters. We fix the BH mass ($10M_{\odot}$), the dimensionless spin parameter ($a_* = 0.5$), the inner radius ($r_{\rm i}$ = 4.5 $R_{\rm g}$, so that $r_{\rm i} > r_{ISCO}$), the bending wave radius ($r_{bw} = 8.2$, so that $h/r \approx 0.2$), and the emissivity index ($\gamma = 4.0$). We use a resolution $N_{dec} = 25$ and include a QPO with fixed width and rms. The results of the calculations are shown in Fig. 2.8. Every plot specifies the parameter values, the asterisk in each panel denotes the value of that parameter used for all the other computations.

Fig. 2.8(a) shows that the centroid frequency of the broad-band component (hereafter $\nu_{\rm b}$) decreases as Σ_0 increases, while the centroid frequency of the QPO (hereafter $\nu_{\rm qpo}$) does not change. This can be understood from equations 2.2 and 2.4. Equation (2.4) shows that increasing Σ_0 decreases $\nu_{visc}(r_0) \approx \nu_{\rm b}$ but, since both integrals in equation (2.2) contain the surface density, the constant Σ_0 cancels in the calculation of ν_{QPO}. In contrast, the *shape* of the surface density profile affects both the broad-band noise and ν_{qpo}. Equation (2.2) shows that the precession frequency of the entire flow is a surface density weighted average of $\nu_{\rm LT}(r)$ (the precession frequency of a test mass a distance r from the BH). Therefore increasing the surface density at large r slows down precession and increasing the surface density at small r speeds up precession. Equation (2.4) and Figs 2.7(a) and (b) show that increasing the surface density in any region decreases the viscous frequency in that region and increasing the *gradient* of $\Sigma(r)$ increases the *range* of frequencies at which the broad-band noise contains significant power.

Fig. 2.8(b) shows that ν_{qpo} decreases with increasing $r_{\rm bw}$. This is because $r_{\rm bw}$ governs where in the flow the surface density starts to drop off (see Fig. 2.7b), and so increasing it weights the surface density towards the outer regions of the flow. Since, as demonstrated in Fig. 2.7, increasing $r_{\rm bw}$ slightly reduces the average surface density, this slightly increases the viscous frequency at the inner and outer rings in the flow, $\nu_{visc}(r_{\rm i})$ and $\nu_{visc}(r_{\rm o})$. This causes $\nu_{\rm b}$ to increase by a small amount (which is difficult to see in Fig. 2.8(b) because of the QPO), and its affect on the high-frequency power is complicated by the emissivity and interference between radiation from different regions of the flow (see IK13). Similar considerations are also valid for Figs 2.8(c)–(e).

Fig. 2.8(f) shows ν_{qpo} increasing as $r_{\rm o}$ decreases, roughly following the trend $\nu_{qpo} \propto r_{\rm o}^{-C}$, where C is a positive constant ($C \approx 2.2$ for the fiducial model parameters). This can be understood if we assume a constant surface density profile (i.e. $\zeta = 0$ and r_{bw} is small) and use the weak field approximation for LT precession, $\nu_{\rm LT}(r) \propto r^{-3}$, to obtain a simplified version of equation 2 in Ingram, Done, & Fragile (2009):

$$\nu_{qpo} = \frac{5a_*}{\pi} \frac{[1-(r_i/r_o)^{1/2}]}{r_o^{5/2} r_i^{1/2} [1-(r_i/r_o)^{5/2}]} \frac{c}{R_g} \tag{2.5}$$

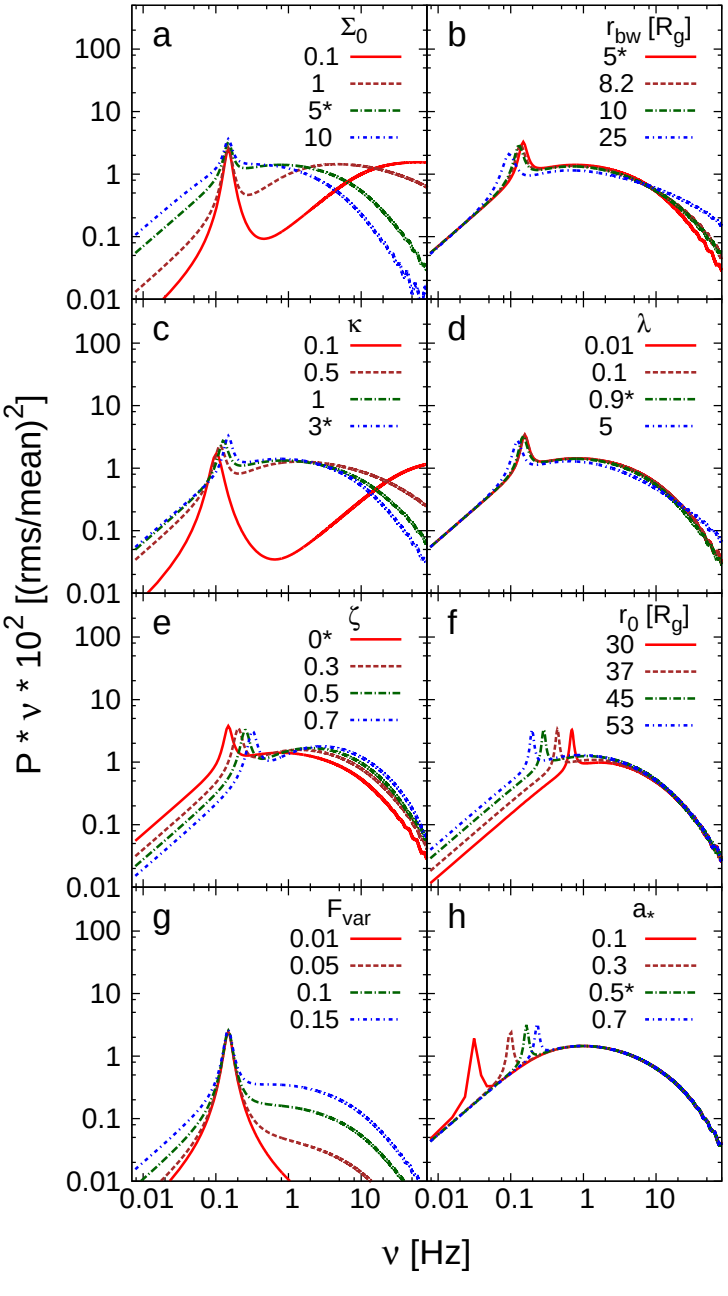

Figure 2.8: Power spectra computed varying each of the main physical parameters of the model in turn as indicated. Asterisk indicates value of each parameter for all other computations.

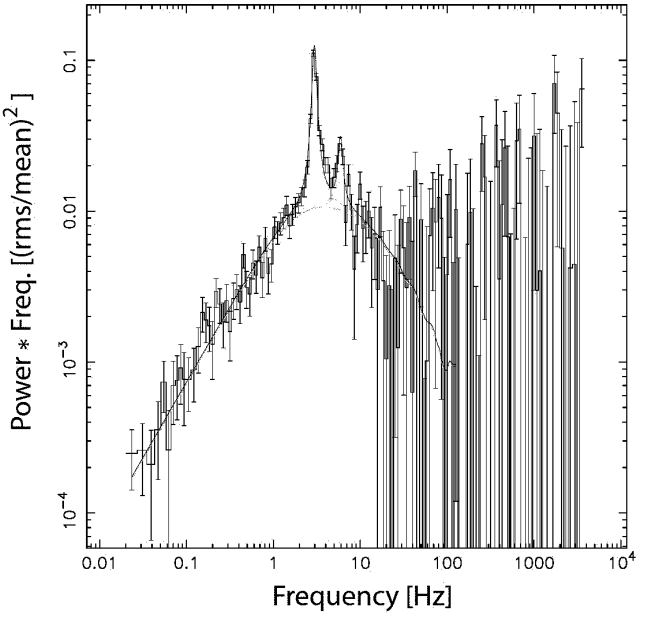

Figure 2.9: PROPFLUC fit of the third power spectrum.

We see that, for $r_{\rm i}/r_{\rm o} \ll 1$, the $r_{\rm o}$ dependence of ν_{qpo} reduces to $\nu_{qpo}(r_{\rm o}) \propto\sim r_{\rm o}^{-5/2} \sim r_{\rm o}^{-2.2}$. We also see from this equation that increasing a_* increases the QPO frequency, as demonstrated in Fig. 2.8(h). Thus, the parameters which most affect the QPO frequency are $r_{\rm o}$ ($\approx$ quadratic) and a_* (linear).

2.4.3 The fit

As described in section 2.4.1, the model is based on the inner accretion flow variability. For this reason, in order to avoid contamination from the disc, the best data choice for fitting would be observations in the high-energy band ($\approx$ 10–20 keV), as mentioned in ID11. Because of the low count rate, we considered a wide 2.87–20.20 keV band. The model assumes that all the variability is generated in the hot flow, so formally, in this scenario, the only effect of the disc is to suppress the variability amplitudes at lower energies by dilution. Of course the possibility that the variability is generated in the disc and then propagates towards the inner flow affecting its emission, cannot be excluded, but for our first explorative fit we just considered the simple scenario described above. We note that, using the spectral model TBABS * SMEDGE * (DISCBB + NTHCOMP + GAUSS) (Mitsuda et al. 1984; Zdziarski, Johnson & Magdziarz 1996; Zycki, Done & Smith 1999; Wilms, Allen & McCray 2000), we find that the disc contribution to the flux in band 1 increases from $\approx$ 38% in observation 1 to $\approx$ 61% in observation 7 (it contributes significantly less in the other bands). Since the rms in

band 1 decreases from ≈ 33 to ≈ 5% for observations 1-7, our assumption that the disc is stable implies that the fractional rms of the flow in this band is ≈ 53 to ≈ 13% for observation 1-7 respectively, which is reasonable.
Since PROPFLUC is not intended to explain the SIMS, we only fit the first five observations and leave a discussion of qualitative interpretation of observations 6 and 7 to section 2.5, in the absence of statistically acceptable fits. We fitted logarithmically binned data points in the frequency range 1/128–128 Hz, using the same resolution for data and model. We used N_{dec} = 15 for all the fits. Compared to power spectra computed using higher resolution (see section 2.4.2) we did not observe any significant difference in χ^2. The difference produced by a larger number of rings is appreciable only in the higher frequency region of the power spectra, where our data error bars are large. We combined the QPO with the broad-band variability by multiplication instead of addition mode (the total flux is the product between the two types of variability instead of their sum, see IK13). Although our observations do not allow us to differentiate between the multiplicative and the additive mode, the multiplicative mode is based on the more physically realistic scenario that the precession modulates the emission. Because of the inner flow precession, the brightest part of the inner flow moves in and out of the observer's line of sight and angles to the line of sight vary, causing variations in the projected area (IK13).
For all the fits we fixed the parameters ζ, λ, κ, the bending wave radius $r_{\rm bw}$, the emissivity γ, the mass M, and the dimensionless spin parameter of the BH a_*. The free parameters are Σ_0, the truncation radius $r_{\rm o}$, the fractional variability F_{var}, the fundamental QPO width $\Delta\nu$, and the rms of the fundamental and harmonic QPOs.
Fig. 2.9 shows the PROPFLUC fit of the third observation, Table 2.2 shows the best-fitting parameters, the main QPO frequency ν_{QPO}, and the reduced χ^2_ν for each of the five observations considered, and Fig. 2.10 shows the evolution of the physical parameters with time.
All parameter values show a clear trend. Σ_0 increases from ≈ 3.5 to ≈ 13 continuously. In the same way, the truncation radius decreases from ≈ 24 $R_{\rm g}$ to ≈ 10 $R_{\rm g}$, indicating an average truncation radius recession speed of about 2 km/h. The fractional variability increases from ≈ 18 to ≈ 23% in the first three observations and shows no significant change beyond. The fundamental QPO width increases continuously with time while its rms decreases from ≈ 18 to ≈ 10%.

2.5 Discussion

As described by Stiele et al. (2012), the source follows the usual behaviour of BHBs. Using the state classification described in Belloni (2010), the source either is in the LHS or in the HIMS during the first five observations. Between observations 5 and 7 we observe rms dropping off (from ≈ 18 to ≈ 7%) simultaneously to the detection of radio emission (Miller-Jones et al. 2011), and in observation 7, we identify a significant (4.7σ, single trial) type-B QPO in the 2.87–20.20 keV energy band. This shows that the source entered the SIMS between ob-

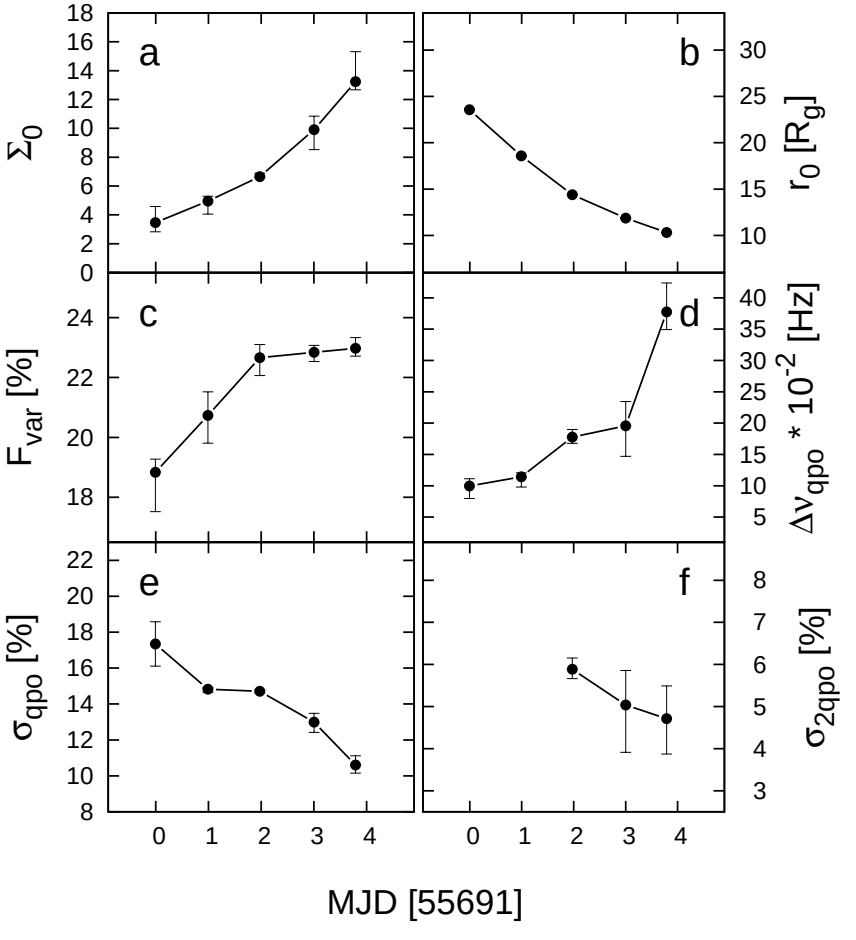

Figure 2.10: PROPFLUC best-fitting parameters versus time. All the points were plotted with 1σ error bars.

servations 5 and 7, a conclusion previously considered by Stiele et al. (2012), who however did not report the QPO in observation 7.

We used the PROFLUC model (ID11; ID12; IK13) for fitting the power spectra of the first five observations in the 2.87–20.20 keV band. As described in section 2.1, the model assumes that the variability generated by each region of the inner flow peaks at the local viscous time-scale. This is contrary to results of General Relativistic Magneto-Hydrodynamic simulations, which display variability peaking approximately at the local *orbital* time-scale (Armitage & Reynolds 2003; Dexter & Fragile 2011). These simulations, however, disagree with obser-

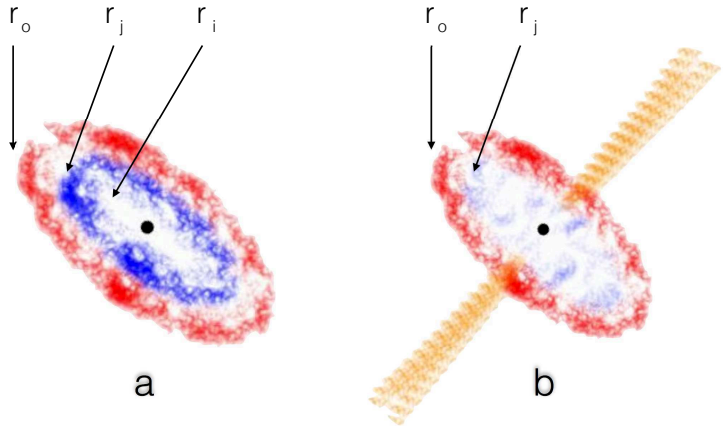

Figure 2.11: Schematic representation of the transition between LHS (a) and SIMS (b).

vations since BHBs display a high-frequency break in their power spectra at $\nu \lesssim 10$ Hz, whereas simulations assuming a $10M_{\odot}$ BH exhibit variability up to a high frequency break of ≈ 100 Hz, $\approx$1/3 the orbital frequency at 5 $R_{\rm g}$ (e.g., fig. 10 of Dexter & Fragile 2011). The same discrepancy with simulations is seen for active galactic nuclei. For example, the power spectrum of the Seyfert 1 galaxy NGC 4051 displays a break at $\approx 8 \times 10^{-4}$ Hz (Vaughan et al. 2011), whereas the orbital frequency at 5 $R_{\rm g}$ is $\approx 1.7 \times 10^{-2}$ Hz (assuming a BH mass of $\approx 1.7 \times 10^{6} M_{\odot}$). While it is clearly important that this inconsistency is addressed, we note that assuming the characteristic variability time-scale to be orbital rather than viscous would require an inner flow radius of $r_i \approx 75 R_g$ in order to fit the observed power spectra in this paper. This strongly implies that considering the viscous time-scale is more appropriate for BHs, even in light of evidence that pulsars show variability on the orbital time-scale (Revnivtsev et al. 2009).

In order to better explore the possibilities of the model, we ran a series of computations varying its physical parameters. The model parameter mainly affecting QPO frequency is the truncation radius $r_{\rm o}$, which sets the physical dimension of the precessing inner flow, responsible for the QPO generation. As can be seen in Fig. 2.8, most other parameters (but not Σ_0 and F_{var}) also affect the QPO frequency. Every parameter affects the broad-band noise in a characteristic way. For example, varying the bending wave radius r_{bw} we observe evident correlated variations in peak frequency and slope of the high frequency tail of the broad-band component, varying ζ has almost no effect on the high frequency tail, but clearly changes its width and peak frequency, Σ_0 variations affect only the peak frequency. Variations in BH spin a_* have no effect at all on the broad-band component. It is clear that in order to constrain all physical parameters of the model, very good counting statistics are needed to clearly define

the precise shape of the broad-band noise.

In our fits we fixed λ, ζ, κ, r_{bw}, the emission coefficient γ, BH mass M, and spin a_*. Fixing λ, ζ, κ, and r_{bw} implies fixing the surface density profile throughout the rising phase of the outburst. ID12 noticed that an evolution of r_{bw} is expected when the truncation radius decreases, because when the inner flow is illuminated by an increasing number of disc photons, its electron temperature drops and hence its scaleheight factor, h/r, collapses. In our fit we fixed the bending wave radius because our spectra are too noisy above 10 Hz to measure it independently, so we are not able to eliminate the degeneracy between r_o and r_{bw} in determining the QPO frequency. For this reason we caution that the fit results in this work were obtained fixing the density profile of the inner flow (except for $r_{\rm o}$), so that they must be interpreted with care.

The QPO frequency increase over observations 1–5 corresponds to an $r_{\rm o}$ decrease from ≈ 24 to $\approx 10\ R_{\rm g}$. From spectral analysis, Stiele et al. (2012) report a constant truncation radius ($r_{\rm o}$ $\approx$ 20-22 km) throughout the whole outburst without specifying uncertainties. As described before, the PROFLUC physical parameter mainly affecting the QPO frequency is $r_{\rm o}$, so that, in order to fit QPOs during the rising phase of the outburst, the truncation radius has to vary during this phase. Because of the data quality, RXTE spectral range, and the limitations of the model used by Stiele et al. (2012) (see Merloni et al. 2001), the spectral estimation of the inner radius is of limited use in the comparison with the PROPFLUC results.

The surface density normalization constant Σ_0 increases from ≈ 3.5 to ≈ 13.2. For a given annulus in the inner flow, Σ_0 is proportional to surface density divided by mass accretion rate (equation 2.1). During the rising phase of the outburst the mass accretion rate increases with time, so the Σ_0 increase means that the surface density increases faster than the mass accretion rate, i.e. matter is accumulating in the flow during this phase of the outburst. This is consistent with the results of ID12 on XTE J1550-564.

The fractional variability F_{var} shows a linear increasing trend in the first three observations and holds almost stable ($\approx 23\%$) in the other observations. The fractional variability does not give us any detailed information about the physical mechanisms producing the variability, but it quantifies the turbulent nature of the accreting material per radial decade. ID12 show that F_{var} increases continuously decreasing truncation radius, but we do not observe the same trend over all the observations, possibly because in our fit we fixed the bending wave radius.

As described, timing properties change in observations 6 and 7, compared to observations 1–5, with simultaneous radio emission. The changes are more abrupt at higher photon energies (Fig. 2.5). The rms decreases from ≈ 18 to $\approx 7\%$ and L_{LF} frequency decreases as well, breaking the monotonically increasing trend of the first five observations. Observations 6 and 7 also show a prominent low-frequency broad-band component ($L_{\rm b}^{-}$) that is not understandable in terms of the two-component power spectra produced by PROFLUC, which is the reason why we applied PROFLUC only to the first five observations. Belloni et al. (1997) consider emptying and replenishing cycles of the inner accretion disc, caused by viscous thermal instability, to explain variability on time-scale of tens of minutes in GRS 1915+105. Feroci et al. (1999) suggest material ejection to explain both spectral and timing properties of

this same source, also in view of the correlation between the innermost disc temperature and the QPO frequency observed by Muno et al. (1999). Similarly, assuming the truncation radius reaches its smallest value at maximum luminosity (and so maximum accretion rate), the ν_{QPO} decrease observed in our data can be explained by the depletion of inner flow material between $r_{\rm i}$ and a certain radius $r_{\rm j}$ ($r_{\rm o} > r_{\rm j} > r_{\rm i}$) simultaneously to the radio emission. This scenario is shown schematically in Fig. 2.11. This depletion can be caused by either ejection or increased accretion between $r_{\rm i}$ and $r_{\rm j}$. As a consequence, the surface density between r_i and r_j drops off, so that the high frequencies (corresponding to smaller radii) contribute less to the QPO frequency (equation 2.2) and F_{var} (so the noise level) decreases.
The low frequency broad-band component $L_{\rm b}^{-}$ might be explained in this scenario as the result of mass accretion rate fluctuations propagating from the disc towards the inner flow.

2.6 Conclusions

We analysed the evolution of MAXI J1543-564 during its 2011 outburst identifying the transition between LHS/HIMS and SIMS, occurring between observations 5 and 6. Analysing the source in different energy bands, we found that in this transition changes in rms are more evident at higher photon energy. Using the mass accretion rate fluctuation/precessing flow model PROPFLUC, we provided a physical interpretation of the first five observations in terms of truncation radius, fractional variability, mass accretion rate, and surface density evolution. We suggest that the source behaviour in observation 6 and 7, and so the transition between LHS and SIMS, might be caused by mass depletion in the innermost part of the accretion flow due to ejection and/or enhanced accretion associated with the simultaneous radio emission. This physical scenario is consistent with our timing analysis in different energy bands.

Table 2.1: Multi-Lorentzian best-fitting parameters for observations 1-7 in four different energy bands.

Date (MJD)	Power spectrum component	Energy band (keV)	ν (Hz)	Q	rms (%)	σ	χ^2_{red}
		2.87–4.90	$1.07^{+0.04}_{-0.05}$	$4.17^{+2.07}_{-1.01}$	$17.97^{+1.85}_{-1.85}$	4.86	1.03
		4.90–9.81	$1.03^{+0.03}_{-0.02}$	$3.42^{+1.10}_{-0.84}$	$20.80^{+1.57}_{-1.64}$	6.36	1.07
55691.089(1)	L_{LF}	9.81–20.20	$1.04^{+0.02}_{-0.02}$	$8.38^{+2.55}_{-2.55}$	$17.42^{+2.07}_{-2.07}$	4.21	0.81
		2.87–20.20	$1.06^{+0.02}_{-0.02}$	$5.26^{+1.34}_{-1.05}$	$17.48^{+1.27}_{-1.24}$	7.05	0.88
		2.87–4.90	$1.72^{+0.02}_{-0.03}$	$6.54^{+3.07}_{-1.64}$	$13.37^{+1.11}_{-1.06}$	6.32	1.17
		4.90–9.81	$1.75^{+0.02}_{-0.01}$	$10.91^{+7.32}_{-2.63}$	$14.34^{+0.92}_{-0.89}$	8.04	0.87
55692.084(2)	L_{LF}	9.81–20.20	$1.74^{+0.02}_{-0.02}$	$6.46^{+2.68}_{-1.48}$	$18.69^{+1.57}_{-1.47}$	6.35	0.83
		2.87–20.20	$1.75^{+0.01}_{-0.01}$	$7.81^{+1.55}_{-1.15}$	$14.74^{+0.67}_{-0.66}$	11.17	0.91
		2.87–4.90	$2.97^{+0.02}_{-0.02}$	$7.82^{+1.61}_{-1.14}$	$11.25^{+0.57}_{-0.54}$	10.49	1.04
		4.90–9.81	$2.97^{+0.01}_{-0.01}$	$9.51^{+1.28}_{-0.98}$	$16.06^{+0.43}_{-0.43}$	18.93	1.04
55693.066(3)	L_{LF}	9.81–20.20	$2.97^{+0.01}_{-0.02}$	$11.06^{+4.25}_{-2.07}$	$16.37^{+0.72}_{-0.67}$	12.18	0.88
		2.87–20.20	$2.97^{+0.01}_{-0.01}$	$8.60^{+0.69}_{-0.60}$	$14.60^{+0.29}_{-0.29}$	25.14	1.22
		2.87–4.90	$4.39^{+0.03}_{-0.07}$	$12.35^{+5.33}_{-5.33}$	$8.37^{+1.06}_{-0.86}$	4.86	0.84
		4.90–9.81	$4.42^{+0.05}_{-0.05}$	$9.18^{+1.44}_{-1.15}$	$14.57^{+1.00}_{-1.00}$	7.30	0.89
55694.095(4)	L_{LF}	9.81–20.20	$4.46^{+0.07}_{-0.05}$	$7.00^{+1.57}_{-1.10}$	$19.62^{+1.55}_{-1.60}$	6.14	1.00
		2.87–20.20	$4.381^{+0.02}_{-0.02}$	$11.27^{+3.19}_{-1.87}$	$13.01^{+0.51}_{-0.49}$	13.18	0.91
		2.87–4.90	$5.67^{+0.15}_{-0.14}$	$6.61^{+9.13}_{-2.64}$	$7.35^{+1.65}_{-1.26}$	2.93	1.04
		4.90–9.81	$5.84^{+0.10}_{-0.11}$	$8.48^{+2.52}_{-1.32}$	$11.10^{+1.04}_{-1.01}$	5.50	1.07
55694.884(5)	L_{LF}	9.81–20.20	$5.83^{+0.11}_{-0.12}$	$6{,}52^{+2.95}_{-1.83}$	$17.41^{+2.66}_{-2.44}$	3.57	0.91
		2.87–20.20	$5.77^{+0.05}_{-0.05}$	$7.98^{+1.20}_{-0.93}$	$10.43^{+0.61}_{-0.61}$	8.53	0.80
		2.87–4.90	$6.52^{+0.42}_{-0.76}$	$3.69^{+7.40}_{-1.87}$	$5.51^{+1.64}_{-1.26}$	2.19	1.10
		4.90–9.81	$5.74^{+0.22}_{-0.22}$	$4.96^{+4.99}_{-2.37}$	$6.08^{+1.42}_{-1.12}$	2.15	1.08
55695.669(6)	L_{LF}	9.81–20.20	$6.19^{+0.27}_{-0.36}$	$4.45^{+8.57}_{-2.31}$	$12.84^{+2.87}_{-2.67}$	2.40	1.08
		2.87–20.20	$5.75^{+0.41}_{-0.49}$	$1.81^{+1.18}_{-0.86}$	$6.35^{+2.05}_{-1.28}$	2.49	1.08
		2.87–4.90	4.69	9.00	< 5.32	-	-
		4.90–9.81	$4.83^{+0.10}_{-0.06}$	$10.38^{+4.50}_{-4.60}$	$5.34^{+0.91}_{-0.67}$	3.97	0.84
55696.650(7)	L_{LF}	9.81–20.20	$4.86^{+0.06}_{-0.17}$	$10.49^{+4.62}_{-4.62}$	$11.37^{+1.59}_{-1.42}$	4.00	1.21
		2.87–20.20	$4.69^{+0.05}_{-0.04}$	9.00	$4.76^{+0.36}_{-0.37}$	6.48	1.01
		2.87–4.90	2.28	4.55	< 6.48	-	-
		4.90–9.81	$2.28^{+0.56}_{-0.09}$	$4.55^{+5.92}_{-3.71}$	$13.05^{+7.56}_{-2.57}$	2.53	1.07
55691.089(1)	L^{+}_{LF}	9.81–20.20	$2.99^{+0.17}_{-0.14}$	4.55	< 22.34	$14.73^{+3.19}_{-3.19}$	0.81
		2.87–20.20	$2.17^{+0.15}_{-0.14}$	6.78	$5.42^{+2.10}_{-2.12}$	1.29	0.88
		2.87–4.90	$4.03^{+0.21}_{-0.13}$	$5.18^{+4.74}_{-2.32}$	$10.31^{+2.34}_{-1.86}$	2.78	1.17
		4.90–9.81	4.03	5.18	< 12.69	-	-
55692.084(2)	L^{+}_{LF}	9.81–20.20	-	-	-	-	
		2.87–20.20	4.03	5.18	< 8.00	-	-
		2.87–4.90	$5.87^{+0.16}_{-0.15}$	$5.18^{+4.74}_{-2.32}$	$6.24^{+1.27}_{-1.25}$	2.50	1.04
		4.90–9.81	$5.87^{+0.16}_{-0.15}$	$7.29^{+1.88}_{-1.88}$	$6.57^{+1.15}_{-1.02}$	3.23	1.04
55693.066(3)	L^{+}_{LF}	9.81–20.20	-	-	-	-	-
		2.87–20.20	$5.85^{+0.11}_{-0.11}$	$6.55^{+2.89}_{-1.53}$	$6.16^{+0.83}_{-0.73}$	4.23	1.22
		2.87–4.90	8.86	6.69	< 9.50	-	-
		4.90–9.81	8.86	5.88	$6.87^{+3.06}_{-2.21}$	1.55	0.89
55694.095(4)	L^{+}_{LF}	9.81–20.20	-	-	-	-	-
		2.87–20.20	$8.86^{+0.26}_{-0.28}$	$6.69^{+3.02}_{-3.02}$	$5.88^{+1.60}_{-1.16}$	2.55	0.91

Table 2.1: Continued.

Date (MJD)	Power spectrum component	Energy band (keV)	ν (Hz)	Q	rms (%)	σ	χ^2_{red}
		2.87–4.90	-	-	-	-	-
		4.90–9.81	3.30	0	< 30.16	-	-
55691.089(1)	L_b	9.81–20.20	-	-	-	-	-
		2.87–20.20	$3.30^{+1.33}_{-0.87}$	0	$19.55^{+2.37}_{-2.32}$	4.22	0.88
		2.87–4.90	-	-	-	-	-
		4.90–9.81	$3.641^{+0.86}_{-0.67}$	0	$22.12^{+1.71}_{-1.67}$	6.64	0.87
55692.084(2)	L_b	9.81–20.20	$7.881^{+7.40}_{-3.33}$	0	$24.65^{+4.60}_{-3.73}$	3.31	0.83
		2.87–20.20	$3.61^{+0.41}_{-0.36}$	0	$21.38^{+0.89}_{-0.89}$	11.96	0.91
		2.87–4.90	$4.813^{+0.74}_{-0.69}$	0	$18.71^{+1.42}_{-1.21}$	7.72	1.04
		4.90–9.81	$3.755^{+0.52}_{-0.50}$	0	$21.25^{+1.25}_{-1.27}$	8.38	1.04
55693.066(3)	L_b	9.81–20.20	$4.261^{+0.66}_{-0.63}$	0	$27.40^{+1.67}_{-1.69}$	8.09	0.88
		2.87–20.20	$3.77^{+0.27}_{-0.27}$	0	$19.98^{+0.61}_{-0.63}$	15.83	1.22
		2.87–4.90	$4.64^{+0.74}_{-0.69}$	0	$15.14^{+1.74}_{-1.69}$	4.48	0.83
		4.90–9.81	$3.44^{+0.78}_{-0.69}$	0	$20.28^{+1.78}_{-1.68}$	6.02	0.89
55694.095(4)	L_b	9.81–20.20	$1.71^{+0.84}_{-0.49}$	0	$21.61^{+3.04}_{-2.47}$	4.38	1.00
		2.87–20.20	$3.42^{+0.52}_{-0.49}$	0	$18.19^{+1.70}_{-1.05}$	8.69	0.91
		2.87–4.90	$5.36^{+2.01}_{-1.63}$	0	$13.18^{+1.92}_{-1.87}$	3.52	1.04
		4.90–9.81	$4.36^{+0.80}_{-0.72}$	0	$20.28^{+1.28}_{-1.24}$	8.11	1.07
55694.884(5)	L_b	9.81–20.20	$3.54^{+1.34}_{-0.98}$	0	$25.89^{+3.45}_{-2.95}$	4.39	0.91
		2.87–20.20	$3.69^{+0.67}_{-0.57}$	0	$16.90^{+0.99}_{-0.93}$	8.53	0.80
		2.87–4.90	-	-	-	-	-
		4.90–9.81	$2.50^{+0.23}_{-0.22}$	$1.69^{+0.89}_{-0.70}$	$6.94^{+1.17}_{-1.00}$	3.48	1.08
55695.669(6)	L_b	9.81–20.20	-	-	-	-	-
		2.87–20.20	$3.08^{+1.04}_{-0.91}$	0	$8.56^{+1.42}_{-1.38}$	3.10	1.08
		2.87–4.90	1.55	0	< 5.03	-	-
		4.90–9.81	$1.55^{+0.94}_{-0.56}$	0	$6.68^{+1.25}_{-1.01}$	3.32	0.84
55696.650(7)	L_b	9.81–20.20	-	-	-	-	-
		2.87–20.20	-	-	-	-	-
		2.87–4.90	$0.06^{+0.05}_{-0.03}$	0	$3.27^{+0.84}_{-0.76}$	2.15	1.04
		4.90–9.81	0.06	0.13	< 5.07	-	-
55694.884(5)	L_b^-	9.81–20.20	-	-	-	-	-
		2.87–20.20	$0.057^{+0.05}_{-0.02}$	$0.13^{+0.48}_{-0.48}$	$3.54^{+0.90}_{-0.58}$	3.04	0.80
		2.87–4.90	$0.19^{+0.06}_{-0.05}$	0	$4.76^{+0.56}_{-0.53}$	4.49	1.10
		4.90–9.81	$0.26^{+0.76}_{-0.11}$	0	$4.62^{+0.92}_{-0.81}$	2.86	1.08
55695.669(6)	L_b^-	9.81–20.20	$0.52^{+2.04}_{-0.26}$	0	$10.47^{+6.41}_{-1.98}$	2.64	1.08
		2.87–20.20	$0.13^{+0.04}_{-0.03}$	0	$4.42^{+0.47}_{-0.44}$	5.00	1.08
		2.87–4.90	-	-	-	-	-
		4.90–9.81	-	-	-	-	-
55696.650(7)	L_b^-	9.81–20.20	-	-	-	-	-
		2.87–20.20	$0.27^{+0.39}_{-0.15}$	0	$2.49^{+0.79}_{-0.56}$	2.23	0.91

Table 2.1: Continued.

Date (MJD)	Power spectrum component	Energy band (keV)	ν (Hz)	Q	rms (%)	σ	χ^2_{red}
55692.084(2)	?	2.87–4.90	$0.561^{+0.01}_{-0.04}$	$6.88^{+18.05}_{-3.11}$	$6.65^{+1.17}_{-0.97}$	3.42	1.10
			$2.74^{+0.06}_{-0.09}$	$6.10^{+11.11}_{-2.33}$	$10.28^{+1.94}_{-1.63}$	3.16	1.10
55695.669(6)	L_{LF} sub?	2.87–4.90	$3.38^{+0.27}_{-0.22}$	$2.40^{+1.61}_{-0.89}$	$6.57^{+1.21}_{-1.15}$	2.85	1.10
		2.87–20.20	$3.11^{+0.12}_{-0.09}$	$6.33^{+3.45}_{-3.45}$	$3.67^{+1.42}_{-0.83}$	2.20	1.10
55696.650(7)	L_{LF} sub?	2.87–20.20	$2.43^{+0.06}_{-0.04}$	9.00	$2.79^{+0.44}_{-0.49}$	2.85	1.01
	L_b ?	2.87–20.20	$1.57^{+0.19}_{-0.12}$	$3.27^{+4.16}_{-1.63}$	$2.70^{+0.78}_{-0.64}$	2.23	1.01

Table 2.2: Best PROPFLUC fit physical parameters for observations 1-5. An $\sim$ symbol indicates that the parameter has been fixed.

Observations	1	2	3	4	5
Σ_0	$3.47^{+1.12}_{-0.64}$	$4.95^{+0.34}_{-0.89}$	$6.65^{+0.25}_{-0.04}$	$9.90^{+0.94}_{-1.37}$	$13.24^{+2.08}_{-0.56}$
F_{var} (%)	$18.84^{+0.44}_{-1.32}$	$20.73^{+0.79}_{-0.92}$	$22.66^{+0.44}_{-0.60}$	$22.84^{+0.23}_{-0.31}$	$22.97^{+0.36}_{-0.26}$
ζ	0	$\sim$	$\sim$	$\sim$	$\sim$
λ	0.90	$\sim$	$\sim$	$\sim$	$\sim$
κ	3.00	$\sim$	$\sim$	$\sim$	$\sim$
r_i	4.50	$\sim$	$\sim$	$\sim$	$\sim$
r_{bw}	8.24	$\sim$	$\sim$	$\sim$	$\sim$
r_o	$23.56^{+0.05}_{-0.07}$	$18.59^{+0.01}_{-0.01}$	$14.40^{+0.00}_{-0.00}$	$11.87^{+0.00}_{-0.01}$	$10.32^{+0.01}_{-0.01}$
$\Delta\nu_{qpo}(10^{-2})$	$9.97^{+1.17}_{-2.01}$	$11.44^{+0.61}_{-1.64}$	$17.75^{+1.23}_{-0.98}$	$19.55^{+3.88}_{-4.86}$	$37.76^{+4.60}_{-2.84}$
σ_{qpo} (%)	$17.34^{+1.24}_{-1.24}$	$14.83^{+0.08}_{-0.18}$	$14.71^{+0.08}_{-0.09}$	$12.99^{+0.50}_{-0.57}$	$10.61^{+0.51}_{-0.46}$
σ_{2qpo} (%)	0.	0.	$5.88^{+0.27}_{-0.22}$	$5.04^{+0.82}_{-0.12}$	$4.71^{+0.78}_{-0.84}$
γ	4.0	$\sim$	$\sim$	$\sim$	$\sim$
$M(M_\odot)$	10.0	$\sim$	$\sim$	$\sim$	$\sim$
a	0.5	$\sim$	$\sim$	$\sim$	$\sim$
ν_{qpo} (Hz)	1.06	1.75	2.97	4.38	5.78
χ^2_ν	0.90	0.91	1.25	0.89	0.99

3

Modelling the cross-spectral variability of the black hole binary MAXI J1659-152 with propagating accretion rate fluctuations

S. Rapisarda, A. Ingram, M. Kalamkar and M. van der Klis

Monthly Notices of the Royal Astronomical Sociaty, 462, 4078

Abstract

The power spectrum of the X-ray fluctuations of accreting black holes often consists of two broad humps. We quantitatively investigate the hypothesis that the lower frequency hump originates from variability in a truncated thin accretion disc, propagating into a large scale-height inner hot flow which, in turn, itself is the origin of the higher frequency hump. We extend the propagating mass accretion rate fluctuations model PROPFLUC to accommodate double hump power spectra in this way. Furthermore, we extend the model to predict the cross-spectrum between two energy bands in addition to their power spectra, allowing us to constrain the model using the observed time lags, which in the model result from both propagation of fluctuations from the disc to the hot flow, and inside the hot flow. We jointly fit soft and hard power spectrum, and the cross-spectrum between the two bands using this model for 5 *Swift X-ray Telescope* observations of MAXI J1659-152. The new double hump model provides a better fit to the data than the old single hump model for most of our observations. The data show only a small phase lag associated with the low frequency hump. We demonstrate quantitatively that this is consistent with the model. We compare the truncation radius measured from our fits with that measured purely by spectral fitting and find agreement within a factor of two. This analysis encompasses the first joint fits of stellar-mass black hole cross-spectra and power spectra with a single self-consistent physical model.

3.1 Introduction

Transient black hole X-ray binaries (BHBs) evolve in very characteristic ways during their outbursts (e.g. Belloni et al. 2005; Remillard & McClintock 2006; Belloni 2010; Gilfanov 2010). A typical BHB outburst passes through a number of different states, each state being defined by particular spectral and timing properties of the source. At the beginning of the outburst, the source is in the low-hard state (LHS): it shows high aperiodic variability (rms $\gtrsim$ 30%) and its energy spectrum is dominated by a hard power law component (photon index $\Gamma \approx 1.7$). As the source luminosity increases, the source moves towards the high-soft state (HSS): the aperiodic variability drops off (rms $\approx 3\%$), the power law softens ($\Gamma \approx 2.4$), and the spectrum becomes dominated by a multi-colour blackbody component peaking in soft X-rays ($\approx$ 1 keV). At the end of the outburst, the source hardens again, turning back in the LHS.

Looking at the power spectrum of the source during the outburst, it is possible to identify several different components representing rapid variability on time scales between ≈ 0.01 and ≈ 100 s, which have different characteristics for each state. In particular, the LHS is usually characterized by the presence of a quasi periodic oscillation (QPO) superimposed on broad band continuum noise. During the evolution of the outburst, all the characteristic frequencies of the power spectral components correlate with hardness (e.g. Wijnands & van der Klis 1998; Psaltis, Belloni & van der Klis 1999; Homan et al. 2001). The initial transition between LHS and HSS usually takes place through intermediate states with spectral and timing properties in between those of LHS and HSS. For example, after the LHS, the source can enter the hard-intermediate state (HIMS) where its spectrum is characterized by the presence of both a disc and a power law component, the aperiodic variability decreases to rms $\approx$ 10-20%, and the QPO superimposed on the broad band noise is still present.

The transition between LHS and HSS can be explained considering two different emitting regions in the accreting flow interacting with each other: an optically thick disc producing the blackbody emission (Shakura & Sunyaev 1973), and an optically thin Comptonizing region producing the power law (Thorne & Price 1975; Sunyaev & Truemper 1979). The latter is often referred to as *corona* (e.g. Melia & Misra 1993; Svensson & Zdziarski 1994; Churazov, Gilfanov & Revnivtsev 2001) or *flow* depending on whether the region is vertically or radially separated from the disc respectively. In particular, the *truncated disc model* (e.g. Esin, McClintock & Narayan 1997; Done, Gierliński & Kubota 2007) considers an optically thick geometrically thin accretion disc truncated at a certain radius $r_{\rm o}$ and an optically thin geometrically thick hot flow extending from $r_{\rm o}$ down to a radius equal or larger than the innermost stable circular orbit (ISCO). At the beginning of the outburst, the truncation radius is still relatively far from the black hole (BH) and the energy spectrum is dominated by the power law component. When the mass accretion rate increases, the truncation radius approaches the BH and the energy spectrum becomes dominated by the blackbody emission. Disc photons up-scatter in the hot flow cooling it down and, as a consequence, the power law softens.

Although the spectral properties of BHBs can be explained considering this two-regime ac-

creting configuration (even though the precise way in which the disc and hot flow interact with each other is not clear), the origin of the fast variability is not fully understood, and a single model explaining both spectral and timing properties is a still matter of debate. The recently proposed model PROPFLUC (Ingram & Done 2011, 2012, hereafter ID11, ID12; Ingram & van der Klis 2013, hereafter IK13) is based on the truncated disc model described above. Additionally, PROPFLUC contains the ingredients of mass accretion rate fluctuations propagating through the hot flow, and precession of the entire hot flow caused by frame dragging close to the BH. Mass accretion rate fluctuations are generated at every radius of the hot flow and propagate towards the BH giving rise to a broad band noise component in the power spectrum (single hump power spectrum). The characteristic time scale of the noise is set by the viscous time scale in the hot flow (e.g. Lyubarskii 1997; Churazov, Gilfanov & Revnivtsev 2001; Arevalo & Uttley 2006). As a consequence of the propagation of the fluctuations, the time variability of the emission from every ring of the flow is correlated (with a time delay). Because the mass accretion rate fluctuations at larger radii, after propagating inward, modulate the amplitude of the fluctuations at smaller radii by multiplication, the process gives rise to the linear rms-flux relation observed in BHBs (Uttley & McHardy 2001; Uttley, McHardy & Vaughan 2005). Meanwhile, the Lense-Thirring (LT) precession of the entire hot flow (Stella & Vietri 1998; Fragile et al. 2007; ID11) produces the QPO at a frequency depending on the mass distribution in the hot flow and on its radial dimension.
Rapisarda et al. (2014) (hereafter RIK14, Chapter 2) presented the first application of PROPFLUC to study the BH candidate MAXI J1543-564. They fitted selected power spectra of the rising phase of the 2011 outburst of the source with the single hump power spectrum calculated by PROPFLUC and traced the evolution of the physical parameters in these observations.
The PROPFLUC version used in RIK14 produces a single hump power spectrum originating from mass accretion rate fluctuations arising only in the hot flow. However, timing analysis of BHBs shows that their power spectrum in the LHS/HIMS is often characterized by a more complex structure than a single hump (e.g Belloni et al. 1997; Homan et al. 2001; Kalamkar et al. 2015b), requiring two or three broad Lorentzians to be fitted (low, mid, and high frequency Lorentzian). Additionally, BHBs often show time lags between different energy bands associated with this broad band variability (e.g., Miyamoto et al. 1988; Nowak, Wilms & Dove 1999). The delay between emission in different energy bands depends on the geometry of the accreting system and can be used to constrain different accretion models (e.g. Miyamoto & Kitamoto 1989; Böttcher & Liang 1999; Misra 2000; Nowak et al. 1999b; Kotov et al. 2001; Arevalo & Uttley 2006).
Combining spectral and timing analysis it is possible to obtain clues about the origin of the different power spectral components. In particular, Wilkinson & Uttley (2009), on the basis of measurements of variability amplitudes of X-ray spectral components, suggested that low frequency noise is the result of intrinsic variability generated in the disc and propagating through the flow. By its very nature, propagation also predicts time lags between soft and hard energy bands, but up to now these two aspects of the propagation hypothesis have never been jointly considered in a quantitative analysis.

As pointed out in IK13, with the model PROPFLUC we can simultaneously predict these time lags, the variability amplitudes, and the coherence between energy bands by calculating power spectra at different energies, and cross-spectra between those energies. These predictions can then jointly be fitted to observed power and cross-spectra. The model can also be adapted to simulate extra disc variability and produce a two-hump power spectrum by considering mass accretion rate fluctuations generated both in the disc and in the flow, all propagating towards the BH. Fits to cross- and power spectra of BHBs in the LHS/HIMS characterized by a two-hump profile can then be attempted using observations spanning the low energy range where the disc emission is concentrated.
In this paper, we analyze data from MAXI J1659-152, a BH discovered in 2010 (Mangano et al. 2010; Negoro et al. 2010). During its 2010 outburst, MAXI J1659-152 followed the usual behavior observed in BHB outbursts (Muñoz-Darias et al. 2011). Previous timing analysis of the source using the *Rossi X-ray Timing Explorer* (RXTE; Jahoda et al. 1996) and *Swift* (Gehrels et al. 2004) observations (Kalamkar et al. 2011; Kalamkar et al. 2015b), showed that its power spectra in the HIMS are characterized by several broad band components with characteristic frequencies between ≈ 0.001 and ≈ 5 Hz. We explore the hypothesis put forward by Kalamkar et al. (2015b) that some of this enhanced low frequency variability originates in the disc by performing joint fits of the power and cross-spectra of MAXI J1659-152 in the HIMS using *Swift* XRT data in two different energy bands (0.5 - 2.0 keV and 2.0 - 10.0 keV). The *Swift* XRT data allow us to study the source from the beginning of the outburst (RXTE started observing the source 3 days later) in an energy range where the disc emission is significant.
Sec. 3.2 is dedicated to the description of the new two-hump version of PROPFLUC, Sec. 3.3 briefly describes how we reduced and analyzed the data, and in Sec. 3.4 and Sec. 3.5 we present and discuss the results of our fits, respectively. By a strictly quantitative analysis, we find, perhaps counterintuitively, that the small lag observed in the broadband noise between these two energy bands is entirely consistent with mass accretion rate fluctuations in the disc propagating to the hot flow.

3.2 The new PROPFLUC model

PROPFLUC (ID11, ID12, IK13) is a model assuming a truncated disc/hot flow geometry, with mass accretion rate fluctuations propagating through a precessing hot flow. Here, we introduce two extra features to the model: 1) we consider that variability can also be generated in the disc, which then propagates to the hot flow on a viscous infall time; 2) we improve the model so that it is now possible to simultaneously fit power spectra in two different energy bands, and the complex cross-spectrum between these two bands. The cross-spectrum contains information on the power in each of these bands, the phase lags between the bands, and also the coherence between the bands. In order to fit the cross-spectrum, we introduce a formalism to include arbitrary QPO phase lags, which allows us to concentrate on physical

modelling of the broad band noise (see Appendix B).

3.2.1 Propagating fluctuations and disc variability

The accreting region producing the variability extends from an inner radius $r_{\rm i}$ equal or larger than the innermost stable circular orbit (r_{ISCO}) up to a radius $r_{\rm d}$ much smaller than the outer edge of the disc (in this paper we use the convention that lowercase r corresponds to radial coordinate scaled by gravitational radius: $r = R/R_{\rm g}$, where $R_{\rm g} = GM/c^2$). The truncation radius $r_{\rm o}$ is in between $r_{\rm i}$ and $r_{\rm d}$, dividing the region into hot flow ($r_{\rm i} < r < r_{\rm o}$) and varying disc ($r_{\rm o} < r < r_{\rm d}$, hereafter just "disc"). The geometry of the accreting region ($r_{\rm d} > r_{\rm o} > r_{\rm i}$) is sketched in Fig. 3.1: red and blue horizontal thick lines indicate disc and hot flow respectively. From the computational point of view, the hot flow is split into rings that are equally logarithmically spaced, so that $dr/r = constant$ for each ring, where r and dr are radial coordinate and thickness of the ring respectively. The power spectrum of mass accretion rate fluctuations generated in each ring of the hot flow is a zero-centered Lorentzian with the width set by the local viscous frequency $\nu_{v,flow}(r)$ and having amplitude $\sigma_0^2 = (F_{var}/\sqrt{N_{dec}})^2$, where the model parameters F_{var} and N_{dec} are the fractional variability produced per radial decade and the number of rings per radial decade, respectively. The right part of Fig. 3.1 ($r < r_{\rm o}$ = 60) shows the dependence of viscous frequency (green solid line) and σ_0 (purple dashed line) on radius in the hot flow. Whereas the variability amplitude is assumed to be constant within the hot flow, the viscous frequency in there is described by a smoothly broken power-law (see Eq. 2 and 3 in ID12). This derives from our assumption that the surface density in the hot flow is characterized by a smoothly broken power-law, since, from mass conservation, the viscous frequency in every ring is inversely proportional to the average surface density (Frank, King, & Raine 2002). The power spectrum of the emission produced by mass accretion rate fluctuations generated in each ring and propagating through the hot flow towards the BH, is a broad band component (single "hump" power spectrum) with approximately constant rms (i.e. power $P(\nu) \propto 1/\nu$) between low and high frequency breaks, where the low frequency break is the viscous frequency at the outer edge of the hot flow $\nu_{v,flow}(r_{\rm o})$ and the high frequency break depends on the highest frequency produced in the hot flow, but it is also influenced by coherent addition of the variability emitted from different regions of the hot flow.

The disc is also split into rings that are equally logarithmically spaced, and the number of rings per radial decade, i.e. the model radial resolution, is the same as in the hot flow ($N_{dec,flow} = N_{dec,disc} = N_{dec}$). The power spectrum of mass accretion rate fluctuations generated in each ring within the disc region is also characterized by a zero-centered Lorentzian with width set by the local viscous frequency. The left part of the plot in Fig. 3.1 ($r_{\rm o}$ = 60 $< r <$ $r_{\rm d}$ = 160) shows the dependence of viscous frequency (green solid line) and variability amplitude (purple dashed line) on radius for the disc. The variability amplitude is assumed to peak at the inner edge of the disc, $r_{\rm o}$, and drop off outside of this with a Gaussian dependence on radius. The peak and the width of this Gaussian, $\sigma_0 N_{var}$ and Δd, respec-

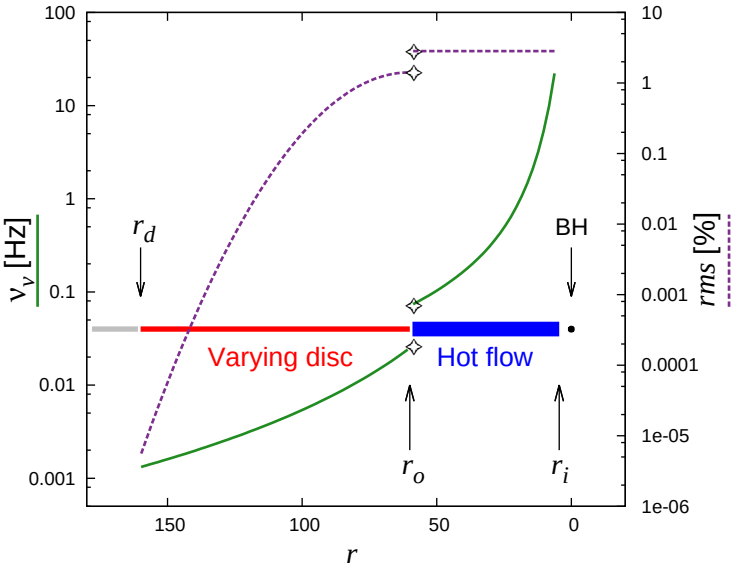

Figure 3.1: Variability produced (purple dashed line) and viscous frequency (green solid line) versus radial coordinate r for the entire mass accretion rate fluctuations propagating region (disc + hot flow). Blue and red horizontal lines indicate the hot flow and the disc respectively, the grey horizontal line ($r > 160$) corresponds to the disc region that does not contribute to the variability. Both viscous frequency and amount of variability produced by every ring, are discontinuous at the truncation radius r_o (star symbols).

tively, are both model parameters. We set $r_d = r_o + 5\,\Delta d$, since to a very good approximation there is no variability outside this radius. For the disc we assume the viscous frequency profile of a Shakura-Sunyaev disc with constant viscosity parameter and scale-height (Shakura & Sunyaev 1973):

$$\nu_{v,disc}(r) = \nu_{d,max}(r/r_o)^{-3/2} \tag{3.1}$$

where the viscous frequency at the inner edge of the disc, $\nu_{d,max} \equiv \nu_{v,disc}(r_o)$, is a model parameter. Mass accretion rate fluctuations generated in every ring, from r_i to r_d, propagate towards the BH on a viscous infall time. We see that the model allows for a discontinuity in the viscous frequency at the truncation radius as the accretion flow transitions from disc to hot flow (see Fig. 3.1, star symbols). It is this jump in frequency that results in two humps in the predicted power spectrum, with the lower frequency hump contributed by the disc (since the viscous frequency is lower here) and the higher frequency hump contributed by the hot flow.

As with previous versions of the model, we assume that the count rate observed in a given energy band can be represented as a linear combination of the mass accretion rate in each

ring. The count rate in a "hard band", $f_h(t)$, is given by:

$$f_h(t) = \sum_{j=1}^{N} h(r_j)\dot{m}(r_j, t) \tag{3.2}$$

where N is the *total* number of rings between $r_{\rm i}$ and $r_{\rm d}$ (i.e. N is the number of rings in the hot flow plus the number of rings in the disc), the emissivity function $h(r_j)$ is the mean count rate observed from the j^{th} ring in this energy band, and $\dot{m}(r_j, t)$ represents the varying mass accretion rate in the j^{th} ring. If we know (or, rather, make an assumption for) the mean spectrum emitted from each ring and the detector response, we can directly calculate $h(r_j)$ from the counts spectrum of the j^{th} ring. For the flow, in the absence of a standard model for the spectrum as a function of radius, we simply parameterize $h(r_j)$ as a power-law function of r with an inner boundary condition given by the surface density profile (see Appendix A and ID12).

For the disc, in contrast, we do have a standard model: a blackbody with temperature $\propto r^{-3/4}$ and luminosity $\propto r^{-3}$ (Shakura & Sunyaev 1973). To calculate each $h(r_j)$ for the disc, we start with the blackbody spectrum from radius r_j (see Fig. 3.3), convolve it with the telescope response, and integrate over the energy range of interest (see Appendix A for details).

For both the disc and hot flow, we expect the spectrum to be harder for smaller r, which translates to a hard band emissivity function $h(r_j)$ being a steeper function of r (i.e. more centrally peaked) than a soft band emissivity function $s(r_j)$. We note that our assumption of linearity relies on variability in disc temperature, $T(r, t)$, being much smaller than the variability in $\dot{m}(r, t)$. This is a good assumption, since $T \propto \dot{m}^{1/4}$. The maximum temperature reached by the disc (at $r_{\rm o}$ since we do not employ the zero-torque boundary condition - see Appendix A), $T_{d,max}$, is a model parameter.

We also need to parameterize the normalization of the disc spectrum. The absolute normalization is not of interest to us, but the *fraction* of the total photons observed in a given band that are contributed by the disc *is* of interest. In this paper, we consider two energy bands, a soft band s and a hard band h. The fraction of observed disc photons in the soft band, x_s, is a model parameter which, along with $T_{d,max}$, can be measured from a spectral fit. The disc fraction in the hard band, x_h, can be calculated from x_s and the hardness ratio HR (the ratio between counts in the hard and soft band), which can be measured directly from the soft and hard light curves (see Appendix A). Tab. 3.2 lists all the new model parameters with a short description.

We compute the power spectrum of $f_s(t)$ and $f_h(t)$ (0.5-2.0 keV and 2.0-10 keV, respectively), and the cross-spectrum between $f_s(t)$ and $f_h(t)$ using the formulae from IK13. Fig. 3.2(a) shows soft and hard power spectra produced considering variability generated in both the disc and the hot flow (solid line) and the only hot flow (dashed line). Introducing a propagating region in the disc has two evident effects: 1) the power spectrum consists of two broad band components (double hump power spectrum), a low frequency one generated in the disc and a high frequency one generated in the hot flow; 2) the total power in the disc + hot flow case is higher than the only hot flow case because of extra variability coming from the disc.

Due to propagation, the hot flow emission lags the disc emission. Since the disc emits a softer spectrum than the hot flow, we expect disc variability to contribute a hard phase lag (i.e. hard photons lagging soft photons). The amplitude of this phase lag depends on the viscous infall time and on how the disc and hot flow emission are distributed in the soft and hard band. If $x_s = 1$ and $x_h = 0$, the soft band exclusively contains disc emission and the hard band exclusively contains hot flow emission. Therefore the lag between these energy bands is equal to the lag between the two physical components. For $x_s < 1$ and $x_h > 0$, the lag between energy bands is diluted by a contribution by each physical component to both bands. Panels b and c of Fig. 3.2 show cross-amplitude and phase lag between soft and hard band respectively; for making the plots we set $x_s = 0.8$, $x_h = 0.5$, and we use the response matrix of *Swift*. In this paper, we adopt the usual convention that a positive phase lag corresponds to the hard band lagging soft. With these assumptions, mass accretion rate fluctuations propagating from the disc produce a clear positive phase lag of ≈ 0.065 cycles in the low frequency hump (see Fig. 3.2(c) between ≈ 0.01 and 0.1 Hz).

3.2.2 PROPFLUC outputs

In RIK14 we computed power spectra in a single energy band varying the model parameters related to the hot flow in order to show the relation between canonical multi-Lorentzian fitting parameters and PROPFLUC parameters. Here, we compute soft and hard power spectra, and cross-spectra (implying the phase lags and coherence) between the bands changing the model parameters related to the disc (Tab. 3.2): the maximum viscous frequency in the disc $\nu_{d,max}$ (see Eq. 3.1), the radial extension of the disc Δd, the variability produced in every ring of the disc parameterized as fraction of the hot flow variability N_{var}, and the maximum temperature in the disc $T_{d,max}$. We fix all the parameters related to the hot flow, which are already discussed in RIK14: the surface density constant ($\Sigma_0 = 6$), the smoothly broken power law describing the surface density profile ($\kappa = 3.0$, $\lambda = 0.9$, $\zeta = 0$), the inner radius ($r_{\rm i}$ = 4.5), the transition radius of the smoothly broken power law ($r_{\rm bw}$ = 7.0), the truncation radius ($r_{\rm o}$ = 20), the fractional variability ($F_{var} = 0.3$), the soft and hard band emissivity indices ($\gamma_s = 3.0$, $\gamma_h = 4.5$), the BH mass ($M = 10 M_{\odot}$), and the dimensionless spin parameter ($a_* = 0.5$). We compute soft (0.5-2.0 keV) and hard (2.0-10 keV) power spectra, and cross-spectra between soft and hard band, with a Nyquist frequency of 128 Hz, using a model resolution of $N_{dec} = 35$, fixing the disc fraction in the soft band ($x_s = 0.9$), the hardness ratio ($HR = 1.0$), and including a main QPO with fixed width, rms, and phase lag ($Q = 8$, $\sigma_{qpo} = 5\%$, ϕ_{QPO} = 0.1 cycles). We did not include any other QPO harmonic component for simplicity (in Appendix A we describe the details of including the QPO in the new PROPFLUC model). We computed all the timing products taking into account the *Swift* response matrix and we considered interstellar absorption with a column density of $n_H = 1.7 \times 10^{21}\ atoms/cm^2$. Figs 3.4-3.5 show the results: every column of plots illustrates the effect of varying the value of one particular parameter. The number between square brackets denotes the value of the parameter used for all the other computations.

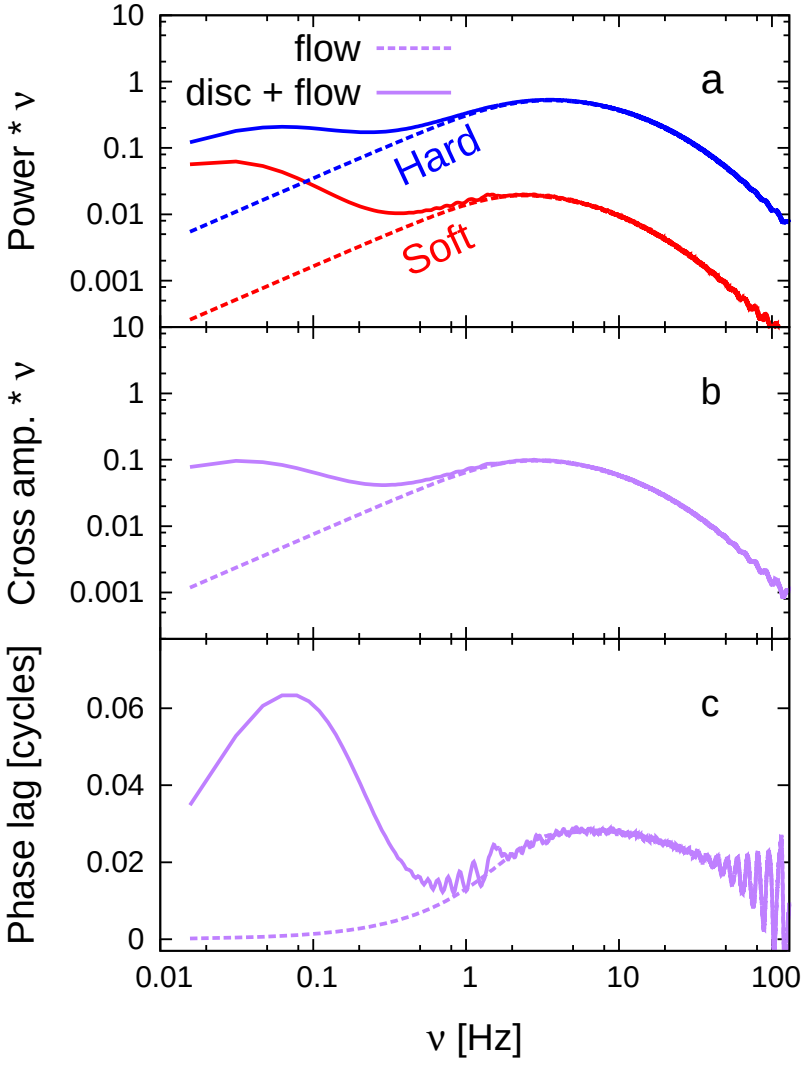

Figure 3.2: Soft (red line) and Hard (blue line) power spectrum (a), cross spectrum (b), and phase lag (c) computed considering mass accretion rate fluctuations propagating only in the hot flow (dashed line) and in the hot flow + disc (solid line). In the second case PROPFLUC produces a two-hump power spectrum with an evident hard lag associated with the low frequency hump.

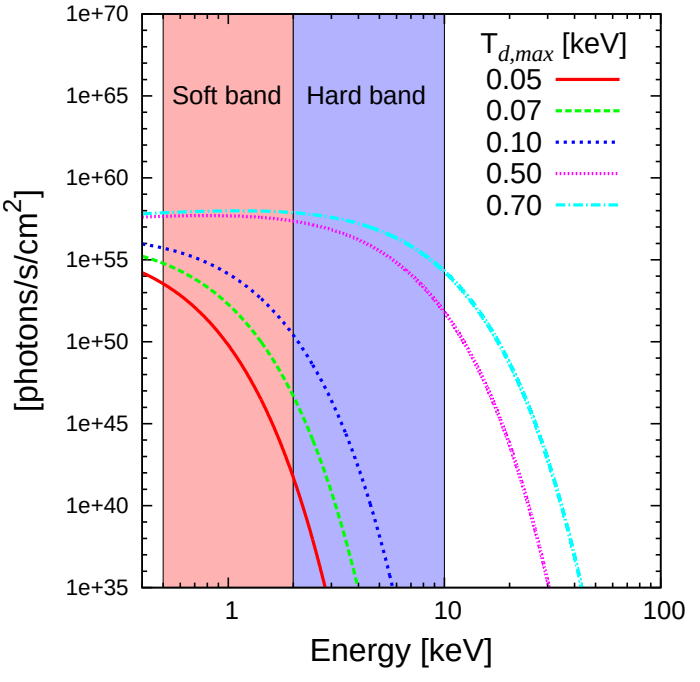

Figure 3.3: Photon flux emitted by a single ring r in the disc characterized by viscous frequency $\nu_{v,disc}(r) = 0.1$. The red and blue regions represent soft and hard band respectively.

In all the plots the shape of soft and hard spectra (dashed and solid line, respectively) are different. This is mainly because of the difference between soft and hard emissivity index (γ_s and γ_h, respectively).
The left column of Fig. 3.4 shows that when $N_{var} = 0$ (red line), i.e. excluding disc variability and considering only mass accretion rate fluctuations propagating in the hot flow, the model converges to the single hump power spectrum version described in RIK14. Increasing N_{var}, the second, lower-frequency, hump starts being distinguishable in all the Fourier products. The disc variability high and low frequency break are the maximum viscous frequency in the disc $\nu_{d,max}$ and $\nu_{v,disc}(r_d)$ respectively (where $r_\mathrm{d} = r_\mathrm{o} + 5\Delta d$). $\nu_{d,max}$ and $\nu_{v,disc}(r_d)$ are both fixed in this case, so that varying N_{var} does not affect the characteristic frequency of the low frequency hump. The phase lags show a different behavior: the peak frequency correlates with N_{var} and at low frequency ($\nu \approx 0.01$ Hz) the phase lags keep the same profile for all the N_{var} values. The relation between N_{var} and the phase lag profile depends on the function describing the variability in the disc, on the disc temperature profile, and on the selected energy bands. In our case, the amount of variability generated in the disc is described by a Gaussian peaking at the truncation radius, with amplitude proportional to N_{var}, and width Δd (see Appendix A). When we increase N_{var}, the variability increases

more steeply with smaller radius close to the truncation radius.
If we increase Δd (Fig. 3.4, right column) we observe in the power and cross-spectrum that the low frequency hump peak frequency decreases and its profile becomes broader. This is because extending the propagating region towards the edge of the disc, the longer time scale variability contribution becomes more important. For the same reason, increasing Δd causes the phase lags to increase at lower frequency.
The left column of Fig. 3.5 shows the effects of varying the maximum viscous frequency in the disc ($\nu_{d,max}$). Varying $\nu_{d,max}$ affects the size of the viscous frequency trend discontinuity between the disc and the hot flow (i.e. Fig. 3.1). The bigger this jump the more evident is the two-hump profile. Decreasing $\nu_{d,max}$ causes the low frequency hump peak to move to lower frequency. The phase lag peak frequency correlates with $\nu_{d,max}$, as expected.
Finally, the right column of Fig. 3.5 shows the effects of varying the maximum temperature in the disc ($T_{d,max}$). Increasing $T_{d,max}$ from 0.05 to 0.1 keV has little consequence on the power and cross spectrum, while we see more evident changes when $T_{d,max}$ varies from 0.1 to 0.5 keV. In particular, the frequency of the phase lag peak is larger than the maximum viscous frequency in the disc ($\nu_{d,max} = 0.1$) and it moves to lower frequencies when $T_{d,max}$ increases.
This behavior can be explained looking at Fig. 3.3. This plot shows the blackbody emission coming from the ring generating 0.1 Hz variability. When the disc temperature is between 0.05 and 0.1 keV, the blackbody emission is almost entirely detected in the soft band. Because a small fraction of photons is still detected in the hard band, the phase lag at 0.1 Hz is a bit lower than its potential maximum (we expect maximum phase lag when the soft band perfectly matches the disc emission, so when x_s = 1), so that the phase lag peak appears to be at frequencies larger than 0.1 Hz. Increasing $T_{d,max}$ from 0.1 to 0.5 keV means moving the blackbody peak to higher energies, so that a larger part of the blackbody emission is now detected in the hard band. This means that the 0.1 Hz variability is more diluted when $T_{d,max}$ = 0.5-0.7 keV than for lower temperatures and, as a consequence, we observe phase lag suppression at this frequency (black vertical line in the right column of Fig. 3.5).

3.3 Observations and data analysis

We analyzed data from the *X-Ray Telescope* (XRT; Burrows et al. 2005) on board of the *Swift* satellite using 5 pointed observations collected between 2010 September 25 and 28 (MJD 55464 - 55467, first 5 observations from the beginning of the outburst). The selected observations contain between ≈ 29.6 and ≈ 58.0 ks of data obtained in the Window Timing mode configuration (WT mode), with a time resolution of 1.779 ms. Each observation contains between 1 and 27 Good Time Intervals (GTIs) of $\approx 0.8 - 2.6$ ks. The data reduction for X-ray spectral analysis was performed using HEASOFT 6.13. The observations were processed using `xrtpipeline` and the latest *Swift* CALDB files.

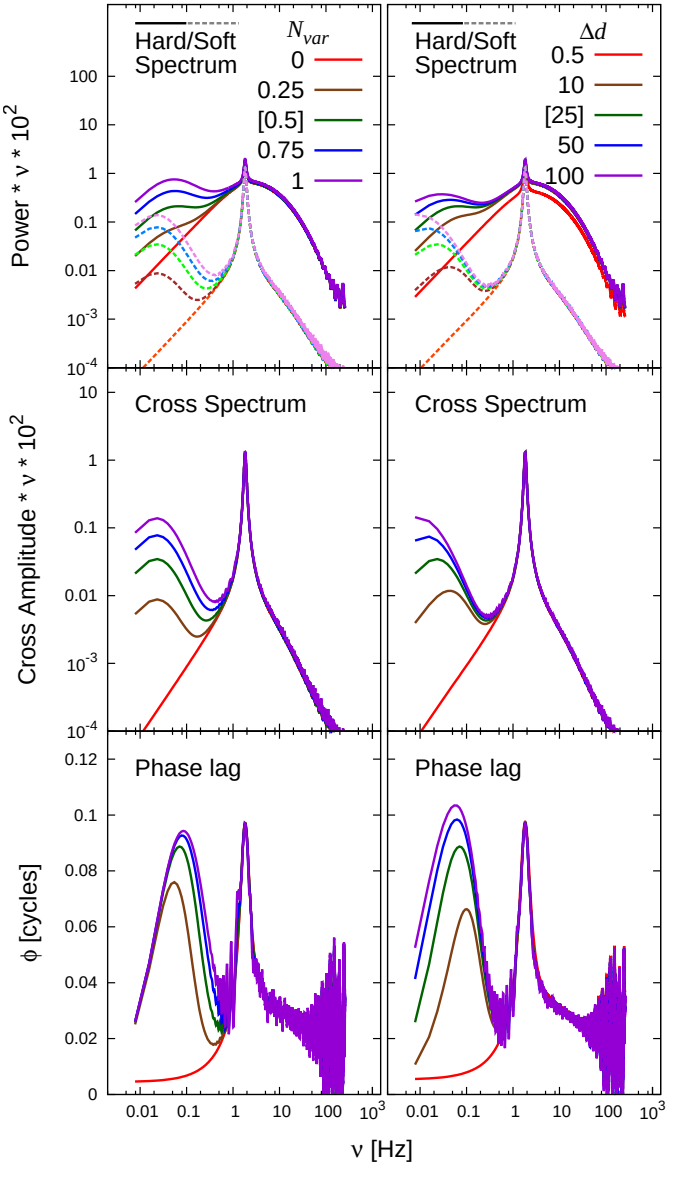

Figure 3.4: Soft (dashed line) and hard (solide line) power spectra, cross spectra, and phase lags computed varying model parameters N_{var} (left column) and Δd (right column) as indicated. Numbers in square brackets indicate the parameter value for all the other computations.

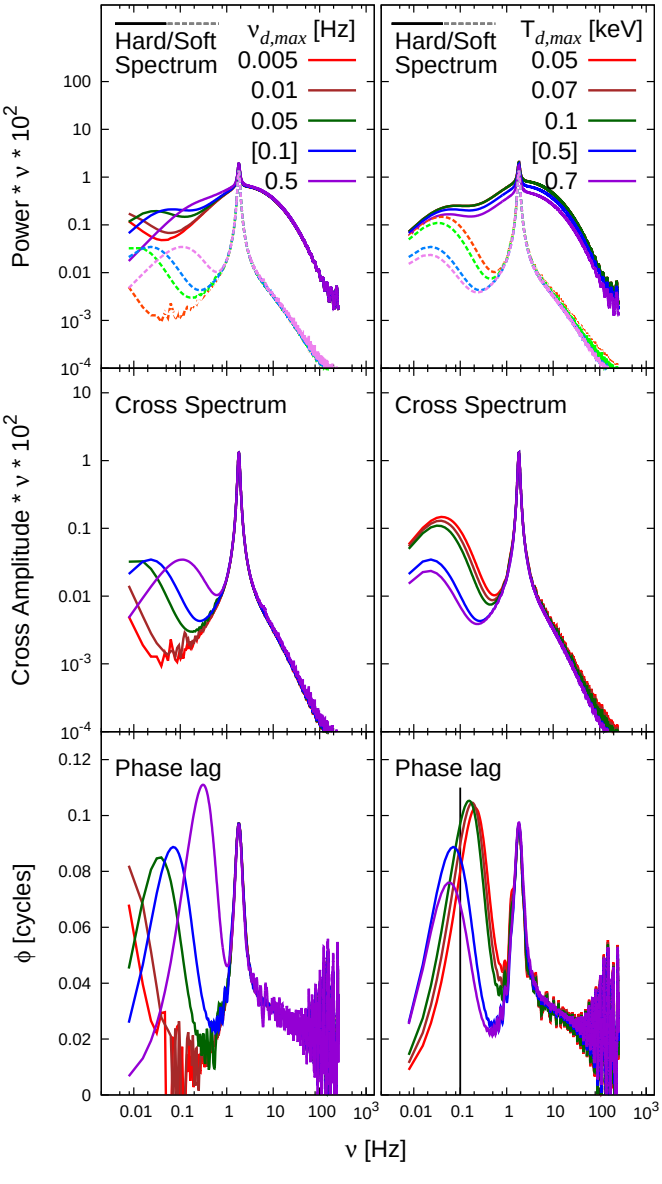

Figure 3.5: Soft (dashed line) and hard (solide line) power spectra, cross spectra, and phase lags computed varying model parameters $\nu_{d,max}$ (left column) and $T_{d,max}$ (right column) as indicated. Numbers in square brackets indicate the parameter value for all the other computations.

Source and background spectra were generated in the 0.5-10 keV range; exposure maps and response files were created as outlined in Reynolds & Miller (2013).
For every GTI we computed soft (0.5 -2.0 keV) and hard (2.0-10 keV) band light curves following the procedure described in Kalamkar et al. (2013): we determined the source and the background region on the CCD and we extracted the light curve for both regions as described in Evans et al. (2007). Each light curve is pile-up corrected. We calculated Leahy-normalized power spectra in the soft and hard band considering 233.19 s data segments in the source light curves, giving a frequency resolution of ≈ 4.3 mHz and a Nyquist frequency of ≈ 281 Hz. Using the same segments, we computed Leahy-normalized and source fractional rms normalized (RMS) cross-spectra between soft and hard band in the following way:

$$\begin{array}{lrcl} Leahy: & C_L(\nu) & = & \frac{2}{\sqrt{T_s T_h}} F_h(\nu)^* F_s(\nu) \\ RMS: & C_{RMS}(\nu) & = & \frac{\sqrt{T_s T_h}}{(T_s - N_s)(T_h - N_h)} C_L(\nu) \end{array} \tag{3.3}$$

where $F_s(\nu)$ ($F_h(\nu)$) represents the Fourier amplitude in the soft (hard) band, and T_s (T_h) and N_s (N_h) are total and background photons in the soft (hard) band respectively. Using this definition, when $F_s(\nu) = F_h(\nu) = F(\nu)$ the cross-spectrum reduces to the power spectrum with the well known Leahy and RMS normalization (Leahy et al. 1983; van der Klis 1995). For every GTI, Leahy power spectra and cross-spectra were averaged, Poisson noise subtracted estimating the noise level from the power and cross amplitude between 70 and 100 Hz (where no source variability is observed), and finally renormalized to source fractional rms normalization. For every GTI and energy band, we computed total and background count rate (T and N) from the source and the background light curve, respectively.
We fitted the energy spectra extracted from every GTI in the full energy band with the model `phabs(diskbb+comptt)` (Mitsuda et al. 1984; Titarchuk 1994). The neutral hydrogen absorption is modeled via `phabs` with Balucinska-Church & McCammon (1992) abundances and Asplund et al. (2009) cross sections. The `comptt` input seed photon temperature is fixed to the disc temperature. The energy spectral analysis and the spectral fit results are those of Kalamkar et al. (2015a). From energy spectra fitting of every GTI we computed the fraction of disc photons emitted in the soft band (x_s) and we obtained the maximum disc temperature in the disc ($T_{d,max}$).

3.4 Results

We fit our model simultaneously to the soft and hard band (0.5-2 keV and 2-10 keV, respectively) power spectrum, and the cross-spectrum between these two energy bands, for the 5 pointed *Swift* observations described in the previous section. We perform fits to the real and imaginary parts of the cross-spectrum, since this has statistically favorable properties, but plot in terms of amplitude and phase, which is more intuitive. These observations display enhanced low frequency variability in their power spectra, which Kalamkar et al. (2015b)

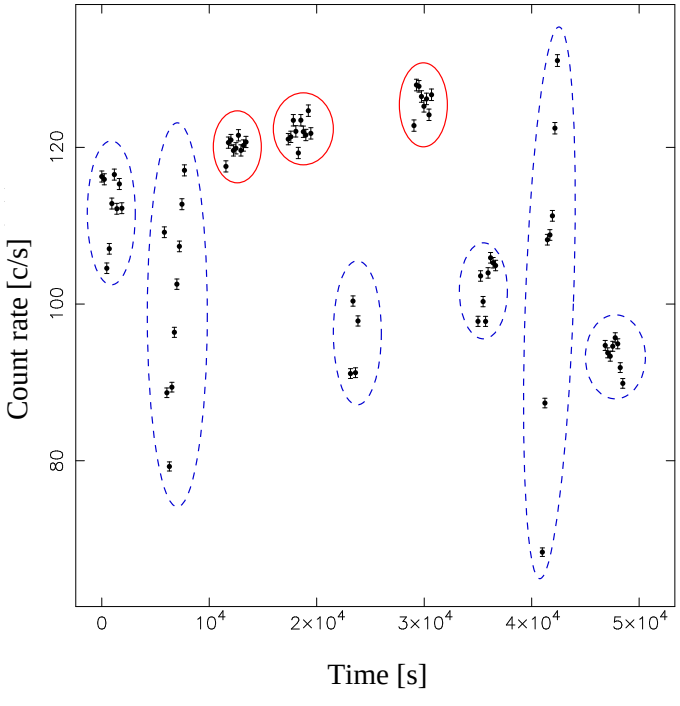

Figure 3.6: Light curve of the fourth observation from the beginning of the outburst. The light curve consists of 9 GTIs (clusters of points inside ellipses), where every point corresponds to count rate averaged over 233.19 s (the same time interval used for performing Fourier analysis). Several GTIs show clear dipping behavior (blue dashed ellipses). In our analysis we considered only no-dip time regions (red ellipses).

suggested may result from disc variability. However, MAXI J1659-152 displays absorption dips which may influence the low frequency variability properties (Kuulkers et al. 2013). In this section, we first investigate these absorption dips before using PROPFLUC to determine if the low frequency variability in these observations can originate from propagating fluctuations in the disc.

3.4.1 Dip and no-dip regions

The MAXI J1659-152 2011 outburst light curve shows two types of peculiar intensity variations: absorption dips and transition dips (Kuulkers et al. 2013). The first kind of dips, the absorption dips, is observed at day 0.3 up to day 8.2 from the beginning of the outburst (MJD

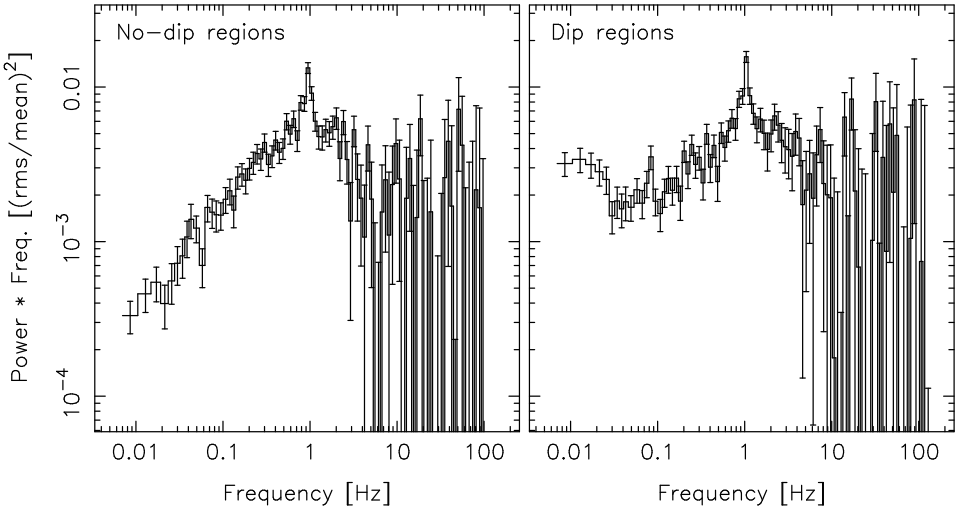

Figure 3.7: Power spectra computed on 233.19 s time intervals from the fourth observation from the beginning of the outburst. The power spectrum of GTIs showing clear dipping behavior (Dip regions) shows extra low frequency variability compared to no-dip regions.

55464), the second kind of dips, the transition (Kuulkers et al. 2013) or "flip-flop" (Kalamkar et al. 2011) dips, are observed sporadically from day 23.7, so they are not included in the time period we analyzed. The depth of the absorption dips is between about 50% and 90% the average out-of-dip interval intensity. During these dips, the source hardens, and the deeper the dip the stronger the hardening. The dips become shallower as the source intensity increases along the outburst. The dip occurrence can be explained with the presence of some absorber in the disc that periodically obscures emission along the line of sight. This period is associated with the orbital period of the binary, which allowed Kuulkers et al. (2013) to estimate with high precision the period of the system (2.414 ± 0.005 hrs) and to estimate lower and upper limit values for the disc inclination ($\approx 65^\circ$ and 80°, respectively).

The XRT observations of MAXI J1659-152 we analyzed clearly show this dipping behavior. Fig. 3.6 shows the light curve of the fourth observation from the beginning of the outburst (ObsID: 00434928003, starting at MJD 55466), each point in the plot represents the count rate in the full band (0.5 - 10.0 keV) averaged over a 233.19 s time interval (the same segment we used to compute timing analysis products). This observation consists of 9 GTIs (blue and red ellipses in the plot) and some of them are characterized by an intensity drop (blue ellipses). The light curve of the source during the dips is characterized by strong $\sim$ 100 s time scale variability, so that averaged power spectra of GTIs including dips show extra

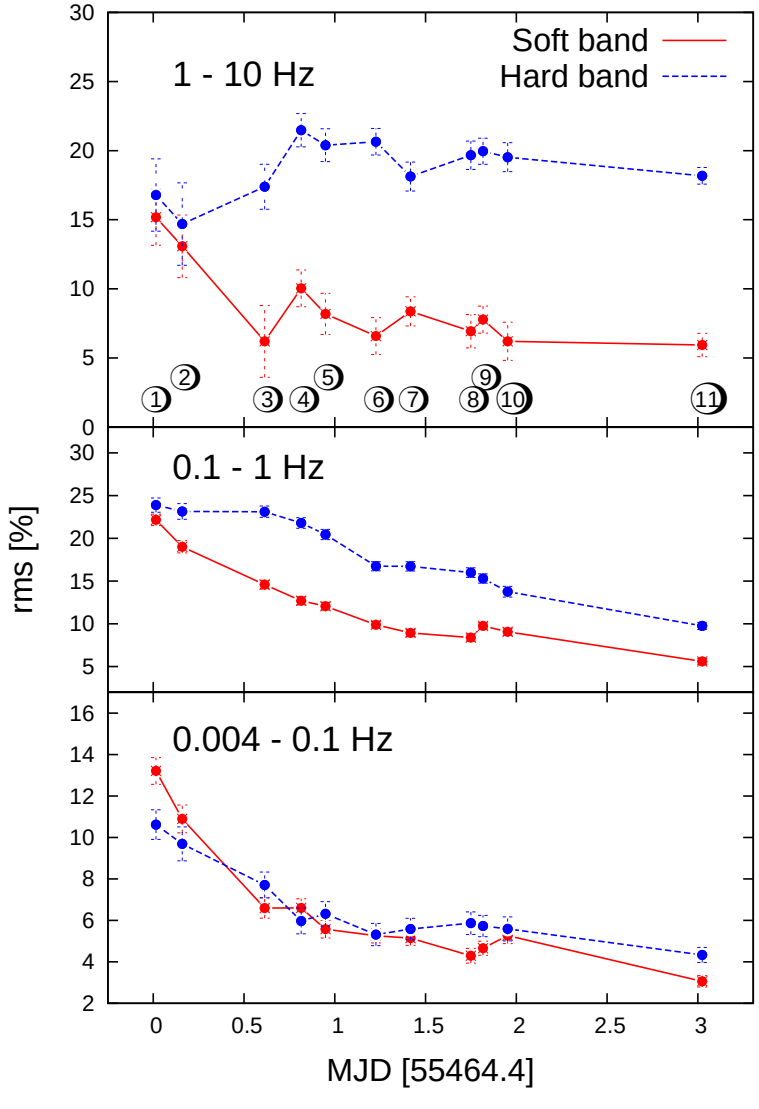

Figure 3.8: Fractional rms amplitude computed from power spectra in three different frequency bands and in two energy bands. Every point in the plots corresponds to a single $no-dip$ time interval of the source light curve.

low frequency noise between $\sim$ 0.01 and $\sim$ 0.1 Hz (see Fig. 3.7). This extra low frequency variability may be due to fluctuations in the absorbing material. In any case, it is not intrinsic to the accretion flow, since it is only present during the absorption dips. For this reason, we excluded GTIs including dips from every observation, leaving a deeper analysis on comparison between spectral and timing properties of dip and no-dip regions to future work.
The power spectra of MAXI J1659-152 in the no-dip regions are still characterized by different broad power spectral components: a low frequency component between $\sim$ 0.1 and 1 Hz and a main hump with characteristic frequency between $\sim$ 1 and 5 Hz (power spectral components referred as “break" and “hump" in Kalamkar et al. 2015b, respectively). This low frequency hump in the out-of-dip power spectrum may be driven by disc variability, with the high frequency hump generated in the flow. Before testing this hypothesis in the next section, we first consider if, instead, even the $\sim$ 0.1-1 Hz hump results from residual dipping activity that we have not been able to "weed out" with our GTI selections. If this were the case, the soft band would be more variable than the hard band (as during the dips), as changes in the column density of the absorbing material affect predominantly the soft X-rays. Fig. 3.8 shows the fractional rms amplitude computed in three different frequency bands for every single *no-dip* GTI selected in our analysis in the soft and hard band. Looking at the variability amplitude between 0.1 and 10 Hz (Fig. 3.8 top and middle panel), we notice that it is always larger in the hard band. This excludes absorption mechanisms as the origin of the “break" and “hump" component.
We notice that the 1^{st} and 2^{nd} no-dip GTIs show extra low frequency ($<$ 0.1 Hz) variability (first two points in Fig. 3.8, bottom panel). Because this variability is larger in the soft band, it is still possibly due to some residual absorption dip in the selected GTI. The presence of extra low frequency variability due to the dips can influence our test on the hypothesis of mass accretion rate fluctuations coming from the disc, for this reason any consideration regarding these two GTIs has to be handled with care.

3.4.2 A soft low-frequency QPO detected in GTI1

We report the detection of a significant QPO (4.22σ) in the soft power spectrum of the first observation (GTI1, see Fig. 3.9). We obtained the QPO characteristics by multi-Lorentzian fit (Belloni, Psaltis & van der Klis 2002): rms = 7.33 $\pm 0.80\%$, coherence $Q = 2.27 \pm 0.92$, and $\nu_{max} = 0.018 \pm 0.001$ Hz. The feature is similar to the 11 mHz QPO observed in two RXTE observations (2-60 keV) of the BH candidate H1743-322 by Altamirano & Strohmayer (2012).

3.4.3 PROPFLUC fits

We fitted logarithmically binned data points in the frequency range 0.004-70 Hz, using the same resolution for data and model. For every observation we fitted simultaneously the soft

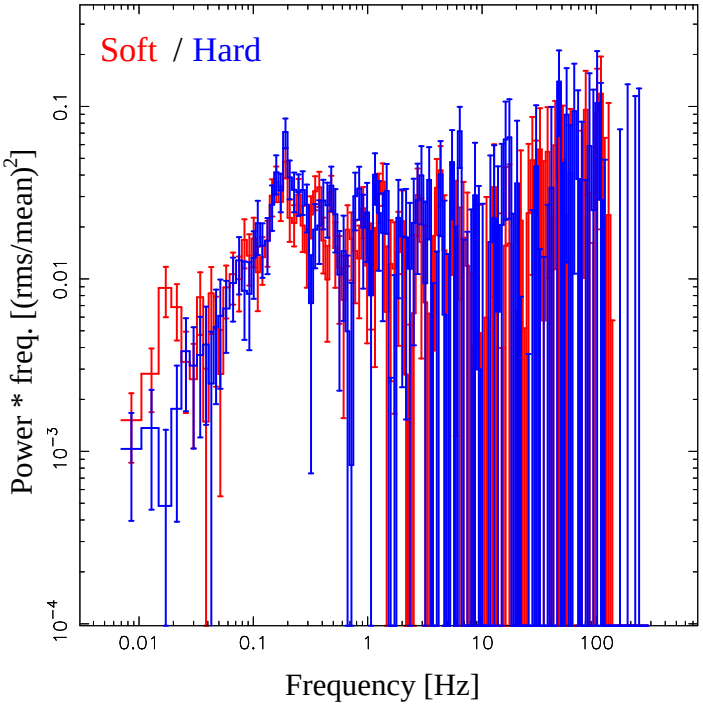

Figure 3.9: Soft (red) and hard (blue) power spectrum of the first GTI. This GTI is characterized by extra low frequency variability in the soft band, the reason of this extra variability is the presence of a soft low-frequency QPO at 0.018 Hz.

and hard spectrum, and the cross-spectrum between the two energy bands using $N_{dec} = 35$ for all the fits. A minimum of 30 rings is required to avoid interference patterns at high frequency (IK13) and we confirmed experimentally that a higher radial resolution did not produce any significant difference in χ^2_{red}. We combined the QPO with the broad band variability by addition (instead of multiplication, see IK13 and Appendix A). For all the fits we fixed the surface density profile in the hot flow (the parameters ζ, γ, and λ), the transition radius of the smoothly broken power law $r_{\rm bw}$, the emissivity in the soft and hard band (γ_s, γ_h), the mass M, and the dimensionless spin parameter of the BH a_*. In our analysis we used the *Swift* Redistribution Matrix File and Ancillary Response File closest to our data and we considered a column density of $n_H = 1.7 \times 10^{21}$ atoms/cm^2 (Kalberla et al. 2005). For fitting the low frequency hump we fixed Δd to 35 corresponding to $r_{\rm d} \approx 235$ assuming $r_{\rm o} \approx 60$ (the largest $r_{\rm o}$ value fitted in the observations we analyzed). In Sec. 3.2.2 we showed how the radial extent of the disc affects both the frequency and the integrated power of the low frequency hump, so that in general $\nu_{d,max}$ and N_{var} variations can be interpreted involving Δd changes. The choice of fixing Δd can be justified considering that larger Δd

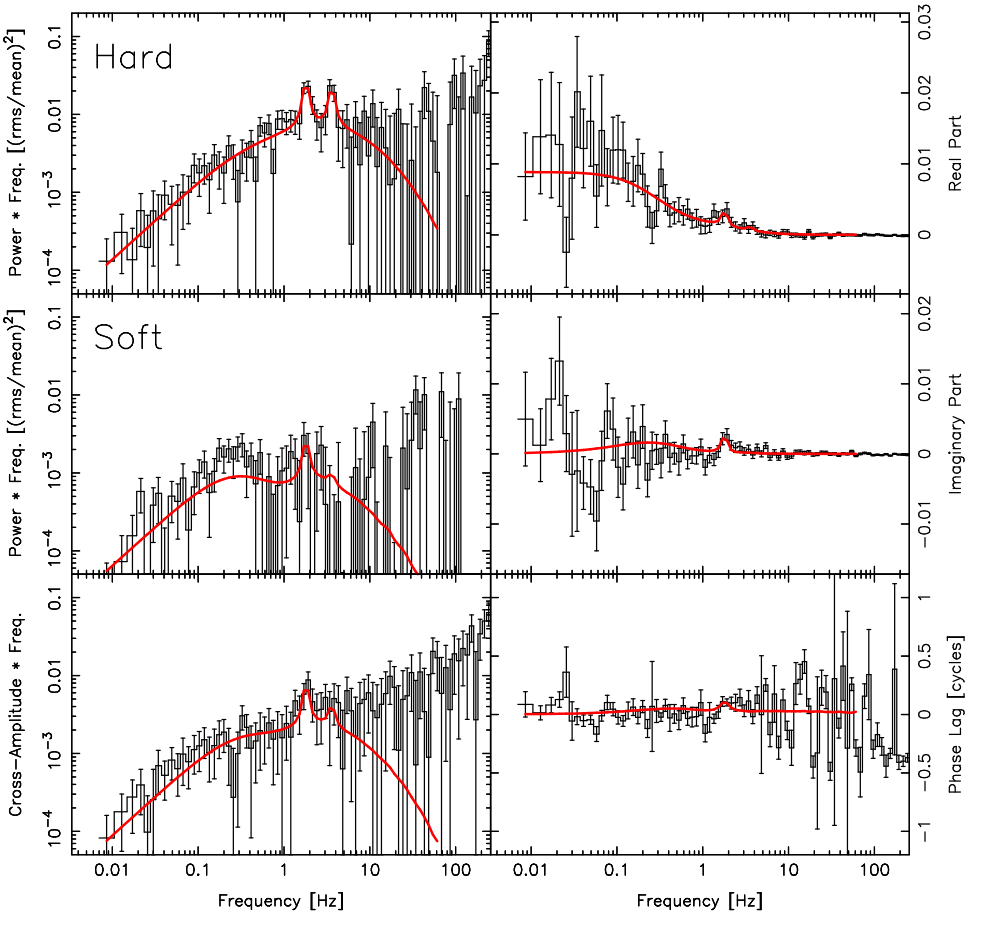

Figure 3.10: Example of joint fit of the 5^{th} observation (GTI11). Fits are performed on the hard and soft power spectrum (1^{st} column), and on the real and imaginary part of the cross-spectrum (2^{nd} column). The 3^{rd} column shows the cross-spectrum represented in terms of amplitude and the phase lag, rather than real and imaginary parts.

values would produce a broader low frequency component than the one observed in the data and $\nu_{d,max}$ values closer to or even larger than the viscous frequency in the hot flow at the truncation radius $\nu_{v,flow}(r_o)$. This last configuration is not consistent with the double hump model assumptions which: 1) imply a discontinuity in the physical properties of the entire accreting region at the truncation radius (so a "jump" of the viscous frequency at r_o), and 2) imply that the characteristic time scale of the variability originating in the hot flow is shorter than in the disc.

We computed the hardness ratio HR dividing hard by soft background subtracted photon counts, and the disc fraction in the soft band x_s from spectral fitting. The free fit parameters

are the surface density normalization constant Σ_0, the fractional variability in the hot flow F_{var}, the truncation radius $r_{\rm o}$, the rms and phase lag of the main QPO, second, and eventually third and sub-harmonic (σ_{qpo}, σ_{qpo2}, σ_{qpo3}, σ_{sub} and ϕ_{qpo}, ϕ_{qpo2}, ϕ_{qpo3}, ϕ_{sub} respectively) in both soft and hard band, the variability in the disc as a fraction of the hot flow variability N_{var}, and the maximum viscous frequency in the disc $\nu_{d,max}$.
Fig. 3.10 shows the simultaneous PROPFLUC fit of the soft and hard power, and the cross-spectrum of the fifth observation (in particular, we plot the hard and soft power spectrum, the real and imaginary part of the cross-spectrum, the cross-spectrum, and the phase lag). The best fit parameters are reported in Tab. 3.1, and Fig. 3.11 shows the evolution of the free model parameters with time (black points). For simplicity, we labeled with integers from 1 to 11 the no-dip GTIs we filtered from the 5 selected pointed *Swift* observations (Fig. 3.11 panel a, c, and e). From GTI 1 to 11, Σ_0 increases from ≈ 2.8 to ≈ 4.2. This increasing trend is not continuous, there are 3 dips (values smaller than the contiguous observations) at GTI 2, 4 and 7, and 3 local peaks at GTI 3, 5, and 8. The truncation radius $r_{\rm o}$ shows a clear smooth decreasing trend from ≈ 60 to 20, indicating an average truncation radius recession speed of about 0.6 $R_{\rm g}$/h (≈ 9 km/h). The fractional variability F_{var} shows a smooth decreasing trend between GTI 1 and 11 (from $\approx 35\%$ to 28%) interrupted by values smaller than average ($\approx$ 17-26%) between GTI 5 and 8. Panels d and e in Fig. 3.11 show the evolution of the model parameters related to the low frequency hump, empty symbols represent upper limits (3σ confidence level). N_{var} varies around ≈ 0.2 and 0.5 in GTI 1-4 and 9-11, respectively. Between GTI 5 and 8, N_{var} is characterized by larger values ($\approx$ 0.8-1.3), in particular it shows an increasing trend between GTI 6 and 8. The maximum viscous frequency in the disc $\nu_{d,max}$ shows an evolution similar to N_{var} with a general increasing trend (from ≈ 0.07 to 1.23 Hz) and higher values than average between GTI 5 and 8.

3.5 Discussion

3.5.1 Double hump and single hump power spectrum

In this study, we presented a new version of the PROPFLUC model that can produce a two-hump power spectrum, where the main hump originates because of mass accretion rate fluctuations propagating through the hot flow (as described in ID12, IK13, Chapter 2) and an additional low frequency hump is produced by fluctuations propagating from the thermal varying disc into the hot flow. Assuming a photon emission mechanism for the hot flow and the disc, we calculated power spectra and cross-spectra between two energy bands (Sec. 3.2). We used this model to study 5 observations of the BHB MAXI J1659-152 during its 2010 outburst using *Swift* data. We measured the spectral parameters required as input by the model by spectral fits, and we fitted soft and hard band power spectra, and cross-spectra simultaneously with both the single and the double hump PROPFLUC version. In a single hump power spectrum, mass accretion rate fluctuations generated and propagating in the hot flow are the only variability source. In a double hump power spectrum, variability is generated

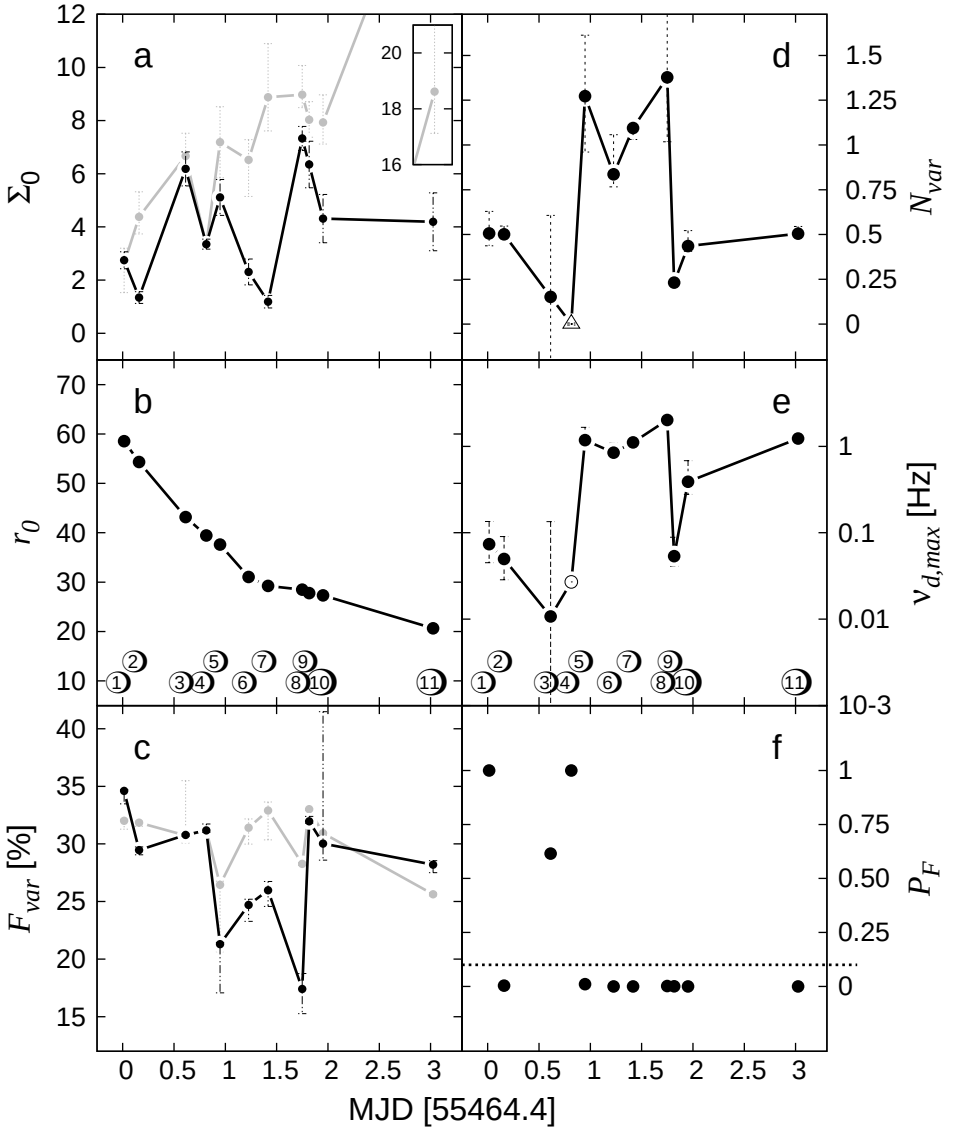

Figure 3.11: PROPFLUC best fit parameters versus time (black points). All the points were plotted with 1σ error bars. Grey points correspond to single hump best fit parameters (fit results excluding the disc propagating region). The filtered GTIs are indicated with integers from 1 to 11 (symbols in panels a, c, and e). Panel f indicates the F probability related to a single hump fit.

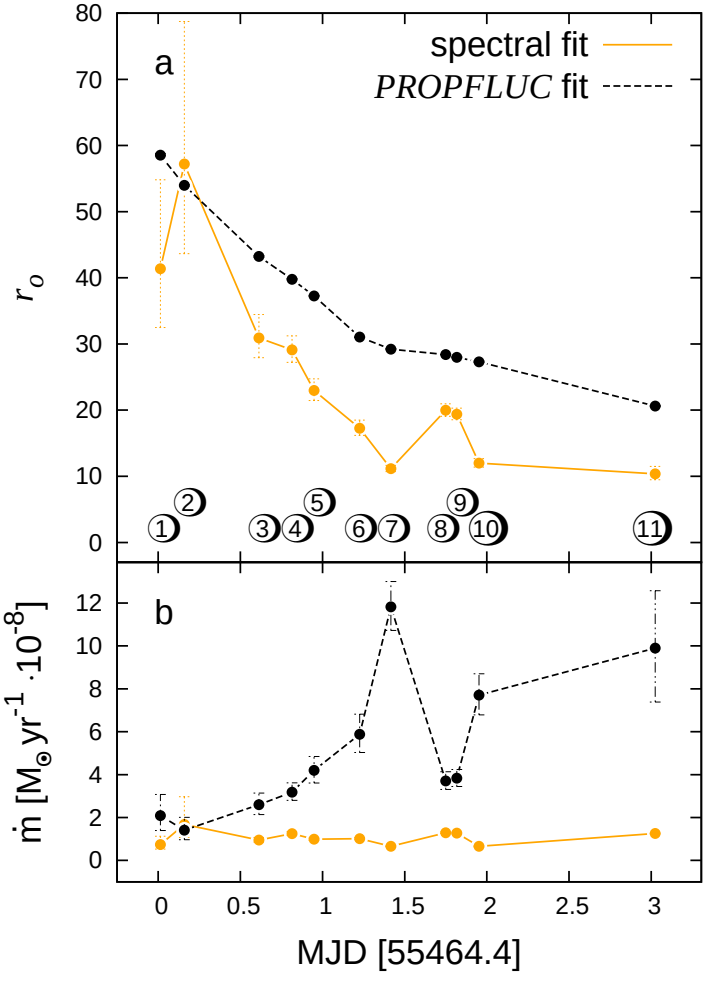

Figure 3.12: Truncation radius r_o (a) and mass accretion rate (b) computed using timing (black dashed line) and spectral fit (yellow solid line) results.

both in the hot flow and in the disc, so that the way the total variability power is distributed between low frequency and main hump depends both on the hot flow and disc characteristics. If a low frequency component is present in the power spectrum, we expect the peak of the main hump in the two-hump model to be shifted to higher frequency relative to the single hump model (i.e., when the low frequency component is not taken into account). The grey points in Fig. 3.11(a) and (c) are the best fit parameter values obtained using a single hump power spectrum. We find that both Σ_0 and F_{var} from single hump fit are different compared to the double hump fit results, in particular the single hump Σ_0 values are larger for all the

GTIs.
Fig. 3.11(f) shows the F probability for every pair of fits, i.e., the probability that the χ^2 improvement when using the double hump model is due to statistical fluctuations. Low probability indicates that the double hump model gives a better fit than the single hump model. P_F exceeds $\approx 1\%$ only in 3 cases (GTI 1, 3, and 4), for all the other GTIs the use of the additional hump originating in the disc is statistically justified.
So, the double hump model fits significantly better than the single hump one, but the fits are not formally acceptable (see Tab. 3.1 at reduced χ^2 values of $\approx$ 1.3 - 1.5). Given that in this first-ever attempt to quantitatively model power and cross-spectra jointly our model reproduces most of the overall characteristics of the data, it seems useful to discuss the evolution of the source in terms of the model physical parameters, but we note that any interpretation of the parameter evolution has to be handled with care.

3.5.2 Evolution of the physical parameters

Contrary to the case with previous applications of the model (ID12, Chapter 2), the fractional variability shows in general a decreasing trend.
For a fixed ring, Σ_0 is proportional to the surface density profile divided by mass accretion rate (RIK14), so that, assuming a constant surface density per ring, Σ_0 can trace variations in mass accretion rate. Even if Σ_0 shows a general increasing trend from GTI 1 to 11, the several dips and peaks in its trend suggest a variable accretion regime, in particular between GTI 7 and 10.
We did not detect a significant lag associated with the low frequency component. This may seem surprising if the process generating the broad band noise is mass accretion rate fluctuations propagating through the accreting flow. In a propagating fluctuations model the amplitude of the lag between two energy bands depends on the radial extension of the propagating region, on the difference between the emissivity profiles, and on the propagation time scale of the fluctuations (Nowak et al. 1999b; Kotov et al. 2001; Arevalo & Uttley 2006). In our model, the propagation time is set by the local viscous time scale, that is equal to the characteristic time scale of the variability produced in every ring. So, the main PROPFLUC parameters affecting the amplitude of the phase lag are γ_s and γ_h (fixed in our fit), and $T_{d,max}$, x_s, and HR (estimated by spectral fitting and measuring the photon counts in the soft and hard bands, see Fig. 3.13). In Sec. 3.2.2 we showed that for x_s = 0.9 and HR = 1, PROPFLUC predicts $\approx$ 0.1 cycle phase lags in the low frequency hump. In all our observations $x_s < 0.63$ and $HR < 0.7$, leading to predicted phase lags smaller than 0.1 cycles. Such lags are not detectable in our data. So, the absence of phase lags in the low frequency hump does not exclude the hypothesis of propagating mass accretion rate fluctuations and it is consistent with PROPFLUC predictions for this case. However, because of this lack of additional information, we can not completely remove the degeneracy between the model parameters, especially those related to the radial extension of low frequency hump and affecting the lag profile (Δd,

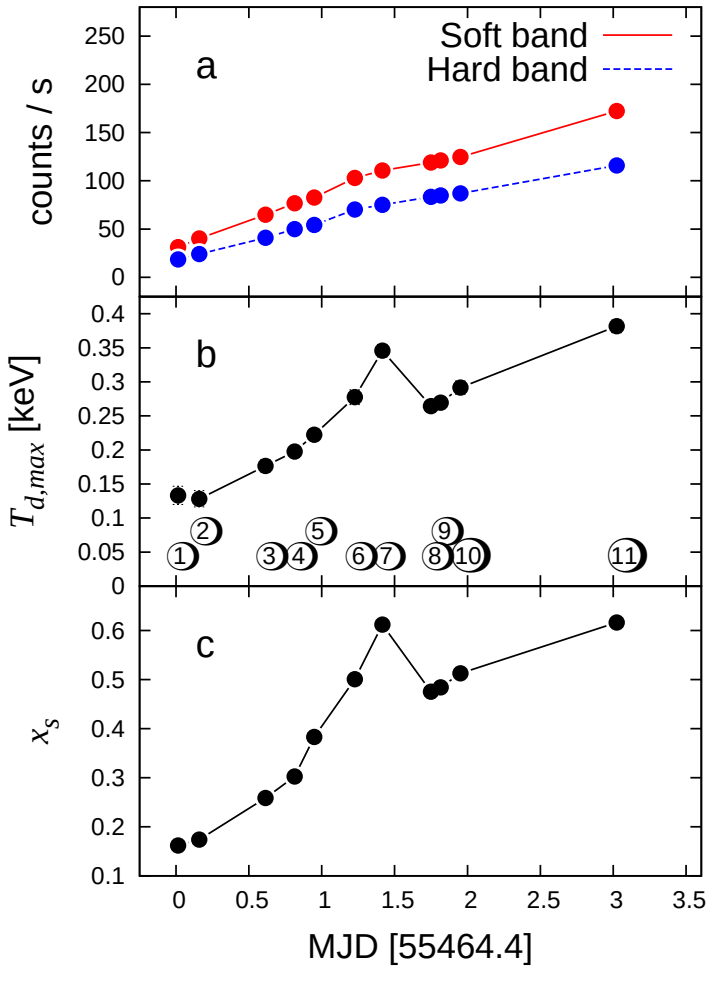

Figure 3.13: Spectral properties of the source for all the analyzed observations. a) Count rate in the soft and hard energy band; b) Maximum disc temperature in the disc; c) Fraction of total photons detected in the soft band.

$N_{var}, \nu_{d,max}$).

3.5.3 Mass accretion rate from spectral and timing analysis

It is possible to compute two independent estimates of the truncation radius r_o from timing and spectral analysis, respectively. In the PROPFLUC fits r_o mainly depends on the

QPO frequency; we can also compute $r_{\rm o}$ from spectral fits using the DISKBB model normalization , the distance d, and the inclination of the accreting disc to the line of sight θ ($norm = \left(\frac{r_o/[km]}{d/[10kpc]}\right)^2 cos(\theta)$). Fig. 3.12($a$) shows the truncation radius computed using both PROPFLUC (black dashed line) and spectral fit (yellow solid line). For computing the last one we used d = 8.6 $\pm$ 3.7 kpc and θ = 72.5° $\pm$ 7.5° (Kuulkers et al. 2013). The absolute values shown in the plot have to be handled with care: the QPO frequency depends not only on $r_{\rm o}$, but also on the hot flow structure ($r_{\rm bw}$, λ, ζ, κ), on the hot flow inner boundary $r_{\rm i}$, on the spin, and on the mass of the BH; the estimation of $r_{\rm o}$ via the DISKBB normalization needs to be corrected because of possible deviation of the emitting region from pure blackbody behavior (Merloni, Fabian, & Ross 2000 and 2001), and general relativistic effects (e.g. Ebisawa et al. 1994). However, $r_{\rm o}$ values obtained in these two ways are the same within a factor of 2, and, in general, show the same decreasing trend. The main difference between the two is that $r_{\rm o}$ from PROPFLUC fit is characterized by a smooth decreasing trend, while $r_{\rm o}$ from spectral fit shows a more irregular behavior with a local peak in GTI 8-9.
From the truncation radius and the maximum temperature in the disc, it is possible to compute the mass accretion rate $\dot{M}$ (Frank, King, & Raine 2002):

$$\dot{M} = \frac{8\pi\sigma}{3GM_{BH}} r_o^3 T_{max}^4 \tag{3.4}$$

3 Similarly to Fig. 3.12(a), Fig. 3.12(b) shows $\dot{M}$ computed from the PROPFLUC $r_{\rm o}$ (hereafter $\dot{M}_{prop}$) and the spectral fit $r_{\rm o}$ measurement (hereafter $\dot{M}_{spec}$). $\dot{M}_{spec}$ is almost constant while $\dot{M}_{prop}$ shows an increasing trend with a peak at GTI 7 followed by a dip in GTIs 8-9. This difference is because $T_{d,max}$ and DISKBB normalization variations compensate each other, while the decreasing $r_{\rm o}$ trend obtained from timing analysis is smooth, so that the resulting $\dot{M}_{prop}$ varies similarly to $T_{d,max}$ (Fig. 3.13b). Looking at luminosity variations (Fig. 3.13a), $\dot{M}_{prop}$ is in agreement with the increasing trend in count rate. It is also interesting to compare the jump followed by the dip in $\dot{M}_{prop}$ between GTIs 6 and 10 with similar features over the same GTIs in Σ_0, F_{var}, N_{var}, and $\nu_{d,max}$ (Fig. 3.11; we note that these are PROPFLUC parameters independent from spectral fit parameters). The peak and the following dip in mass accretion rate rate at GTI 7 and 8-9 respectively are consistent with Σ_0 variations: higher $\dot{M}_{prop}$ values correspond to lower Σ_0 values, and vice versa. The relation between $\dot{M}_{prop}$ and F_{var}, N_{var}, and $\nu_{d,max}$ is more difficult to interpret. We may speculate that the jump in $\dot{M}$ at GTI 7 (triggered by some instability) may have stirred up extra variability in the disc and in the flow (increasing N_{var} and F_{var}) and will have increased the viscous frequency in the disc (since $\nu_v \propto \dot{M}$ though mass conservation). The dip in $\dot{M}_{prop}$ (GTI 8) then follows as the supply of material is depleted, leading to the corresponding dips seen in F_{var} (GTI 8), and in N_{var} and $\nu_{d,max}$ with a GTI of delay (the material closer to the BH is depleted faster). Because of the jump in $\dot{M}$ we would also expect some variation in the average decreasing rate of $r_{\rm o}$. Indeed, in a truncated disc geometry the radial dimension of the hot flow depends on mass accretion rate, and when mass accretion rate increases (rising part of the outburst), $r_{\rm o}$ moves in. Fig. 3.14 shows the rate of $r_{\rm o}$ decrease for all the observations considered in our

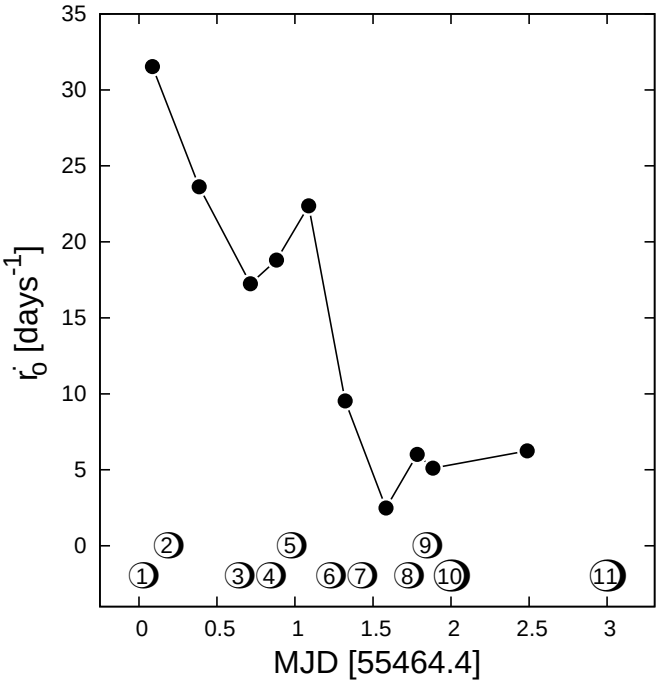

Figure 3.14: The black points represent the average r_o decreasing rate between couples of GTIs (indicated with symbols in the same way of previous Figs)

analysis. Between GTI 5 and 6 r_o decreases faster than average, while between GTI 7 and 8 it decreases slower than average. This behavior is consistent with the mass accretion rate variations described above.

3.5.4 The absorption dips

In our study of MAXI J1659-152 we excluded time intervals characterized by absorption dips (see Sec. 3.4.1). Power spectra computed including dip-regions show strong low frequency noise ($\sim$ 0.01 Hz). This additional noise component was identified as “lfn" in the Kalamkar et al. (2015b) timing analysis of the source. In their study, it was proposed that the characteristics of the < 0.1 Hz “lfn" component during the outburst could be explained with variability arising in the disc and propagating into the hot flow. Here, we exclude this possibility for the observations we analyzed mainly because the “lfn" component is strongly coupled with the periodic absorption dips in the light curve (Sec. 3.4.1). Contrary to the case of the “lfn”, the rms amplitude in the 0.1 - 10 Hz frequency band (Fig. 3.8, top and middle panel) is always larger in the hard band. For this reason the components identified as “break" and “hump" in Kalamkar et al. (2015b) (with characteristic frequency between $\sim$ 0.1 and $\sim$

5 Hz in our observation sample), can not have been produced by varying absorption. In our fit with PROPFLUC, the “break" and “hump" components are associated to the disc and the hot flow, respectively.

3.6 Conclusions

We applied the double hump model PROPFLUC to investigate the HIMS of MAXI J1659-152 using *Swift* data. In the model, low frequency broad band components are interpreted as the result of mass accretion rate fluctuations arising in the disc and propagating towards the BH through the hot precessing flow. This double hump model was statistically preferred to a single hump model for most of the GTIs analyzed. In our analysis we detected only small phase lag associated with the low frequency variability, however model predictions are consistent with the data. Using both spectral and timing analysis we estimated recessing trend in truncation radius, and from that we inferred the mass accretion rate. Considering the truncation radius estimate from the PROPFLUC fit and the maximum temperature in the disc (spectral fit parameter), we found a peak in the average increasing mass accretion rate trend that matches the variability properties of the accreting system (the amount of variability generated and the viscous frequency in the disc and in the flow). Considering the truncation radius estimate from spectral fit, would have lead to an almost constant mass accretion rate, in contrast to observations (the total counts increase almost linearly in our observation sample). Our analysis constitutes the first joint fitting of compact object cross-spectra and power spectra with a single self-consistent physical model.

Table 3.1: Best fit PROPFLUC parameters (double hump). Errors correspond to 1σ confidence level. The subscripts s and h correspond to soft and hard band respectively. The symbol $\sim$ means that the parameter is fixed at the value in column 2 for all the GTIs, the symbol $-$ means that the component did not significantly improve the χ^2 and was omitted, and the symbol $\uparrow$ indicates 3σ upper limit (see GTI4). The last row shows the F probability relative to a single hump fit. $T_{d,max}$ and x_s are fixed model parameters computed from previous energy spectral analysis.

MJD	55464.4093317 [1]	55464.5541349 [2]	55465.0086948 [3]	55465.2095189 [4]	55465.3433757 [5]	55465.6217809 [6]
Σ_0	$2.75^{+0.32}_{-0.19}$	$1.34^{+0.22}_{-0.25}$	$6.18^{+0.64}_{-0.35}$	$3.35^{+0.19}_{-0.12}$	$5.11^{+0.67}_{-0.55}$	$2.31^{+0.49}_{-0.75}$
$F_{var}[\%]$	$34.60^{+0.11}_{-1.13}$	$29.46^{+0.28}_{-0.41}$	$30.78^{+0.08}_{-0.11}$	$31.17^{+0.56}_{-0.16}$	$21.30^{+0.15}_{-4.23}$	$24.71^{+0.49}_{-1.43}$
ζ	0	$\sim$	$\sim$	$\sim$	$\sim$	$\sim$
λ	0.9	$\sim$	$\sim$	$\sim$	$\sim$	$\sim$
κ	3.0	$\sim$	$\sim$	$\sim$	$\sim$	$\sim$
r_i	4.5	$\sim$	$\sim$	$\sim$	$\sim$	$\sim$
r_{bw}	5.0	$\sim$	$\sim$	$\sim$	$\sim$	$\sim$
r_o	$58.55^{+0.26}_{-0.17}$	$54.32^{+0.15}_{-0.15}$	$43.18^{+0.17}_{-0.09}$	$39.45^{+0.09}_{-0.09}$	$37.60^{+0.06}_{-0.05}$	$31.05^{+0.07}_{-0.05}$
N_{var}	$0.51^{+0.12}_{-0.07}$	$0.50^{+0.05}_{-0.02}$	$0.15^{+0.46}_{-0.46}$	$0.0002\uparrow$	$1.27^{+0.34}_{-0.31}$	$0.84^{+0.22}_{-0.07}$
Δd	35.0	$\sim$	$\sim$	$\sim$	$\sim$	$\sim$
$\nu_{d,max}$	$0.074^{+0.061}_{-0.029}$	$0.050^{+0.041}_{-0.021}$	$0.011^{+0.124}_{-0.124}$	0.027	$1.182^{+0.477}_{-0.230}$	$0.844^{+0.245}_{-0.060}$
$T_{d,max}$ [keV]	0.13	0.13	0.18	0.20	0.22	0.28
Q	$1.92^{+0.35}_{-0.11}$	$2.67^{+0.14}_{-0.10}$	$3.79^{+0.47}_{-0.27}$	$2.91^{+0.37}_{-0.15}$	$4.13^{+0.24}_{-0.11}$	$2.97^{+0.25}_{-0.11}$
Q_{sub}	$1.99^{+1.63}_{-1.15}$	$2.40^{+0.76}_{-0.45}$	$1.09^{+0.78}_{-0.52}$	$0.50^{+0.09}_{-0.04}$	$0.21^{+0.08}_{-0.06}$	$0.58^{+0.35}_{-0.12}$
$\sigma_{QPO,h}[\%]$	$16.18^{+0.09}_{-0.53}$	$16.57^{+0.10}_{-0.63}$	$13.89^{+0.14}_{-0.21}$	$15.74^{+0.11}_{-0.22}$	$13.21^{+0.08}_{-0.19}$	$12.58^{+0.08}_{-0.17}$
$\sigma_{QPO2,h}[\%]$	$5.19^{+1.02}_{-1.46}$	$8.03^{+0.21}_{-0.66}$	$6.83^{+1.41}_{-1.09}$	$6.21^{+1.10}_{-1.30}$	$7.14^{+1.09}_{-0.82}$	$6.27^{+0.98}_{-1.34}$
$\sigma_{QPO3,h}[\%]$	-	$7.51^{+0.37}_{-1.18}$	$5.68^{+1.04}_{-1.36}$	$9.55^{+0.17}_{-0.77}$	$6.51^{+1.05}_{-1.16}$	$7.52^{+1.30}_{-0.69}$
$\sigma_{QPO_{sub},h}[\%]$	$2.98^{+2.55}_{-1.67}$	$5.92^{+0.44}_{-0.67}$	$2.90^{+2.97}_{-2.15}$	$7.72^{+1.81}_{-0.85}$	$4.04^{+2.07}_{-1.90}$	$3.63^{+1.00}_{-1.63}$
$\sigma_{QPO,s}[\%]$	$13.88^{+0.12}_{-0.99}$	$12.01^{+0.21}_{-0.23}$	$6.98^{+0.41}_{-0.20}$	$4.44^{+0.22}_{-0.39}$	$5.10^{+0.18}_{-0.17}$	$5.22^{+0.12}_{-0.14}$
$\sigma_{QPO2,s}[\%]$	$10.17^{+0.29}_{-0.52}$	$7.35^{+0.87}_{-1.15}$	$4.58^{+0.38}_{-0.85}$	$3.27^{+0.28}_{-1.19}$	$2.03^{+0.30}_{-1.17}$	$1.06^{+0.14}_{-0.82}$
$\sigma_{QPO3,s}[\%]$	-	$7.55^{+1.26}_{-1.41}$	$3.61^{+0.38}_{-1.12}$	$2.18^{+0.33}_{-1.14}$	$1.91^{+0.27}_{-1.10}$	$3.25^{+0.17}_{-0.48}$
$\sigma_{QPO_{sub},s}[\%]$	$7.80^{+0.17}_{-0.94}$	$6.70^{+0.80}_{-1.13}$	$5.67^{+0.70}_{-1.02}$	$9.69^{+0.05}_{-0.26}$	$9.10^{+0.04}_{-0.47}$	$5.61^{+0.38}_{-0.59}$
$\phi_{QPO}[cycles]$	$0.01^{+0.00}_{-0.00}$	$0.01^{+0.00}_{-0.00}$	$0.02^{+0.01}_{-0.01}$	$0.01^{+0.02}_{-0.01}$	$0.12^{+0.01}_{-0.01}$	$0.11^{+0.00}_{-0.00}$
$\phi_{QPO2}[cycles]$	$-0.01^{+0.05}_{-0.05}$	$0.02^{+0.03}_{-0.02}$	$-0.00^{+0.05}_{-0.05}$	$-0.04^{+0.06}_{-0.08}$	$-0.08^{+0.09}_{-0.14}$	$0.05^{+0.32}_{-0.35}$
$\phi_{QPO3}[cycles]$	-	$-0.06^{+0.03}_{-0.03}$	$0.03^{+0.07}_{-0.07}$	$0.10^{+0.15}_{-0.08}$	$0.12^{+0.18}_{-0.23}$	$0.07^{+0.05}_{-0.06}$
$\phi_{QPO_{sub}}[cycles]$	$0.05^{+0.15}_{-0.07}$	$0.05^{+0.04}_{-0.02}$	$-0.11^{+0.11}_{-0.25}$	$0.06^{+0.03}_{-0.01}$	$-0.10^{+0.20}_{-0.17}$	$-0.12^{+0.17}_{-0.13}$
γ_s	3.0	$\sim$	$\sim$	$\sim$	$\sim$	$\sim$
γ_h	4.5	$\sim$	$\sim$	$\sim$	$\sim$	$\sim$
x_s	0.16	0.17	0.26	0.35	0.38	0.50
χ^2/dof	366.22/380	412.20/377	407.12/377	665.23/377	400.22/377	374.50/377
$P_f[\%]$	100.00	0.40	61.54	100.00	1.04	< 0.1

Table 3.1: Continued.

MJD	55465.8117549 [7]	55466.1446146 [8]	55466.2118039 [9]	55466.34714 [10]	55467.4190101 [11]
Σ_0	$1.19^{+0.24}_{-0.27}$	$7.33^{+0.45}_{-0.28}$	$6.35^{+0.88}_{-0.52}$	$4.31^{+0.91}_{-0.53}$	$4.19^{+1.09}_{-0.77}$
$F_{var}[\%]$	$25.97^{+0.76}_{-1.40}$	$17.41^{+1.34}_{-2.14}$	$31.96^{+0.43}_{-0.16}$	$30.03^{+11.45}_{-1.44}$	$28.20^{+0.35}_{-0.70}$
ζ	0	$\sim$	$\sim$	$\sim$	$\sim$
λ	0.9	$\sim$	$\sim$	$\sim$	$\sim$
κ	3.0	$\sim$	$\sim$	$\sim$	$\sim$
r_i	4.5	$\sim$	$\sim$	$\sim$	$\sim$
r_{bw}	5.0	$\sim$	$\sim$	$\sim$	$\sim$
r_o	$29.23^{+0.07}_{-0.08}$	$28.47^{+0.04}_{-0.04}$	$27.78^{+0.12}_{-0.07}$	$27.32^{+0.12}_{-0.12}$	$20.65^{+0.04}_{-0.04}$
N_{var}	$1.09^{+0.01}_{-0.06}$	$1.38^{+0.37}_{-0.36}$	$0.23^{+0.01}_{-0.01}$	$0.44^{+0.09}_{-0.03}$	$0.50^{+0.04}_{-0.02}$
Δd	35.0	$\sim$	$\sim$	$\sim$	$\sim$
$\nu_{v,max}$	$1.113^{+0.052}_{-0.070}$	$2.017^{+0.248}_{-0.217}$	$0.054^{+0.035}_{-0.012}$	$0.389^{+0.295}_{-0.111}$	$1.232^{+0.248}_{-0.109}$
$T_{d,max}$ [keV]	0.35	0.26	0.27	0.29	0.38
Q	$5.08^{+0.87}_{-0.42}$	$10.30^{+2.70}_{-1.49}$	$6.53^{+2.44}_{-1.31}$	$6.81^{+1.39}_{-0.67}$	$9.83^{+4.49}_{-2.57}$
Q_{sub}	$6.77^{+3.39}_{-3.39}$	$0.16^{+0.07}_{-0.04}$	$0.63^{+0.08}_{-0.05}$	$0.59^{+0.38}_{-0.15}$	$30.73^{+0.01}_{-0.01}$
$\sigma_{QPO,h}[\%]$	$10.51^{+0.16}_{-0.18}$	$8.61^{+0.88}_{-0.37}$	$8.89^{+0.94}_{-0.25}$	$9.68^{+1.02}_{-0.25}$	$7.25^{+0.39}_{-0.14}$
$\sigma_{QPO2,h}[\%]$	$6.77^{+0.60}_{-0.49}$	$2.80^{+0.54}_{-2.43}$	$4.04^{+0.73}_{-2.07}$	$4.97^{+1.24}_{-1.60}$	$6.52^{+0.44}_{-0.31}$
$\sigma_{QPO3,h}[\%]$	$4.39^{+0.57}_{-1.18}$	-	-	$3.02^{+1.82}_{-1.82}$	-
$\sigma_{QPO_{sub},h}[\%]$	$3.45^{+0.58}_{-1.23}$	$13.19^{+0.18}_{-2.90}$	$6.09^{+2.00}_{-1.13}$	$2.99^{+0.25}_{-1.55}$	$2.49^{+0.20}_{-0.63}$
$\sigma_{QPO,s}[\%]$	$4.17^{+0.09}_{-0.17}$	$3.23^{+0.07}_{-0.18}$	$2.85^{+0.10}_{-0.35}$	$3.32^{+0.56}_{-0.31}$	$2.23^{+0.06}_{-0.21}$
$\sigma_{QPO2,s}[\%]$	$2.51^{+0.12}_{-0.72}$	-	$0.75^{+0.15}_{-0.15}$	$1.66^{+0.22}_{-0.22}$	$0.75^{+0.08}_{-0.53}$
$\sigma_{QPO3,s}[\%]$	$3.61^{+0.17}_{-0.73}$	-	-	-	-
$\sigma_{QPO_{sub},s}[\%]$	$2.17^{+0.36}_{-0.64}$	$6.36^{+0.54}_{-1.12}$	$7.93^{+0.57}_{-0.22}$	$7.71^{+1.31}_{-0.38}$	$0.33^{+0.04}_{-0.04}$
$\phi_{QPO}[cycles]$	$0.08^{+0.01}_{-0.01}$	$0.16^{+0.01}_{-0.01}$	$0.14^{+0.01}_{-0.02}$	$0.15^{+0.01}_{-0.01}$	$0.12^{+0.01}_{-0.02}$
$\phi_{QPO2}[cycles]$	$-0.02^{+0.05}_{-0.05}$	-	$-0.09^{+0.01}_{-0.01}$	$-0.01^{+0.11}_{-0.11}$	$0.05^{+0.26}_{-0.13}$
$\phi_{QPO3}[cycles]$	$0.07^{+0.07}_{-0.05}$	-	-	-	-
$\phi_{QPO_{sub}}[cycles]$	$-0.07^{+0.07}_{-0.07}$	$0.05^{+0.09}_{-0.01}$	$-0.01^{+0.04}_{-0.04}$	$0.04^{+0.15}_{-0.17}$	$0.07^{+0.01}_{-0.01}$
γ_s	3.0	$\sim$	$\sim$	$\sim$	$\sim$
γ_h	4.5	$\sim$	$\sim$	$\sim$	$\sim$
x_s	0.61	0.48	0.48	0.51	0.62
χ^2/dof	367.15/377	454.16/383	433.20/380	396.41/379	424.00/381
$P_f[\%]$	< 0.01	0.23	0.06	< 0.01	< 0.01

Table 3.2: Summary of new model parameters.

	Parameter	Description
1	r_d	Disc radius in units of R_g
2	Δd	radial extension of the disc in units of R_g
3	N_{var}	fraction of hot flow variability in the disc at the truncation radius
4	$T_{d,max}$	maximum temperature in the disc [keV]
5	$\nu_{d,max}$	maximum viscous frequency in the disc [Hz]
6	x_s	fraction of disc emission in the soft band
7	n_h	hydrogen column density [$10^{22} cm^{-2}$]
8	ϕ_{qpo}	main QPO phase lag [cycles]
9	ϕ_{qpo2}	QPO second harmonic phase lag [cycles]
10	ϕ_{qpo3}	QPO third harmonic phase lag [cycles]
11	ϕ_{qpos}	QPO sub-harmonic phase lag [cycles]

Appendix

A) New PROPFLUC formalism

In the hot flow the viscous frequency is described by a smoothly broken power-law, in the disc we assume the following profile (Shakura & Sunyaev 1973):

$$\nu_{v,disc}(r) = \nu_{d,max} \left(\frac{r}{r_o} \right)^{-3/2} \tag{3.5}$$

where $\nu_{d,max}$, the maximum viscous frequency in the disc, is a model parameter.
We assume the amount of variability generated per radial decade in the hot flow to be constant (ID11, ID12, RIK14), while in the disc it follows a Gaussian profile peaking at the truncation radius r_o:

$$\sigma(r) = \sigma_o N_{var} e^{-\frac{1}{2}\left(\frac{r-r_o}{\Delta d}\right)^2)} \tag{3.6}$$

where the model parameters N_{var} and Δd govern amplitude of disc variability and radial extension of the varying disc respectively. In particular, considering that $\sigma_0 = F_{var}/\sqrt{N_{dec}}$, N_{var} estimates the amount of variability generated in the disc per radial decade as a fraction of the flow fractional variability F_{var}. When $N_{var} = 1$, the variability produced in the innermost ring of the disc is equal to the variability produced in the outermost ring of the hot flow. If the variability produced in the hot flow is larger than in the disc, it follows that $N_{var} < 1$.
As described in IK13, the flux observed in some energy band can be written in the following

way:

$$f_h(t) = \sum_{j=1}^{N} h(r_j)\dot{m}(r_j, t) \tag{3.7}$$

where the subscript h indicates the hard band (so that $f_h(t)$ is the flux observed in the hard band), $\dot{m}(r_j, t)$ represents the mass accretion rate fluctuations in the ring r_j, $h(r_j)$ is the number of photons coming from the ring r_j and detected in the hard band, and N is the total number of rings (disc plus hot flow rings). From the flux, we can compute the power spectrum in the hard band:

$$P_h(\nu) = |F_h(\nu)|^2 = \sum_{i,j=1}^{N} h(r_i)h(r_j)\dot{M}^*(r_i, \nu)\dot{M}(r_j, \nu) \tag{3.8}$$

here we adopt the convention that lower case and capital letters indicate time series and Fourier transforms respectively (unless specified differently), and the symbol * stands for complex conjugation.

The weighting factors $h(r_j)$ depend on how many photons are detected in a selected energy band, so on photons emitted and on the instrument response. The general expression for $h(r_j)$ factors is the following:

$$\begin{aligned} h(r) &\propto \sum_{I_{min}}^{I_{max}} Q(r, I) \\ &= \int_0^{\infty} A(r, E)M_a(E)dE \sum_{I_{min}}^{I_{max}} R_D(I, E) \end{aligned} \tag{3.9}$$

where $Q(r, I)$ represents the photon counts measured from ring r by our detector in the I^{th} energy channel, I_{min} and I_{max} are the boundaries of the channel range selected, $A(r, E)$ is the spectrum emitted from the radial bin centered at r (photons per unit time, unit energy, and unit telescope collecting area), $M_a(E)$ is the dimensionless absorption model, and $R_D(I, E)$ is the response of the detecting instrument.

In the new version of PROPFLUC, we assume that the spectrum emitted from a certain radius r in the disc is a blackbody with temperature $T(r) = T_{max}(r/r_o)^{-3/4}$ (Shakura & Sunyaev 1973). With this assumption, $A(r, E)$ is given by the Planck function.

In the absence of a full model for the spectrum emitted by the flow, we parametrize the weighting factors in the following way (IK13):

$$h_{flow}(r) \propto r^{(2-\gamma_h)}\Sigma(r) \tag{3.10}$$

where γ_h is the emissivity index for the hard energy band, and $\Sigma(r)$ is the surface density in the flow. The $h(r)$ values described so far have an arbitrary normalization, but in order to compare PROPFLUC computations with real data, we need to include some other parameter

taking into account the spectral characteristics of the source. Considering two energy bands, soft and hard (s and h respectively), we define the disc fraction in the soft band x_s as the fraction of total photons in the soft band that comes from the disc. x_s is a model parameter and can be estimated from spectral fitting. From x_s and the hardness ratio HR (the ratio between hard and soft photon counts), it is possible to compute the disc fraction in the hard band.

$$x_h = \frac{h_d/s_d}{HR} x_s \tag{3.11}$$

where $s_d \equiv \sum_{j=N_{flow}}^{N_{disc}} s(r_j)$, $h_d \equiv \sum_{j=N_{flow}}^{N_{disc}} h(r_j)$. Using the disc fraction in the hard band it is possible to normalize the $h(r)$ values of Eq. 3.9 and Eq. 3.9:

$$\tilde{h(r)} = \begin{cases} x_h h(r)/s_d & \text{if } r_n \text{ is in the varying disc} \\ (1-x_h)s(r)/s_f & \text{if } r_n \text{ is in the hot flow} \end{cases} \tag{3.12}$$

where $\tilde{h(r)}$ indicated the normalized counts in the hard band. Analogous equations for the soft band can be obtained by exchanging h with s.

B) Including the QPO

PROPFLUC assumes that the entire hot flow precesses because of frame dragging close to the BH. The precession of the hot flow modulates the emission producing a QPO in the power spectrum and, as described in ID11, ID12, and RIK14, the centroid frequency of the QPO depends both on the radial dimension of the hot flow and on its surface density profile. Modulation occurs mainly through two mechanisms: variation of the projected area of the hot flow towards the line of sight, and variations of the rate at which seed photons coming from the disc enter the hot flow and Compton up-scatter in the optically thin plasma (ID11, ID12, IK13). We can approximate the former case by multiplying the broad band noise time series with a time series representing the QPO. This is because the observed flux is $\sim L(t)\Omega(t)$, where $L(t)$ is the intrinsic luminosity, which contains the broad band noise, and $\Omega(t)$ is the solid angle subtended by the flow, which is varying quasi-periodically. We can approximate the latter case by adding the broad band noise and QPO time series, since an increase in seed photons adds to the total luminosity available for the hot flow to re-emit. If we make the simplifying assumption that the QPO and broad band noise time series are not correlated with one another and, for the additive case, that the mean of the QPO time series is zero, we can calculate the resulting power spectrum for both cases analytically (IK13).
Now we are fitting also to the cross-spectrum, we must consider how to treat lags intrinsic to the QPO signal. We can define soft and hard band QPO signals, $q_s(t)$ and $q_h(t)$, with Fourier transforms $Q_s(\nu)$ and $Q_h(\nu)$ respectively, such that the cross-spectrum of the QPO signals is $Q_s^*(\nu)Q_h(\nu) = |Q_s(\nu)||Q_h(\nu)|e^{i\phi(\nu)}$ (where $\phi(\nu)$ is the lag between the soft and hard energy band at frequency ν). For the additive case, the total flux observed in the soft band

is $f_{tot,s}(t) = f_s(t) + q_s(t)$ (with a similar expression for the hard band). Using the above assumptions, the cross-spectrum of the total flux is:

$$\begin{aligned} C(\nu) &= F^*_{tot,s}(\nu)F_{tot,h}(\nu) \\ &= F^*_s(\nu)F_h(\nu) + |Q_s(\nu)||Q_h(\nu)|e^{i\phi(\nu)} \end{aligned} \tag{3.13}$$

Following previous versions of PROPFLUC (see IK13), we model $|Q_s(\nu)|$ and $|Q_h(\nu)|$ as a sum of Lorentzian functions, each representing a different harmonic:

$$|Q_{s/h}(\nu)|^2 = \sum_{k=1}^{4} |Q_{s/h}(k,\nu)|^2 \tag{3.14}$$

where we consider a total of 4 harmonics (k = 1-4), one being a sub-harmonic (k = 4). We then need to make an assumption for the form of the phase, $\phi(\nu)$. The simplest treatment is to also break $\phi(\nu)$ down into harmonics so that we can specify only one model parameter per harmonic, ϕ_k, in order to characterize the QPO phase lags, rather than an entire (unknown) function, $\phi(\nu)$. Eq. 3.14 follows from this because, at the peak frequency of one harmonic in the soft band, the power in all the other harmonics in the hard band is very low (and vice versa). In the additive case, the cross-spectrum becomes:

$$C(\nu) = F^*_s(\nu)F_h(\nu) + \sum_{k=1}^{4} |Q_s(\nu)||Q_h(\nu)|e^{i\phi_k} \tag{3.15}$$

and we can fit features in the cross-spectrum attributable to the QPO using only one parameter for QPO phase per non-zero harmonic. Note that Eq. 3.15 is the equivalent of fitting the real and imaginary part of the cross-spectrum with our broad band noise model plus a sum of Lorentzian functions representing the QPO, with the centroid and widths tied between real and imaginary parts, but with the Lorentzian normalizations free to be different between real and imaginary parts. This is a favorable treatment, since it is the simplest possible way of accounting for phase lags contributed by the QPO, and it is the treatment we adopt in this paper.

If we were to instead consider the multiplicative case, equation 3.15 picks up an extra term, becoming:

$$\begin{aligned} C(\nu) = \quad & F^*_s(\nu)F_h(\nu) + \sum_{k=1}^{4} |\tilde{Q}_s(k,\nu)||\tilde{Q}_h(k,\nu)|e^{i\phi_k} + \\ & \tilde{F}^*_s(\nu)\tilde{F}_h(\nu) \otimes \sum_{k=1}^{4} |\tilde{Q}_s(k,\nu)||\tilde{Q}_h(k,\nu)|e^{i\phi_k} \end{aligned} \tag{3.16}$$

Here, the $\otimes$ denotes a convolution, and we employ the convention from IK13 that a tilde signifies zero mean in time space and a zero $\nu = 0$ component in Fourier space (i.e. $\tilde{x}(t) = x(t) - \langle x(t) \rangle$ or $\tilde{X}(\nu) = X(\nu) - X(0)\delta(\nu)$). Because of the convolution, the third term in

this equation can be fairly broad in Fourier space. Therefore the parameters ϕ_k can have an influence on frequencies in the cross-spectrum not dominated by the QPO signal. This is best avoided, since our assumptions regarding the QPO are rather *ad hoc*. We note, however, that the first and second terms in Eq. 3.16 have amplitudes of $\sim \sigma^2_{bbn}$ (the fractional variability amplitude of the broad band noise) and $\sim \sigma^2_{qpo}$ (the fractional variability of the QPO) respectively, whereas the amplitude of the problematic third term is $\sigma^2_{bbn}\sigma^2_{qpo}$. Since σ_{bbn} and σ_{qpo} are both ~ 0.1, the third term is small compared to the other terms and so the additive and multiplicative cases are reasonably similar to one another.

4

Cross-spectral modelling of the black hole X-ray binary XTE J1550-564: challenges to the propagating fluctuations paradigm

S. Rapisarda, A. Ingram and M. van der Klis

Submitted to Monthly Notices of the Royal Astronomical Sociaty

Abstract

Timing properties of black hole X-ray binaries in outburst can be modelled with mass accretion rate fluctuations propagating towards the black hole. Such models predict time lags between energy bands due to propagation delays. First application of a propagating fluctuations model to black hole power spectra showed good agreement with the data. Indeed, hard lags observed from these systems appear to be in agreement with this generic prediction.
Our PROPFLUC code allows us to simultaneously predict power spectra, time lags and coherence of the variability as a function of energy. This was successfully applied to the *Swift* data of MAXI J1659-152, fitting jointly the power spectra in two energy bands and the cross-spectrum between these two bands. In this work, we attempt to to model two high signal-to-noise *Rossi X-ray Timing Explorer* (RXTE) observations of XTE J1550-564. We find that neither observation can be adequately explained by the model even when considering, additionally to previous PROPFLUC versions, different propagation speeds of the fluctuations. After extensive exploration of model extensions, we tentatively conclude that the quantitative and qualitative discrepancy between model predictions and data is generic to the propagating fluctuations paradigm. This result encourages further investigation of the fundamental hypotheses of the propagating fluctuations model. We discuss some of these hypotheses with an eye to future works.

4.1 Introduction

Low-mass black hole X-ray binaries (BHBs) are optimal laboratories for studying the physics of accretion. To investigate the geometry of, and the mechanism regulating, accretion, it is necessary to observe the spectral and timing characteristics of the source. During the rising phase of an outburst, these characteristics radically change on time-scale of days/weeks (e.g. Belloni et al. 2005; Remillard & McClintock 2006; van der Klis 2004; Belloni 2010; Gilfanov 2010). At the beginning of the outburst, when the luminosity is still low, the energy spectrum of the source is dominated by a non-thermal component usually modelled with a hard power law ($\Gamma \approx 1.5$). In this phase (also known as low-hard state, LHS), the power spectrum of the source is characterized by broad-band noise (rms $\approx 30\%$) and by a strong quasi periodic oscillation (QPO; e.g. Casella, Belloni & Stella 2005 and references therein). As the source luminosity increases, the power law softens ($\Gamma \approx 2.5$) and the energy spectrum shows a significant thermal component that can be modelled by a multi-temperature blackbody peaking at ≈ 1 keV. This component becomes dominant at maximum luminosity (high-soft state, HSS). In this transition, all the characteristic frequencies of the power spectral features increase (e.g. Wijnands & van der Klis 1998; Homan et al. 2001) and the amplitude of both broad-band noise and QPO decreases. The transition from LHS to HSS does not occur in the same way for all the BHBs, for example, in some cases, the very high state (VHS) is observed, which is characterized by high luminosity, a significant blackbody component, and a soft power law dominating the emission (e.g. Miyamoto et al. 1991; McClintock & Remillard 2006).

Assuming that each spectral component corresponds to a certain physical region, the changes described above indicate important variations in the geometry of the accreting system. If each region produces variability depending on its physical characteristics, the correlation between the varying emission in different energy bands is an important tool to study both the different regions and their mutual interaction. In particular, it is known that BHBs show a positive (hard) lag between variations in soft and hard energy band and that the amplitude of this lag depends both on Fourier frequency and energy.

The truncated disc model (e.g. Esin, McClintock & Narayan 1997; Done, Gierliński & Kubota 2007) is a good candidate for explaining the spectral transition described above: an optically thick geometrically thin disc is truncated at a certain radius $r_{\rm o}$ (truncation radius) larger than the last stable circular orbit (ISCO) and, inside this radius, accretion takes place through an optically thin (optical depth $\tau \sim 1.5$) geometrically thick hot flow. Disc photons illuminating the hot flow are Compton up-scattered by the hot flow high-energy electrons. This interaction both cools down the hot flow and produces the observed hard power-law emission (Thorne & Price 1975; Sunyaev & Truemper 1979). At the beginning of the outburst, the disc is truncated far away from the the BH, so that the X-ray spectrum is dominated by the non-thermal emission coming from the hot flow. As the mass accretion rate increases, the truncation radius moves towards the BH, the luminosity of disc photons illuminating the hot flow increases cooling it down (the power law softens) and the dominant spectral component

becomes the thermal multi-temperature blackbody disc emission.
Looking at the short time-scale variability (luminosity variations with time-scale from ms to $\approx$ 100s), it is possible to explain the timing properties of the source considering mass accretion rate fluctuations stirred up in every ring of the accreting region and propagating towards the BH (Lyubarskii 1997). Propagating mass accretion rate fluctuations have been claimed to naturally explain the linear rms-flux relation observed in BHBs (Uttley & McHardy 2001; Uttley et al. 2005; Heil, Vaughan & Uttley 2012), the fact that the variability is observed over several orders of magnitude in frequency (Lyubarskii 1997), and the hard lag between soft and hard emission (Kotov et al. 2001; Arevalo & Uttley 2006), but quantitative tests of these claims have so far been incomplete.
The reason for this is that, even though the truncated disc model and the mass accretion rate fluctuation scenario may explain some of the observed phenomenology, a physical model that can self-consistently reproduce the energy spectrum, the power spectrum, and the correlation between different energy bands, has not yet been constructed. The model PROPFLUC (Ingram & Done 2011, 2012, hereafter ID11, ID12; Ingram & van der Klis 2013, IK13; Rapisarda et al. 2016, hereafter RIKK16, Chapter 3) is intended as a first step in this direction: the model is based on the truncated disc geometry and assumes that mass accretion rate fluctuations, stirred up both in the hot flow and in the disc, propagate towards the BH on a local viscous time-scale. In combination with this process of propagating fluctuations, the entire hot flow precesses because of frame dragging around the BH (Lense-Thirring precession) producing the QPO (Stella & Vietri 1998; Fragile et al. 2007; Ingram et al. 2016). The model outputs are power spectra in two different energy bands and the cross-spectrum between these bands. This implies that PROPFLUC can predict the phase lag and the correlation between the two bands.
RIKK16 applied the model to the BHB MAXI J1659-152 using the *Swift* data. In their study, PROPFLUC predictions showed to be in reasonable agreement with the data, but the data showed only small phase lags associated with the variability. In order to test PROPFLUC predictions and, ultimately, the validity of the propagating fluctuations hypothesis, we studied high s/n XTE J1550-564 observations showing significant phase lags.
XTE J1550-564 is a BHB first detected with the All-Sky monitor (ASM; Levine et al. 1996) on board of the *Rossi X-ray Timing Explorer* (RXTE) on 1998 September 7 (Smith 1998). Since its discovery, the source has gone into outburst four times, but the first outburst (1998-1999) remains the most luminous and best monitored outburst of the source ever observed with RXTE. The rising part of this outburst (first 12 days from the discovery) is characterized by a transition between LHS and VHS (Sobczak et al. 2000; Kubota & Done 2004). The power spectrum of the source in this phase shows broad-band noise and a strong QPO signal (Cui et al. 1999, Remillard et al. 2002). In our study we analysed 12 observations from the beginning of the outburst, in particular we performed spectral analysis in a full band (1.94-20.30 keV) and timing analysis in two energy bands (1.94-12.99 keV and 13.36-20.30 keV, soft and hard band respectively). For testing PROPFLUC, we selected two observations (2 and 7 days after the discovery, respectively) characterized by different count rate and power

spectral shape in the soft and hard band. We jointly fitted soft and hard band power spectra, and the cross-spectrum between these bands.
In Sec. 4.2, we present a number of updates to PROPFLUC intended to deal with the more complex variability characteristics of XTE J1550-564. In particular we add the option of extra variability in the inner part of the hot flow, and two new parameters describing the damping strength and the propagation velocity of the fluctuations. Secs 4.3 and 4.4 describe the techniques used for reducing the data and the PROPFLUC fit results, respectively. For both observations, the PROPFLUC prediction disagrees with the data for any acceptable combination of fit parameters. In Sec. 4.5, we discuss the implication of this result and possible, more complex, physical scenarios not considered in PROPFLUC. In Sec. 4.6, we summarize our results.

4.2 PROPFLUC updates

PROPFLUC (ID11, ID12, IK13) assumes that mass accretion rate fluctuations propagate through a truncated disc/hot flow geometry, where the entire hot flow is precessing because of frame dragging in the vicinity of a rotating BH (Lense-Thirring precession). RIKK16 improved the model in order to consider variability generated in and propagating from the truncated disc through the hot flow, and to simultaneously fit power spectra in two different energy bands and the complex cross-spectrum between these bands. Here, we introduce three extra updates to the model: 1) we consider the hypothesis of extra variability stirred up in the inner part of the hot flow; 2) we introduce a new parameter for taking into account the damping of mass accretion rate fluctuations as they propagate towards the BH; 3) we introduce a multiplicative factor regulating the propagation speed of the fluctuations. These updates are intended to make the PROPFLUC prescription resemble more closely a real accretion flow and extend the model capabilities in order to fit the complex variability observed in XTE J1550-564 (and in general in BHBs).

4.2.1 Summary of the PROPFLUC model

The accreting region assumed by PROPFLUC consists of an optically thick geometrically thin disc and a optically thin geometrically thick hot flow (red and blue horizontal bars in Fig. 4.1, respectively). The region in the disc contributing to the variability extends from the truncation radius $r_{\rm o}$ up to a radius r_d smaller than the outer edge of the disc. The hot flow extends from an inner radius $r_{\rm i}$ out to $r_{\rm o}$. The inner radius $r_{\rm i}$ is equal to or larger than the innermost stable circular orbit (ISCO), so that $r_{\rm d} > r_{\rm o} > r_{\rm i} > r_{ISCO}$. We adopt the convention that lowercase r corresponds to radial coordinate scaled by gravitational radius: $r = R/R_g$, where $R_g = GM/c^2$.
For numerical purposes, both disc and hot flow are split into rings whose boundaries are equally logarithmically spaced. The model resolution, i.e. the number of rings per radial decade N_{dec}, is the same for both disc and hot flow. Each ring produces a Lorentzian spec-

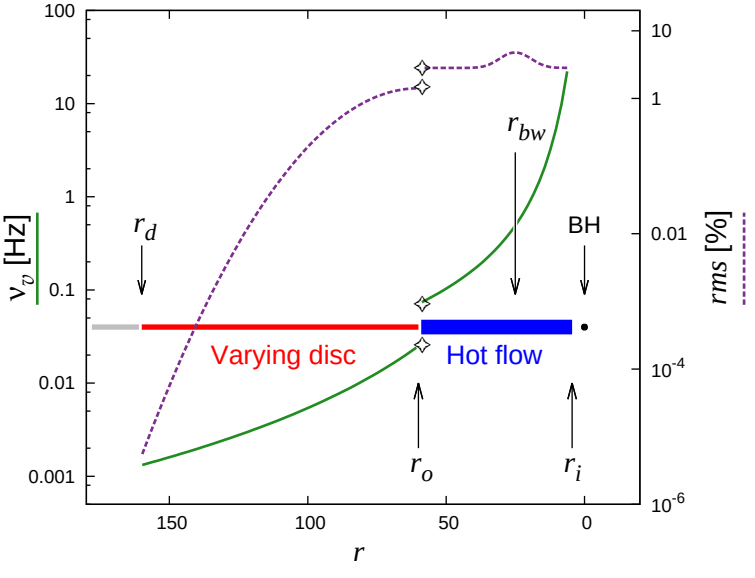

Figure 4.1: Viscous frequency (green solid line) and amount of variability produced by each ring (purple dashed line) versus the radial coordinate covering truncated disc and hot flow. The variability profile is Gaussian around the transition radius $r_{\rm bw}$. This extra variability in the hot flow, coupled with the variability stirred up in and propagating from the disc, produces a three hump power spectrum.

trum of mass accretion rate fluctuations with characteristic frequency equal to the local viscous frequency. These fluctuations propagate towards the BH on a time-scale equal to the local viscous time-scale. The radial viscous frequency profile has thus the double role of determining the characteristic frequency of fluctuations stirred up in each ring and the propagation speed of these fluctuations.

In the disc, the viscous frequency depends on radius as in a Shakura-Sunyaev disc with constant viscosity parameter and scale-height: $\nu_{v,disc}(r) = \nu_{d,max}(r/r_{\rm o})^{-3/2}$ (Shakura & Sunyaev 1973). In this expression, $\nu_{d,max}$ is the maximum viscous frequency in the disc, obtained at $r_{\rm o}$, and is one of the model parameters (see Appendix A in Chapter 3 for details).

In the hot flow, the viscous frequency is described by a smoothly broken power law, i.e. two different power law indices set the viscous frequency profile for rings close and far from the BH respectively, with a smooth transition at the so-called *bending wave* radius (ID12, IK13, Chapter 2). Because at each radius the viscous frequency is inversely proportional to the surface density (Frank, King & Raine 2002), this radius marks a transition between two different density regimes in the hot flow: the surface density increases smoothly with radius at large radii, while at small radii, the surface density drops off towards the BH because of viscous torques. Numerical simulations (Fragile et al. 2007) show that a similar transition occurs in

the wavelength of the bending waves (which propagate warps throughout the hot flow and so influence its shape), suggesting that the surface density transition radius is set by the shape of the bending waves (Ingram et al. 2009). This transition/bending wave radius, $r_{\rm bw}$, is a model parameter and regulates how the material is distributed in the hot flow.
The green solid curve of Fig. 4.1 shows the viscous frequency in both the disc and the hot flow. The star symbols on the curve highlight the discontinuity of the viscous frequency trend at the truncation radius. It is this discontinuity of the physical properties of the propagating region that produces a double hump power spectrum (RIKK16, Chapter 3). The power spectrum resulting from propagating mass accretion rate fluctuations depends also on the amount of variability produced by each ring. This is described by the model parameter $F_{var} = \sigma(r)\sqrt{N_{dec}}$ (the fractional variability per radial decade), where $\sigma(r)$ is the amount of variability fractional rms injected at each radius. In the disc, $\sigma(r)$ is a Gaussian peaking at the truncation radius $r_{\rm o}$ (the amplitude and the width of the Gaussian are both model parameters), while in the hot flow it is assumed to be constant (Chapter 2 and 3).

4.2.2 Extra variability in the flow

Numerical simulations show that extra high-frequency continuum variability may be produced in the inner part of a tilted accretion flow (Fragile & Blaes 2008; Henisey, Blaes & Fragile 2012). The mechanism generating this extra variability is related to the changes in the accreting regime of the flow around the bending wave radius. Here we introduce a prescription to account for this extra variability in PROPFLUC: $\sigma(r)$ in the hot flow is now a Gaussian peaking at the transition radius $r_{\rm bw}$. The amplitude and the width of this Gaussian, N_{extra} and Δr respectively, are both model parameters.
The purple dashed line of Fig. 4.1 shows σ for both the disc and the hot flow. Fig. 4.2 shows the result of including extra variability in the inner part of the flow. The dotted line is the two-hump power spectrum resulting from mass accretion rate fluctuations produced both in the disc and in the hot flow and propagating towards the BH. Including extra variability in the hot flow, we obtain a third, high-frequency, hump in the power spectrum (label H in Fig. 4.2a), so a three-hump power spectrum. Because the inner part of the hot flow emits mostly in the hard band, we do not observe large phase lags associated with this third hump. However, the presence of the high frequency hump partly suppresses the lag associated with the hump produced by mass accretion rate fluctuations propagating only in the hot flow (main hump, M), as extra variability dilutes its cross-spectrum (see Fig. 4.2c around 10 Hz). The fringes observed at high frequency (see Fig. 4.2 above $\approx$ 10 Hz) are the result of interference between contributions from different rings.
With the additional hypothesis of extra variability in the hot flow, it is now possible to produce a double hump power spectrum in two different ways: combining variability from the disc and the hot flow (labels L and M in Fig. 4.2a) and variability coming only from the hot flow (labels M and H Fig. 4.2a). However, while by adjusting the PROPFLUC parameters it is possible to reproduce a double hump shape in the power spectrum in two different ways,

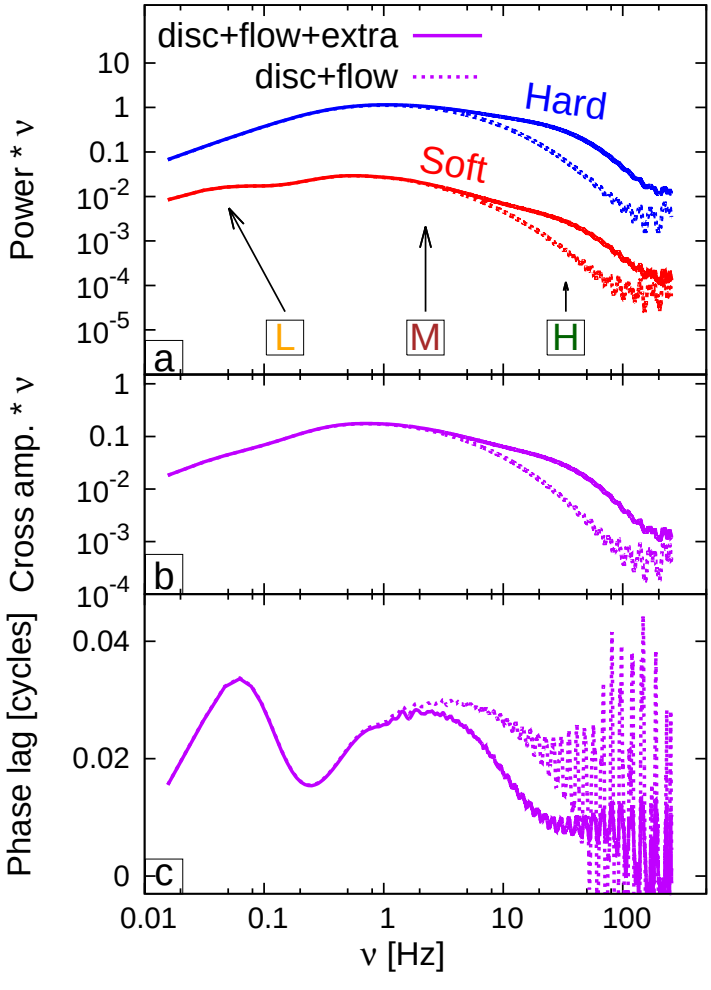

Figure 4.2: Soft (red line) and Hard (blue line) power spectrum (a), cross-spectral amplitude (b), and phase lag (c) computed considering mass accretion rate fluctuations propagating in the hot flow + disc (dashed line) and adding extra variability in the hot flow (solid line). In the latter case PROPFLUC produces a three-hump power spectrum combining disc variability (L, low frequency hump), hot flow variability (M, main hump), and extra variability in the hot flow (H, high frequency hump).

the two configurations (L-M and M-H) produce a different phase lag profile depending on the spectral properties of the source, i.e. on how thermal and non-thermal emission is distributed between the selected hard and soft bands.

4.2.3 The damping factor

The power spectrum of fluctuations stirred up in each ring of the hot flow is a broad Lorentzian with most of the variability power concentrated at the local viscous frequency. This assumption follows the fact that fluctuations with characteristic frequency higher than the local viscous frequency are strongly damped, so they never reach the inner part of the accreting system, where most of the emission comes from (Ingram 2016). This effect was analytically demonstrated by Churazov et al. (2001) for an optically thick geometrically thin disc, and in general it depends on the Green's function of the diffusion equation of the accreting system.
In PROPFLUC, the mass accretion rate at a certain radius $r_{\rm n}$ has so far been expressed in the following way (ID12, IK13):

$$\dot{m}(r_n, t) = \dot{m}_0(r_n) \prod_{l=1}^{n} a_l(t - \Delta t_{ln}) \tag{4.1}$$

where $\dot{m}_0(r_n)$ is the average mass accretion rate in $r_{\rm n}$, $\Delta t_{\rm ln}$ is the propagation time from $r_{\rm l}$ to $r_{\rm n}$, and $a_{\rm l}$ is the time series describing the fluctuation amplitude at $r_{\rm l}$.
Eq. 4.1 is a special case of the following expression:

$$\dot{m}(r_n, t) = \dot{m}_0(r_n) \prod_{l=1}^{n} g(r_l, r_n, t) \otimes a_l(t) \tag{4.2}$$

where the symbol $\otimes$ means convolution and $g(r_{\rm l}, r_{\rm n}, t)$ is the Green's function for propagation between $r_{\rm l}$ and $r_{\rm n}$, i.e. the function describing the diffusion of an infinitely narrow ring of material from $r_{\rm l}$ to $r_{\rm n}$. Eq. 4.1 describes inward-only propagation without spreading of the fluctuations, while Eq. 4.2 describes also inward-only propagation, but this time the ring is allowed to spread and the spreading is regulated by the Green's function $g(r_{\rm l}, r_{\rm n}, t)$. When $g(r_{\rm l}, r_{\rm n}, t)$ is equal to $\delta(t - \Delta t_{\rm ln})$, we obtain Eq. 4.1.
In order to take into account damping in the updated PROPFLUC model, we multiply power and cross-spectrum by a factor $e^{-D\Delta t_{ln}\nu}$, where D is a model parameter and ν is the frequency. This is equivalent to considering a Green's function with the following Fourier transform:

$$G(r_n, r_l, \nu) = e^{-D\Delta t_{ln}\nu} e^{-i2\pi\Delta t_{ln}\nu} \tag{4.3}$$

For every frequency ν, the argument of this Green's function is the phase shift in the fluctuations caused by the time it takes to propagate between the radii $r_{\rm l}$ and $r_{\rm n}$, and its modulus damps the amplitude of the fluctuations depending to their frequency (high frequencies are more damped) and propagation time (fluctuations propagating from larger radii are more damped). The exact expressions for the power and cross-spectrum including damping are derived in Appendix A. This kind of prescription is analogous to the one used in Arevalo & Uttley (2006).
The left column of Fig. 4.3 shows double hump power spectra obtained considering extra

variability in the flow (configuration M-H, see previous section) and varying the damping factor D. Increasing D suppress the power in both hard and soft band. For the main hump (label M in Fig. 4.3a) the damping is more evident than for the high frequency hump (label H in Fig. 4.3a). This is because fluctuations that propagate longer in the hot flow are more damped. From suppression of variability follows a suppression of phase lags (see in Fig. 4.3c) as more delayed variability is preferentially suppressed.

4.2.4 The propagation delaying factor

PROPFLUC so far assumed that the propagation time-scale of mass accretion rate fluctuations is equal to the local viscous time-scale. In a preliminary analysis of XTE J1550-564 observations, we noticed that the amplitude of the lag predicted by PROPFLUC was systematically lower than the data. Considering a slower propagation speed would have produced larger lags without significantly modifying the power distribution. For this reason, similarly to Arevalo & Uttley (2006), we introduced a scaling factor x_{lag} to consider the possibility that fluctuations stirred up in a certain ring can propagate in a time-scale not necessary equal (but still proportional) to the local viscous time-scale:

$$\Delta t_{ln} = x_{lag} \frac{dr}{r} \sum_{q=l+1}^{n} t_{visc}(r_q) \tag{4.4}$$

where $\Delta t_{\rm ln}$ is the propagation time from $r_{\rm l}$ to $r_{\rm n}$, t_{visc} is the viscous time-scale, and dr is the thickness of the ring. When x_{lag} is larger than 1, the fluctuations propagate slower than the local viscous time-scale. Increasing x_{lag} clearly affects the phase lag profile (Fig. 4.3f). As pointed out by Arevalo & Uttley (2006), varying x_{lag} it is possible to obtain significant lags even if hard and soft emissivity profiles are very similar. However, x_{lag} also affects the power distribution (Fig. 4.3d), introducing complex degeneracy between the parameters regulating the amplitudes of the humps.

4.3 Observations and data analysis

We analysed data from the RXTE Proportional Counter Array (PCA; Jahoda et al. 1996) using 12 pointed observations performed on September 9 1998 (MJD 51065, observation ID 30188-06-01-01) and on September 16 1998 (MJD 51072, observation ID 30188-06-11-00). The observations each contain between ~ 2 and ~ 4 ks of data.
Spectral analysis was performed using HEASOFT 6.13: we extracted source and background spectrum from Standard2 data (16 s time resolution). We created a PCA response matrix (necessary for both spectral analysis and PROPFLUC fitting) for all the analysed spectra. Each energy spectrum was background subtracted and a systematic error of 0.5% was applied. We fitted the energy spectrum in the 3-20 keV range using XSPEC 12.8.2 (Arnaud 1996).

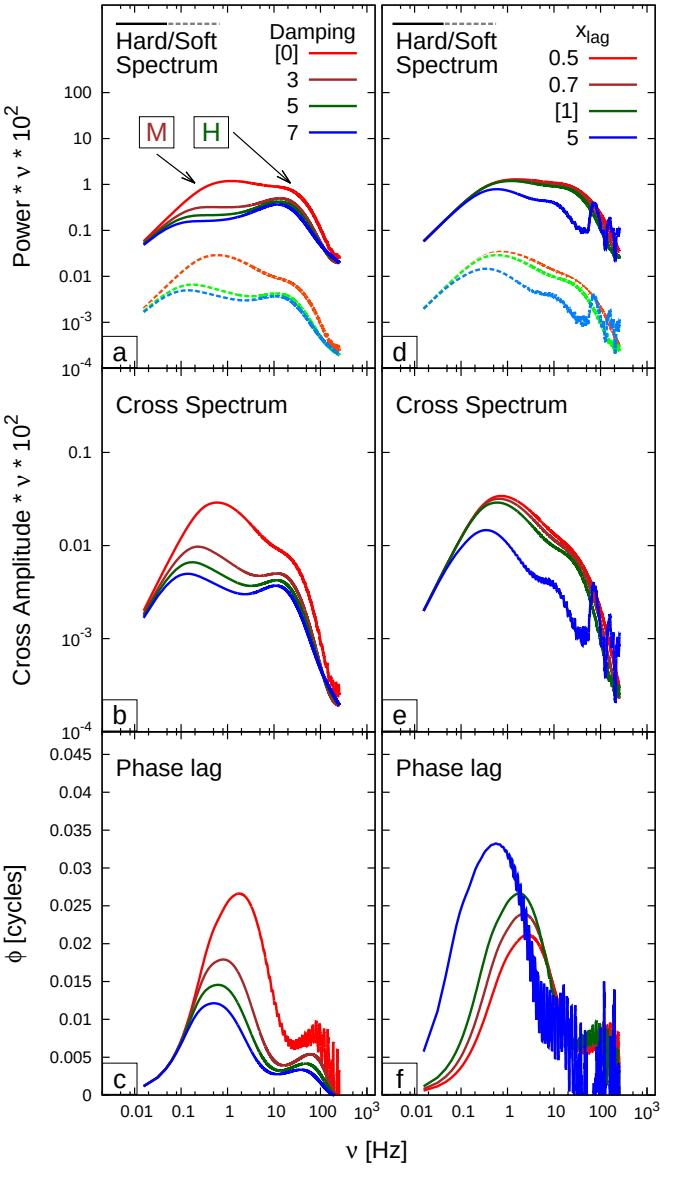

Figure 4.3: Soft (dashed line) and hard (solid line) double hump power spectra, cross-spectra, and phase lags computed varying the damping factor D and x_{lag}. The double hump power spectra consist of a main and a high-frequency hump (M-H configuration). Numbers in square brackets indicate the parameter value for all the other computations.

Following Axelsson et al. (2013), we used the model TBABS x GABS x (DISKBB + NTHCOMP + RFXCONV x NTHCOMP) (Mitsuda et al. 1984; Zdziarski, Johnson & Magdziarz 1996; Życki, Done & Smith 1999; Kolehmainen et al. 2011). The obtained results are consistent with the Axelsson et al. (2013) analysis. We extracted source and background light curves in two different energy bands (soft: 1.94-12.99 keV, and hard: 13.36-20.30 keV). From the background subtracted light curves, we computed the hardness ratio HR, i.e. the count rate ratio between hard and soft energy band. From spectral analysis we obtained the maximum disc temperature $T_{d,max}$ and we computed the disc fraction in the soft band x_s (for details on the role of HR and $T_{d,max}$ in PROPFLUC fits, see Appendix A in Chapter 3).
We used the $\approx$ 125 μs time resolution Single Bit mode and $\approx$ 16 μs time resolution Event mode for the Fourier timing analysis. For each observation, we computed Leahy-normalized power spectra in the soft and hard band, and cross-spectra between these two bands, using 256 s data segments and a time resolution of 1/8192 s, giving a frequency resolution of 1/256 $\approx$ 0.004 Hz and a Nyquist frequency of 4096 Hz. Leahy-normalized power and cross-spectra were then averaged, Poisson noise subtracted, and fractional rms normalized (for details about Leahy- and rms normalized cross-spectra, see Chapter 3, sec. 3.3). We did not apply any background correction in computing the Fourier analysis products.
For each observation, by integrating power- and cross-spectra, we computed the fractional rms for both hard and soft band, and phase lags between these bands, in three frequency ranges: low (0.004-0.2 Hz), mid (0.5-10 Hz), and high (10-40 Hz).

4.4 Results

4.4.1 Preliminary analysis

Fig. 4.4(b) shows fractional rms in the hard (blue points) and soft (red points) band for all the analysed observations. The phase lags between hard and soft band are shown in Fig. 4.4(c). These quantities are integrated over three frequency ranges: low-, mid-, and high-frequency. Note that the mid-frequency range always contains the QPOs.
Looking at the evolution of the properties of the source during this first, rising phase, of the outburst, we identify a change in evolution at observation 7 (vertical orange line in Fig. 4.4). The main indicators of this change are soft and hard rms in low frequency range, and the phase lag trend in all the frequency ranges. Up to observation 7, soft and hard rms show a clear decreasing trend in the low-frequency range. From observation 7, hard and soft rms are almost constant in all the frequency ranges. The mid-frequency range phase lag is smoothly decreasing from observation 2 to 7, leveling off afterward. Up to observation 6, low- and high-frequency ranges show smaller phase lags than the mid-frequency range. After an initial correlation from observation 1 to 5, low- and high- frequency ranges show two opposite trends: increasing in the former and decreasing in the latter. From observation 7, the phase lags in the mid-frequency range are close to zero, while the largest lags are now observed in the low-frequency range, and the high-frequency range has negative lags.

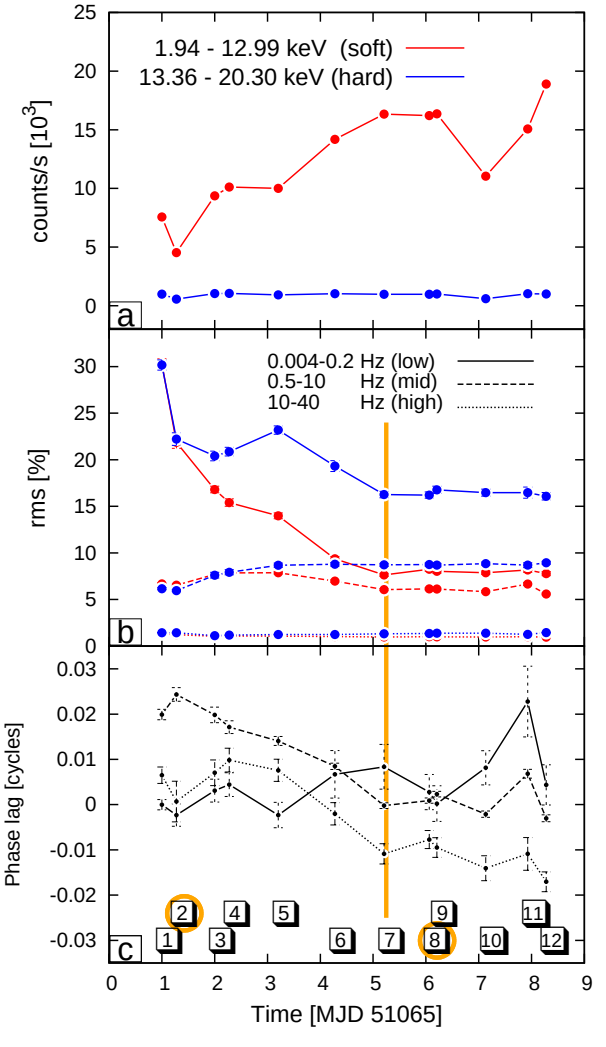

Figure 4.4: Integrated rms (b) in the hard (blue points) and soft (red points) band in three frequency ranges: low- (solid line), mid- (dashed line), and high-frequency (dotted line). Panel c shows the phase lags between these two bands integrated over the same frequency ranges. Panel a shows the hard and soft count rate in the full frequency range. The analysed observations are labelled from 1 to 12 in panel c. The orange vertical bar highlights the transition observed in the characteristics of the source at observation 7. The orange circles indicate the observations fitted with PROPFLUC.

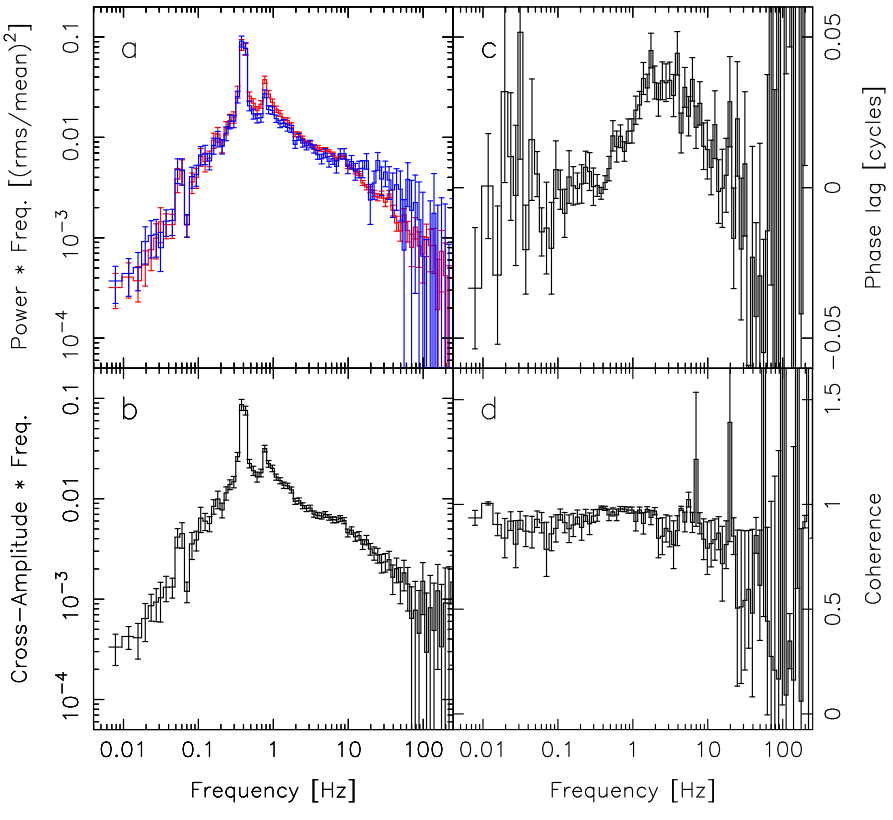

Figure 4.5: Hard (blue line) and soft (red line) power (a), cross-spectrum (b), phase lag (c), and intrinsic coherence (d) of the first observation (30199-06-01-01).

In order to test PROPFLUC predictions using the broadest variety of observed characteristics, we selected two observations, before and after the transition respectively. These two observations (orange circles in Fig. 4.4*c*) show very different observational characteristics: in the first selected observation (MJD 51065, observation ID 30188-06-01-01, $\sim$ 2.2 ks, Fig. 4.5) soft and hard rms are almost identical at all the frequencies (Fig. 4.4b) and soft and hard power spectra are very similar (Fig. 4.5a). This observation is characterized by positive (hard) phase lags that are largest in the mid-frequency range (Fig. 4.4c, dashed line). In the second observation (MJD 51070, observation ID 30188-06-07-00, $\sim$ 3.8 ks, Fig. 4.6) the rms in the hard band is larger than in the soft band, especially in the low-frequency range (Fig. 4.4b, solid line), and the hard power exceeds the soft power, principally below 1 Hz (Fig. 4.6a). In this observation the largest phase lags are observed in the low-frequency range (Fig. 4.4c, solid line). The two observations clearly differ also in count rate (Fig. 4.4a) and intrinsic coherence (panel *d* of Figs 4.5 and 4.6).

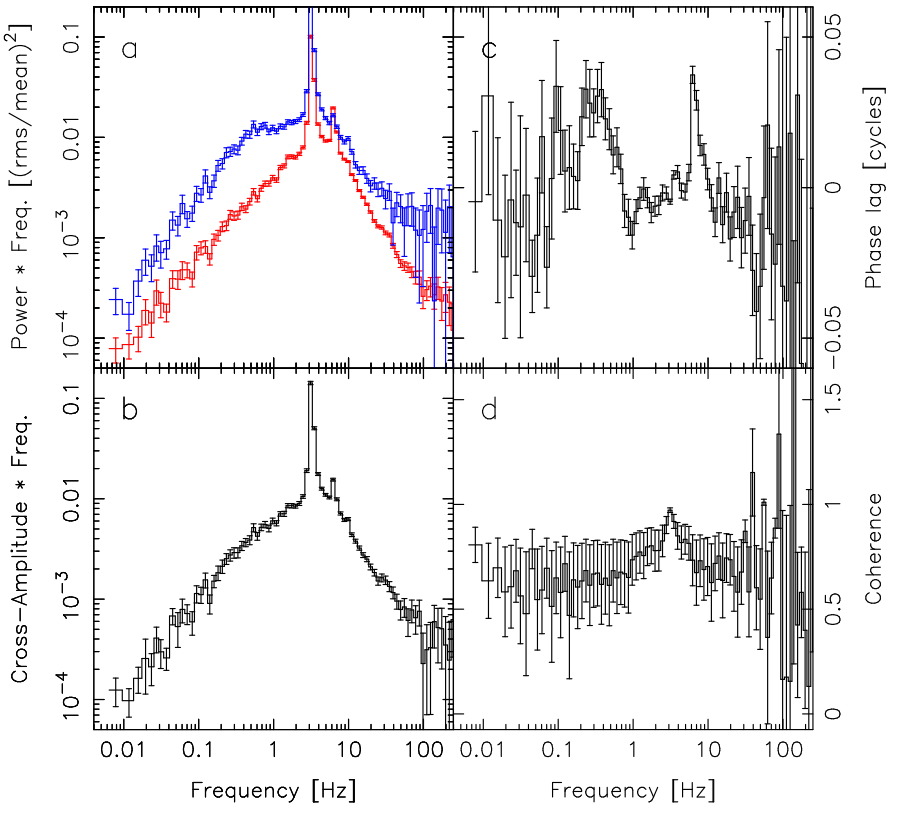

Figure 4.6: Hard (blue line) and soft (red line) power (a), cross-spectrum (b), phase lag (c), and intrinsic coherence (d) of the second observation (30199-06-07-00).

4.4.2 PROPFLUC fits

We jointly fitted logarithmically binned soft and hard power spectra, and cross-spectra between the two bands in the frequency range 0.004-100 Hz. The resolution is the same for both data and model. A QPO 1st and 2nd harmonic were added to the broad-band variability following the prescription described in Chapter 3, Appendix B. For a complete description of the model parameters and how these affect cross- and power spectrum, we refer to Rapisarda et al. (2014) and RIKK16 (Chapter 2 and 3 respectively). Tab. 4.1 provides a summary of the model parameters affecting low-, main, and high-frequency hump (the description of QPO parameters is omitted for conciseness). Additionally to what is described in Tab. 4.1, we note that the maximum temperature in the disc $T_{d,max}$, the disc fraction in the soft band x_s, and the hardness ratio HR (the count ratio ratio between hard and soft band) together set the disc emissivity as a function of radius in the soft and hard band. We obtained all these parameters from spectral analysis and flux measurements. The main parameters related to the QPO (1st

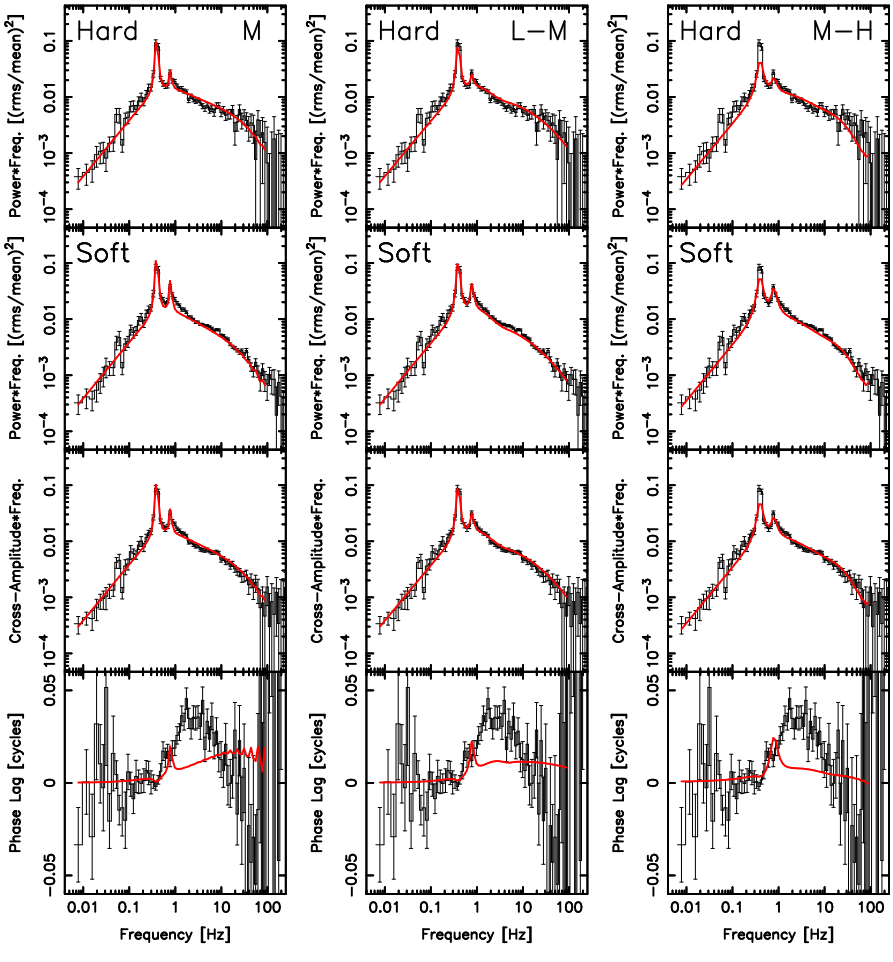

Figure 4.7: Best fit of observation 1 (solid red line) in three different hump configurations: only main (M, first column), low-frequency and main (L-M, second column), main and high-frequency (M-H, third column).

+ 2nd harmonic rms, quality factor Q, and phase lags ϕ, for a total of 5 parameters) are free. For all the fits, we fixed the number of rings per radial decade (N_{dec} = 35), the hydrogen column density (n_H = 0.6 x 10^{22} cm^{-2}; Gierlinski & Done 2003), the mass (M = 10 $M_{\odot}$), and the dimensionless spin parameter of the BH (a_* = 0.5). For both the observations, we tried to fit the data using four different hump configurations: only main (M, 17 free parameters), main and high-frequency hump (M-H, 18 free parameters), low-frequency and main hump (L-M, 17 free parameters), and the combination of all the three humps (L-M-H, 19 free parameters). In the M configuration, we varied the parameters regulating the surface density profile (λ, ζ, κ), and thereby the radial dependence of the viscous frequency. For all the other

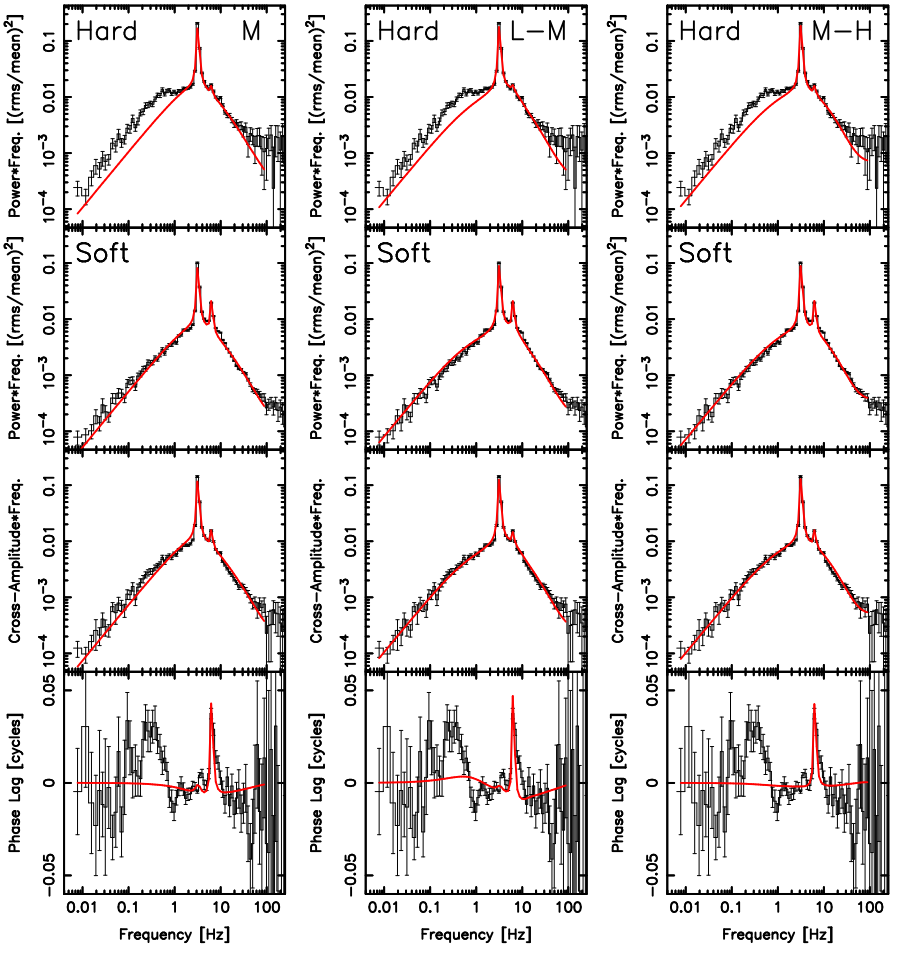

Figure 4.8: Best fit of observation 2 (solid red line) in three different hump configurations: only main (M, first column), low-frequency and main (L-M, second column), main and high-frequency (M-H, third column).

configurations, we fixed the surface density profile ($\lambda = 0.9$, $\zeta = 0$, $\kappa = 3$). While the number of free parameters in our fit seems quite large, we find that due to the high predictive power of the model, and the highly constraining nature of our formalism, using four independently measured quantities at each Fourier frequency (the power spectrum in the soft and hard band, and the real and imaginary part of the cross-spectrum between these two bands), most of the fit parameters are very well constrained by data of this high quality. Figs 4.7 and 4.8 show the best fit (solid red curve) in three different configurations (M, L-M, M-H). The best-fitting results are reported in Tab. 4.2. The results obtained using the L-M-H configuration are very similar to the L-M configuration, therefore they are omitted in our discussion. The narrow

features in the predicted phase lags are associated with the QPO 1st and 2nd harmonic.

First observation: 30199-06-01-01

This observation is characterized by a very similar hard and soft power spectral shape, and a phase lag bump between ≈ 0.5 and 10 Hz (Fig. 4.5). We could reproduce the power spectral shape with each of the three hump configurations (M, L-M, and M-H, see Fig. 4.7). The configurations L-M and M-H (double hump power spectrum) better predict the high frequency power. The predicted phase lags clearly disagree with data for all the configurations. In particular, PROPFLUC underestimates the lag between ≈ 0.5 and 10 Hz, so we could not get a statistically acceptable fit (see χ^2 in Tab. 4.2). This is because the emissivity indices necessary to fit the power are too similar to produce the observed lags (see $\Delta\gamma$ in Tab. 4.2).

Second observation: 30199-06-07-00

This observation is characterized by a different hard and soft power spectral shape, in particular the fractional rms in the hard band is higher than in the soft band at all the frequencies and the hard power spectrum shows a broad shoulder at ≈ 0.7 Hz absent from the soft power spectrum (Fig. 4.6). The main feature in the phase lag profile is a bump between ≈ 0.1 and 1 Hz. Fitting the data with the all the available configurations, we could not reproduce the difference between soft and hard power spectral shape. In particular, PROPFLUC always underestimates the hard power below ≈ 0.7 Hz (Fig. 4.8). Furthermore, the best-fitting emissivity index in the soft band is always larger than in the hard band. This suggests a rather unphysical scenario where the softer emission comes from the inner part of the flow. The phase lags are also underestimated between ≈ 0.1 and 0.7 Hz. All these discrepancies lead, again, to a statistically unacceptable fit (see χ^2 in Tab. 4.2).

4.5 Discussion

We tested the propagating fluctuations model on two high signal to noise RXTE observations of the BHB XTE J1550-564 during the rising phase of its 1998-1999 outburst, relaxing several of the constrains on the generation and propagation of the fluctuations by introducing additional free parameters. We jointly fitted power density spectra in two energy bands and the complex cross-spectrum between the two bands. This is the most stringent test of the model to date requiring the model to correctly predict amplitude, time lags, and coherence of the variability in and between the two energy bands chosen: our formalism uses all the information contained in the spectral variability that can be extracted by Fourier analysis in two energy bands.

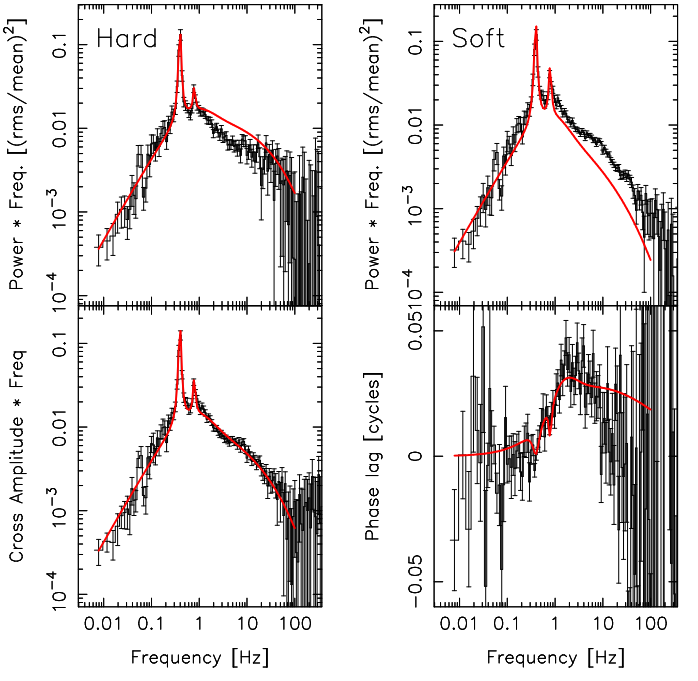

Figure 4.9: Best fit of observation 1 (red line) obtained using the M (single hump) configuration and fitting only the cross-spectrum

4.5.1 Fit to XTE J1550-564 observations

We fitted the two selected observations considering all the possible hump configurations: M, L-M, M-H, and L-M-H. Additionally to previous applications of PROPFLUC (ID12; IK13; Chapters 2 and 3), we considered damping, different fluctuation propagating speeds, and different hump configurations. Even using these new features we found that the model cannot explain the data: the χ^2 is not acceptable and, even more importantly, there are qualitative differences between observed power/cross-spectra and model predictions. As described below, these discrepancies appear to be generic to the propagating fluctuations idea.

The first observation shows hard lags (the bump between ≈ 0.7 and 10 Hz) in combination with almost identical hard and soft power spectra up to ≈ 10 Hz. Propagating fluctuation models assume that different time-scale variability is generated at different radii and that mass accretion rate fluctuations propagate from larger to smaller radii. In such scenarios, the positive (hard) phase lags occur because the hard band has a steeper emissivity profile than the soft band, as previously concluded by, e.g., Kotov et al. (2001) and Arevalo & Uttley (2006). Therefore, the hard power spectrum is more weighted to the faster characteristic frequencies of the inner regions than the soft band. When we use PROPFLUC to quantitatively confront these model ideas with observations, we find that in the first observation the simi-

larity between soft and hard power spectra up to $\approx$ 10 Hz requires emissivity profiles for the two bands that are very close to each other (see $\Delta\gamma$ in Tab. 4.2), which, as expected from the generic argument above, leads to predicted phase lags close to zero, in evident contradiction to the data. We note that fitting *only* the cross-spectrum, PROPFLUC can reproduce the phase lags of the first observation, but the best-fitting emissivity indices do not reproduce the power spectral shape observed in the soft and hard band (see Fig. 4.9). When we jointly fit power and cross-spectrum, we obtain a better χ^2 reproducing the shape of the power spectrum instead of the phase lags. This is because the error bars of the power are smaller than the phase lags.
The second observation shows a difference between hard and soft power spectra; in particular the hard power spectrum is characterized by a low-frequency feature (around 0.7 Hz) that is absent from both the soft power and the cross-spectrum (see Fig. 4.6a and b). This suggests that the variability associated with this feature is uncorrelated with the variability in the soft band, as indeed confirmed by the small coherence at low frequency (Fig. 4.6c). We do not expect this behaviour if this slow variability originates from farthest from the BH and the hard band has a steeper emissivity than the soft band.
The observations, when considered quantitatively in the context of a propagation model, seem to have characteristics that are generically at variance with propagating fluctuation model expectations, and indeed our PROPFLUC fit attempts confirm this.

4.5.2 Possible explanations

QPO lags

In the observations we analysed (LHS state of XTE J1550-564), the QPO always dominates the rms and its frequency increases from $\approx$ 0.3 to 10 Hz. The presence of the phase lag bump between $\approx$ 1 and 10 Hz prevents us to clearly identify the lag associated with the QPO and its harmonics in the first part of the outburst (up to observation 6, see Fig. 4.4).
In PROPFLUC the QPO is modelled with an *ad hoc* prescription producing features in the phase lag versus frequency spectrum similar in width to those in the power spectrum (see Chapter 3, Appendix B). While this simple solution allowed to fit data characterized by strong QPOs (Chapters 2 and 3), this means we do not take into account possible more complex QPO characteristics. For example, we can not exclude that the QPO has broad higher harmonics contributing to both the power and the phase lag. Alternatively, the presence of the QPO might be part of a physical process that also influences the broad-band noise. Perhaps it is possible to obtain clues about the role of QPOs in the phase lag spectrum by comparing to sources that do not show strong QPOs, but similar broad-band noise and energy spectrum (Chapter 5).

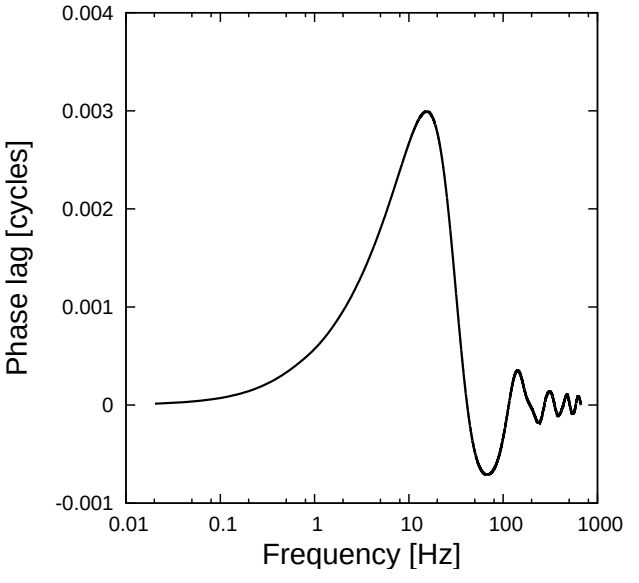

Figure 4.10: Phase lags resulting from reflection of X-ray emitted by an isotropic stationary source located 200 R_g above the BH. The amplitude of the lags is a factor 10 smaller than the data.

Reflection

The phase lags predicted by PROPFLUC are only due to the propagation of mass accretion rate fluctuations. However, it is well known that reflection contributes significantly to the spectrum, and this is true also for our selected observations (Axelsson et al. 2013). Photons from the hot flow are reflected by the disc, so that the reflected emission is delayed depending on the finite light travel time from the hot flow to the disc and on the size of the reflector (the disc). For the energy bands considered in our analysis, we expect more reflection in the hard band than in the soft band (since the Compton hump is harder than the continuum), so that reflection can contribute hard lags. Because of the finite size of the disc, the high frequency variability of the reflected component is suppressed (e.g. Gilfanov et al. 2000), so that the reflected emission affects both the way the soft and hard power are distributed between the frequencies, and the amplitude of the (hard) phase lags. In the first observation, the phase lag bump observed between $\approx$ 1 and 10 Hz cannot be produced by propagating fluctuations because of the similarity between the hard and soft power spectra. However, frequency dependent phase lags will be produced by hard photons emitted by the hot flow and reflected from the disc.

We tested the contribution of reflection by calculating a transfer function from a lamppost model formalism (X-rays are emitted from an isotropic stationary point some height h above

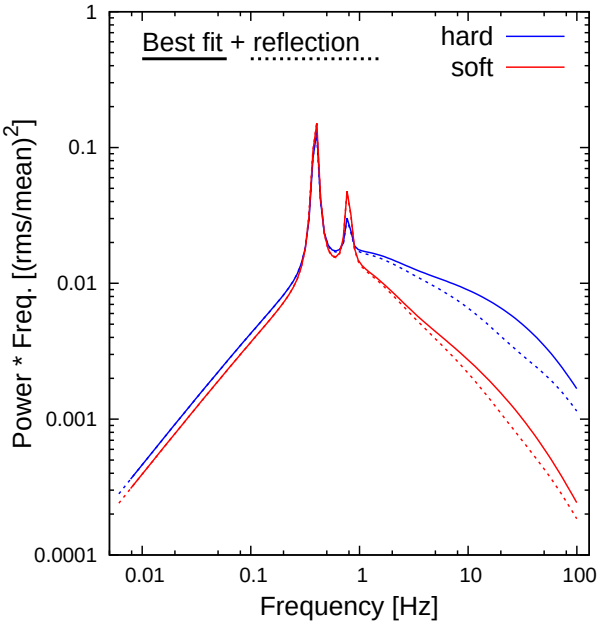

Figure 4.11: Power spectra resulting from including reflection to propagating fluctuations. Due to light travel effects, the reflected component dilutes the emission suppressing mainly the hard power at high frequencies.

the BH), ignoring light bending (e.g. Campana & Stella 1995). We assume the inner boundary of the reflector, $r_{in,refl}$, equal to the best-fitting truncation radius for the first observation, $r_{\rm o} = 42.3$, $i = 70°$. Our spectral fitting (see Sec. 4.3) indicates that reflection accounts for $\approx 16\%$ of the soft band flux and $\approx 23\%$ of the hard band flux. We calculate the hard lags that would result purely from reflection. Fig. 4.10 shows that, even assuming a very large $h = 200R_g$, the magnitude of the lag (≈ 0.003 cycles) is only a small fraction of the observed lag (≈ 0.04 cycles), and the lag peaks at a higher frequency than observed (we assume a 10 $M_\odot$ BH; increasing the mass would lower the frequency where the lag peaks). We note that it is possible to reproduce a lag of the required amplitude with reflection, but for rather implausible parameters. This requires considering the hard emission to come from ≈ 1 $R_{\rm g}$ and the soft emission to come from ≈ 200 $R_{\rm g}$, which is unlikely.

Fig. 4.9 shows that PROPFLUC can reproduce the phase lags observed in the first observation at the expense of a correct prediction of the power spectral shape in the soft and hard band. As mentioned at the beginning of this section, reflection can affect the shape of the power spectrum in the two bands. In particular, we want to explore the possibility that the *intrinsic* soft and hard power spectra are different from one another (allowing us to produce the observed hard lag), but, because of reflection, their shapes are modified to be similar to

one another, as observed in the data. In order to test the effect of reflection on the power distribution, we computed power spectra from the fit parameters of Fig. 4.9 including reflection and using the same setting adopted above (lamppost model, $r_{\rm o} = 42.3$, $i = 70^{\circ}$, $h = 200R_g$, see Appendix B for details). The power spectra obtained including reflection are shown in Fig. 4.11. Including reflection suppresses the power at high frequency, mainly in the hard band (this is because the hard band contains more reflection than the soft band). Although including reflection reduces the difference between hard and soft power spectrum, the model prediction is still far from the observed power spectral shapes (almost identical power distribution in both energy bands). Therefore, reflection, either purely or combined with propagating fluctuations, is unlikely to explain the discrepancies observed between data and model predictions. We note that Walton et al. (2013) reported on a variable AGN with almost no reflection feature, so this would provide a very good test for the propagation model.

Inwards and outwards propagation

As described in Sec. 4.2, PROPFLUC assumes a simplified diffusion mechanism, with fluctuations propagating only towards the BH and without spreading of the fluctuations during propagation. A more realistic approach would require considering a Green's function closer to proper diffusion, i.e. accounting for inwards and outwards propagation. Outward propagation could introduce soft phase lags leading to unintuitive results. This is beyond the scope of this study, but we highlight the importance of exploring fundamental principles of the propagation models as currently understood to check if the discrepancies we found in these XTE J1550-564 observations can be naturally addressed in a more physical description of the diffusion process (Mushtukov, Ingram & van der Klis in preparation).

Non-linear spectral variations

PROPFLUC assumes that the flux in a certain energy band is a linear combination of the mass accretion rate weighted fluxes of each ring (IK13). If the shape of the energy spectrum from each ring is not constant but varies with mass accretion rate, this approximation is not valid anymore. In a more realistic scenario, we expect the blackbody disc temperature and the Compton power law index to vary with mass accretion rate. If these variations are small enough, we could still represent the flux as a linear combination of the mass accretion rate at each ring linearizing the variations through Taylor expansion. So, in this case, we would not expect significant differences from the actual PROPFLUC predictions. Larger variations would lead to deviations from the power spectral shape and the phase lag profile predicted by a linear model like PROPFLUC. Exploring the characteristics of these deviations requires further quantitative exploration of our model. We plan to investigate the magnitude of these deviations in a future analysis.

4.6 Conclusions

We used the propagating mass accretion rate fluctuations model PROPFLUC to fit two observations in the LHS of XTE J1550-564. In our fit, we accounted for damping and different fluctuation propagation speeds. The model failed to reproduce the data both quantitatively (unacceptable reduced χ^2 values) and qualitatively. In the first observation, this could still be due to the simplistic QPO prescription adopted in PROPFLUC. However, in the second observation, the discrepancies between data and model predictions are a generic issue for propagation models and not specific to the PROPFLUC implementation. This result encourages a deeper investigation of the fundamental properties of the propagation model, with particular attention to the physical mechanism producing the QPO and how it affects the broad-band noise.

Appendix

A) Including damping

Eq. 4.2 describes the mass accretion rate at the $n^{\rm th}$ ring for a general Green's function assuming that fluctuations propagate only inwards. If we inject a narrow ($\delta-$function) ring of mass into the disc, the Green's function describes how that ring spreads out and eventually accretes onto the BH. Considering the Green's function of IK13 ($g(r_{n=1}, r_n, t) = \delta(t - \Delta t_{l,n})$), this ring would remain a narrow ring and simply move towards the BH at a velocity $r \cdot \nu_v(r)$. In a more realistic scenario, the ring will spread: some material will move towards the BH slower or faster than the average rate, and in general some material can even spread outwards from the starting point. Here, we generalize the IK13 formalism by considering a more general Green's function. We still assume only inwards propagation (since this vastly simplifies the Green's function solutions: Mushtukov, Ingram & van der Klis in preparation), but the form for the Green's function given in Equation (3) in the text allows for spreading of the ring.

Equation (2) implicitly assumes that the Green's function has the property:

$$g(r_l, r_n, t) = g(r_l, r_q, t) \otimes g(r_q, r_n, t), \tag{4.5}$$

or equivalently in Fourier space:

$$G(r_l, r_n, \nu) = G(r_l, r_q, \nu) G(r_q, r_n, \nu). \tag{4.6}$$

where ($r_l > r_q > r_n$). For a function describing propagation, it is rather unphysical to not have this property, since a fluctuation propagating from r_1 to r_3 must equal the same fluctuation propagating first from r_1 to r_2, and then from r_2 to r_3. The IK13 Green's function, $G(r_l, r_n, \nu) = \exp(i2\pi\Delta t_{l,n}\nu)$, has this property since $\Delta t_{l,n} = \Delta t_{l,q} + \Delta t_{q,n}$. The Green's function implemented here (Eq. 4.3) also has this property. Because this property holds,

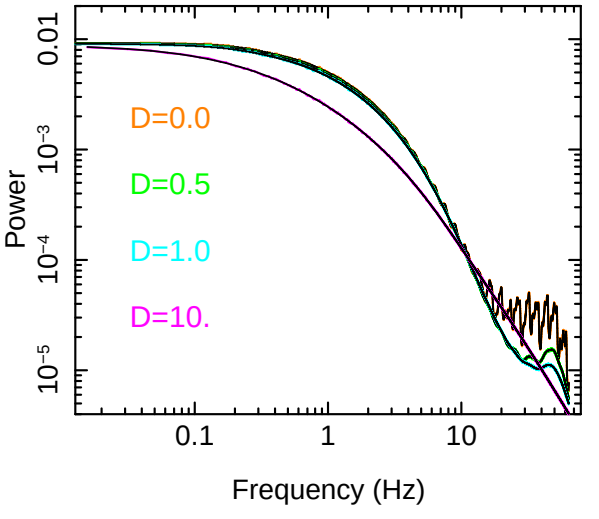

Figure 4.12: Single hump power spectrum (M configuration) predicted by the model. Different colours represent different values of the damping factor D. The colored lines are the average of 10000 iterations obtained using the Timmer & Koening (1995) prescription and the black lines are the analytic calculations.

the same arguments can be used as in IK13 (Appendix B therein) to show that the power spectrum of the mass accretion rate at r_n is

$$|\dot{M}(r_n,\nu)|^2 = \prod_{l=1}^{n} |G(r_l,r_n,\nu)|^2 |A_l(\nu)|^2. \tag{4.7}$$

Similarly, the cross-spectrum between $\dot{M}(r_n,\nu)$ and $\dot{M}(r_l,\nu)$ is

$$\dot{M}(r_n,\nu)\dot{M}^*(r_l,\nu) = \Lambda_{l,n} G(r_l,r_n,\nu)|\dot{M}(r_l,\nu)|^2, \tag{4.8}$$

where $\Lambda_{l,n}$ is the product of the mean mass accretion rate in each radius (following IK13). Since we assume the same mass accretion rate in each ring, we can always set $\Lambda_{l,n} = 1$. The power spectrum of the "hard band" flux becomes

$$P(\nu) = \sum_{n=1}^{\mathcal{N}} \Bigg[h_n^2 |\dot{M}(r_n,\nu)|^2 + 2\sum_{l=1}^{n-1} h_l h_n \Lambda_{ln} |G(r_l,r_n,\nu)| \cos\Phi_{l,n}(\nu) |\dot{M}(r_l,\nu)|^2 \Bigg] \tag{4.9}$$

where $\Phi_{l,n}(\nu) \equiv \arg[G(r_l,r_n,\nu)]$. For our Green's function (and also that of IK13), $\Phi_{l,n}(\nu) = 2\pi\Delta t_{l,n}\nu$. Fig. 4.12 shows that this calculation (black lines) gives the same result as using

the average of 10000 realisations obatined using the Timmer & Koenig (1995) prescription for a range of values of the damping factor D (coloured lines). This can be extended to the cross-spectrum between the "hard" and "soft" band, giving

$$\begin{aligned} C(\nu) &= \sum_{n=1}^{\mathcal{N}} \Bigg[h_n s_n |\dot{M}(r_n,\nu)|^2 \\ &+ \sum_{l=1}^{n-1} (h_l s_n e^{i\Phi_{l,n}(\nu)} + h_n s_l e^{-i\Phi_{l,n}(\nu)}) \\ &\times \Lambda_{ln} |G(r_l,r_n,\nu)||\dot{M}(r_l,\nu)|^2 \Bigg] \end{aligned} \tag{4.10}$$

B) Including reflection

We can represent the hard (soft) band flux as the sum of a direct and reflected component:

$$h(t) = d_h(t) + x_{r,h}[d_h(t) \otimes \tau(t)] \tag{4.11}$$

where $d_h(t)$ ($d_s(t)$) is the direct component in the hard (soft) band, $x_{r,h}$ ($x_{r,s}$) is the reflection fraction in the hard (soft) band, $\tau(t)$ is the impulse response function or transfer function, and $\otimes$ means convolution. We calculated the transfer function from a lamppost model formalism (X-rays are emitted from an isotropic stationary point at some height h above the BH) and ignoring light bending (e.g. Campana & Stella 1995). Normalizing $d_h(t)$ ($d_s(t)$) to have a mean of unity, the mean of $h(t)$ is $1 + x_{r,h}$ (the mean of $s(t)$ is $1 + x_{r,s}$).
Applying the Fourier transform, we obtain:

$$H(\nu) = D_h(\nu)[1 + x_{r,h} \times T(\nu)] \tag{4.12}$$

and the cross-spectrum between soft and hard band is:

$$S^*(\nu)H(\nu) = D_s^*(\nu)D_h(\nu)[1 + x_{r,s}T^*(\nu)][1 + x_{r,h}T(\nu)] \tag{4.13}$$

The power spectrum in the hard (soft) band is:

$$|H(\nu)|^2 = |D_h(\nu)|^2[1 + x_{r,h}^2|\tau(\nu)|^2 + 2x_{r,h}\,\mathrm{Re}\{T(\nu)\}] \tag{4.14}$$

Representing the power spectrum in the fractional rms normalization we obtain:

$$\begin{aligned} P_h(\nu) &= |H(\nu)|^2/(1 + x_{r,h})^2 \\ &= \frac{|D_h(\nu)|^2[1 + x_{r,h}^2|T(\nu)|^2 + 2x_{r,h}\,\mathrm{Re}\{T(\nu)\}]}{(1 + x_{r,h})^2} \end{aligned} \tag{4.15}$$

The presence of a stable reflected component affects both the shape and the normalization of the power spectrum.

Table 4.1: Short description of the PROPFLUC parameters.

Main hump parameters	
Σ_0	Surface density constant. It is a multiplicative factor for the surface density in the hot flow and it regulates the characteristic frequency of the main hump M.
F_{var}	Fractional variability per radial decade in the hot flow. It regulates the amplitude of the main hump power.
λ	Power law index determining the surface density profile in the hot flow for radii much smaller than the bending wave radius.
ζ	Power law index determining the surface density profile in the hot flow for radii much larger than the bending wave radius.
κ	Index regulating the sharpness of the transition between λ and ζ regime at the bending wave radius.
$r_{\rm i}$	Inner radius of the hot flow.
$r_{\rm bw}$	Bending wave radius. $r_{\rm bw}$ is in between $r_{\rm i}$ and $r_{\rm o}$.
$r_{\rm o}$	Truncation radius. It sets the outer edge of the hot flow and it is the main parameter affecting the QPO frequency.
γ_s	Emissivity profile index of the hot flow in the soft band.
γ_h	Emissivity profile index of the hot flow in the hard band.
Low-frequency hump parameters	
$r_{\rm o}$	Truncation radius. It sets the inner edge of the disc.
$r_{\rm d}$	Outer edge of the varying disc.
$\nu_{d,max}$	Maximum viscous frequency in the disc. It regulates the characteristic frequency of the low-frequency hump.
N_{var}	Amount of variability produced in the disc as a fraction of F_{var}. It regulates the amplitude of the low-frequency hump. When N_{var} = 0, no variability is produced in the disc. When N_{var} = 1, the amount of variability produced at the truncation radius in the disc is equal to F_{var}.
Δd	Radial extension of the varying disc. It affects both the characteristic frequency and the amplitude of the low-frequency hump.
$T_{d,max}$	Maximum temperature in the disc.
x_s	Fraction of disc photons emitted in the soft band.
High-frequency hump parameters	
$r_{\rm bw}$	Bending wave radius. It is the radius in the inner flow where the extra variability peaks.
N_{extra}	Amplitude of the extra variability in the hot flow.
Δr	Width of the high-frequency hump.
Global parameters	
M_{BH}	Mass of the BH.
a_*	Dimensionless spin parameter of the BH.
n_H	hydrogen column density in units of 10^{21} [atoms/cm^2].
Other information	
HR	Hardness ratio: count ratio between hard and soft band.
N_{dec}	Number of rings per radial decade in the hot flow and in the disc. It sets the resolution of the model.

Table 4.2: PROPFLUC best-fitting parameters to the first and second observation selected in our study (obs. ID 30188-06-01-01 and ID 30188-06-07-00, respectively). For each observation there are three columns corresponding to three different hump configurations: only main hump (M), main and high-frequency hump (M-H), and low-frequency and main hump (L-M). The subscripts s and h correspond to soft and hard band respectively. The symbol $\sim$ means that the parameter is fixed at the value of the previous column, the symbol $-$ means that the parameter was not used for that particular configuration.

Observation	First: 30188-06-01-01			Second: 30188-06-07-00		
Humps	M	L-M	M-H	M	L-M	M-H
Σ_0	19.61	0.26	3.99	1.71	1.28	6.38
$F_{var}[\%]$	27.18	50.45	33.27	106.28	114.47	36.05
ζ	1.9	0.0	$\sim$	0.0	0.0	$\sim$
λ	2.7	0.9	$\sim$	1.8	0.9	$\sim$
κ	20.0	3.0	$\sim$	3.3	3.0	$\sim$
r_i	4.5	$\sim$	$\sim$	$\sim$	$\sim$	$\sim$
r_{bw}	15.70	5.05	4.61	4.04	5.02	5.49
r_o	41.36	41.44	41.55	15.71	15.62	15.53
γ_s	9.90	2.70	5.71	2.60	1.14	3.81
γ_h	12.28	3.10	6.34	2.31	0.78	3.55
$(\Delta\gamma)$	2.38	0.40	0.63	-0.29	-0.36	-0.26
N_{var}	–	1.88	–	–	0.30	–
Δd	–	8.80	–	–	5.26	–
$\nu_{v,max}[Hz]$	–	1.52	–	–	1.62	–
$T_{d,max}$ [keV]	–	0.55	–	–	0.70	–
$x_s[\%]$	–	17	–	–	32	–
N_{shock}	–	–	2.15	–	–	3.92
Δr	–	–	0.77	–	–	2.31
D	0.0	0.9	0.1	1.1	2.1	2.2
x_{lag}	7.8	3.1	4.2	3.0	2.0	2.7
$M[M_\odot]$	10.0	$\sim$	$\sim$	$\sim$	$\sim$	$\sim$
a_*	0.5	$\sim$	$\sim$	$\sim$	$\sim$	$\sim$
$n_H[10^{22}cm^{-2}]$	0.6	$\sim$	$\sim$	$\sim$	$\sim$	$\sim$
χ^2_{red}	2.73	2.49	2.90	6.74	5.55	5.57
dof	403.00	404.00	403.00	403.00	404.00	403.00

5

Modelling hard and soft state of Cygnus X-1 with propagating mass accretion rate fluctuations

S. Rapisarda, A. Ingram and M. van der Klis

Submitted to Monthly Notices of the Royal Astronomical Sociaty

Abstract

We present a timing analysis of three *Rossi X-ray Timing Explorer* (RXTE) observations of the black hole binary Cygnus X-1 with the propagating mass accretion rate fluctuations model PROPFLUC. The model simultaneously predicts power spectra, time lags, and coherence of the variability as a function of energy. The observations cover the soft and the hard state of the source, and the transition between the two. We find good agreement between model predictions and data in the hard and soft state. Our analysis suggests that in the soft state the fluctuations propagate in an optically thin hot flow extending up to large radii above and below a stable optically thick disc. In the hard state, our results are consistent with a truncated disc geometry, where the hot flow extends radially inside the inner radius of the disc. In the transition from soft to hard state, the characteristics of the rapid variability are too complex to be successfully described with PROPFLUC. The surface density profile of the hot flow predicted by our model and the lack of QPOs in the soft and hard state, suggest that the spin of the black hole is aligned with the inner accretion disc and therefore probably with the rotational axis of the binary system.

5.1 Introduction

Up to date, the propagating mass accretion rate fluctuations model (Lyubarskii 1997; Kotov et al. 2001; Arevalo & Uttley 2006, hereafter AU06; Ingram & van der Klis 2013, hereafter IK13) is one of the most promising models for quantitatively explaining the rapid variability observed in black hole X-ray binaries (BHBs). In the low-hard state (LHS), when the energy spectrum is dominated by a power law ($\Gamma \approx 1.5$) and the luminosity is low, the rapid variability is characterized by broad band noise (fractional rms $\approx 30\%$) and by a strong quasi-periodic oscillation, or QPO (e.g. Remillard & McClintock 2006; Belloni 2010; Gilfanov 2010). The shape of the power spectrum can be quite complex, showing several broad band continuum components or "humps" in the frequency domain. The study of this variability in different energy bands revealed that hard X-ray variations are often delayed with respect to soft X-ray variations. The amplitude of this *hard lag* correlates with energy and it is larger for variations on longer time-scales (e.g. Miyamoto & Kitamoto 1989; Nowak et al. 1999a). In the propagating fluctuations scenario, broad band noise arises because of mass accretion rate fluctuations stirred up at each radius of the accretion flow and propagating towards the black hole (BH). If the spectrum of the region close to the BH is harder than that emitted at larger radii, the propagation of fluctuations naturally produces hard phase lags (Kotov et al. 2001; AU06). Propagating fluctuations also explain other observational characteristics of BHBs: the linear rms-flux relation on different time scales (Uttley & McHardy 2001), the high coherence of the variability across a broad range of energy bands (Vaughan & Nowak 1997; Nowak et al. 1999a), and the large amplitude of the X-ray variations (of tens of per cent fractional rms) observed over several decades of time-scales (e.g. Reig, Papadakis & Kylafis 2002).

Kotov et al. (2001) and AU06 made a first step in applying the propagating fluctuations paradigm quantitatively to BHBs. They showed that the model can predict the observed ratio between power in broad soft and hard bands, and the phase lag between these two energy bands for some selected Cygnus X-1 observations. The model PROPFLUC (IK13; Rapisarda et al. 2016, hereafter RIKK16, Chapter 3; Rapisarda, Ingram & van der Klis 2017 submitted, hereafter RIK17, Chapter 4) further explores the propagating fluctuations model predictions. PROPFLUC can produce multi-hump power spectra in different energy bands assuming fluctuations stirred up in and propagating from a truncated disc (optically thick and geometrically thin) through a hot flow (optically thin and geometrically thick). This means the model also predicts the frequency-dependent phase lag between soft and hard energy band. Supplementing propagating fluctuations with solid-body precession of the entire hot flow, the model produces a QPO on top of the broad band noise. The model predicts amplitude, phase lags, and coherence of the rapid variability in and between the soft and hard bands. This represents the complete information that can be extracted by first- and second-order Fourier analysis from the variability in two energy bands (without considering higher order cumulants: the bi-spectrum, tri-spectrum, etc).

Rapisarda, Ingram & van der Klis 2014 (hereafter RIK14, Chapter 2) applied systematically

and for the first time PROPFLUC on the BHB MAXI J1543-564 fitting single hump power spectra in a single energy band. RIKK16 then applied PROPFLUC on the BHB MAXI J1659-152 using for the first time the hypothesis of fluctuations stirred up in and propagating from the disc (Chapter 3). They fitted simultaneously power spectra in two energy bands and cross-spectra between these two bands. RIK17 further updated PROPFLUC introducing the hypothesis of extra variability in the hot flow, damping, and different propagation speeds of the fluctuations (Chapter 4). Veledina (2016) obtained multi-hump power spectra considering a slightly different model. The multi-hump shape of the noise is the result of interference between two variable spectral components: Compton up-scattered disc photons and synchrotron, hot flow, photons. The variability is triggered by mass accretion rate fluctuations propagating from the disc through a hot flow.
RIK17 used PROPFLUC to study two observations of the BH XTE J1550-564. Their analysis showed qualitative as well as quantitative differences between data and model predictions. These discrepancies represent an important challenge for the propagating fluctuations scenario. RIK17 speculated that the process generating the QPO may also influence the broad band noise. In this case, the observed variability is not only due to propagating fluctuations and any PROPFLUC fit of the power spectrum in two energy bands and of the phase lag between these two bands, would be biased. Here, in order to further explore this possibility and, more in general, the validity of the propagating fluctuations model, we apply PROPFLUC to selected Cygnus X-1 observations (that in general do not show QPOs). Because we want to test PROPFLUC on the broadest variety of observational states and to compare our results with previous analyses, we used the same soft state observation as that selected by AU06, and a hard state observation showing an energy spectrum that is very similar to one of the XTE J1550-564 observations analyzed by RIK17. We also selected a third observation in the transition from soft to hard state.
In Sec. 5.2 we report the main characteristics of Cygnus X-1 relevant to this study and in Sec. 5.3 we briefly summarize the PROPFLUC model features. Sec. 5.4 and Sec. 5.5 describe data reduction and our results, respectively, and in Sec. 5.6 we discuss the results. We conclude that PROPFLUC predictions are consistent with observations during the soft and hard state, while the propagating fluctuations scenario cannot explain the variability characteristics observed during the intermediate state.

5.2 Cygnus X-1

Cygnus X-1 (Bowyer et al. 1965) is a bright ($\sim$ 0.6 Crab) persistent BHB. Up to date, it has been mostly observed in the hard state with frequent (and often very fast) transitions to the soft state (Grinberg et al. 2013). The Cygnus X-1 energy spectrum in the hard state is characterized by a non-thermal component, usually modelled with a power-law ($\Gamma \approx 1.6$) with an exponential cut-off above $\approx$ 100 keV, and a thermal component, usually modelled with a multi-temperature blackbody (Dove et al. 1998 and references therein). Compared to the

canonical LHS, the Cygnus X-1 hard state differs in the lack of QPOs. The Cygnus X-1 soft state also differs from the high-soft state (HSS) of the canonical phenomenological description of transient BHBs (e.g. Belloni 2010; Remillard & McClintock 2006). The HSS energy spectrum is dominated by thermal emission (usually modelled with a multi-temperature black body), high luminosity, and low amplitude rapid variability (fractional rms $\approx 3\%$), while in Cygnus X-1 we additionally observe a significant non-thermal power law emission and high rapid variability (fractional rms $\approx 25\%$).
In a Power x Frequency representation (the one adopted in this study), the power spectrum of the source in the hard state shows two broad humps, while in the soft state it shows a single, continuous, broad band component that can be modeled with a single power law (Axelsson et al. 2005). In general, Cygnus X-1 power spectra do not show strong QPOs, even though there is evidence of the presence of broad QPOs in many observations (Belloni et al. 1996; Cui et al. 1997).
The drastic differences associated with different states in the spectral and timing properties of Cygnus X-1 suggest very different accretion regimes in the hard and soft state. Many models have been proposed to explain the behaviour of the source, but all of them agree on the presence of two main physical components (e.g. Zdziarski et al. 2002): a geometrically thin optically thick disc (producing the thermal radiation) and an optically thin hot inner flow or corona (producing the non-thermal/Comptonized radiation). The exact geometry of the system, and the exact way these two components interact with each other in the various states, is still a matter of debate.
On May 10 1996, Cygnus X-1 started a transition from the hard to the soft state. The source remained in the soft state for about 2 months before going back to the hard state (Cui et al. 1997). Studying the variability in different energy bands, Churazov et al. (2001) found that this soft state is characterized by a soft stable multi-temperature blackbody component and a harder variable power-law component. The physical scenario suggested by these authors is an optically thin variable corona 'sandwiching" an optically thick stable disc. In this scenario mass accretion rate fluctuations originate in the corona and propagate towards the BH, producing the observed rapid variability. AU06 selected one observation in this soft state to test a Monte Carlo implementation of the mass accretion rate fluctuations model (Lyubarskii 1997; Kotov et al. 2001). They found good agreement between model predictions and data.

5.3 The PROPFLUC model (summary)

PROPFLUC (ID12, IK13) assumes a truncated disc/hot flow geometry: an optically thick geometrically thin accretion disc is truncated at a certain radius $r_{\rm o}$. Inside this radius, accretion takes place through an optically thin (opacity $\tau \sim 1$) geometrically thick hot flow. Mass accretion rate fluctuations are stirred up at each radius of both the disc and the hot flow. The fluctuations propagate towards the BH (inward-only propagation) throughout the disc/hot

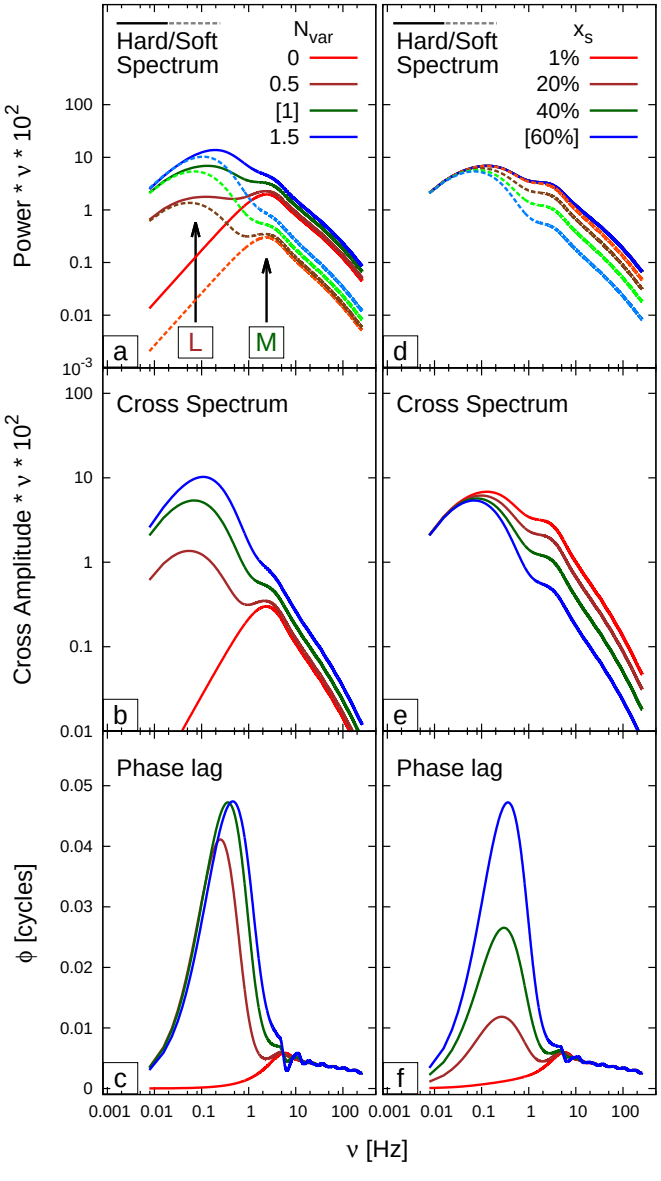

Figure 5.1: Soft (dashed line) and hard (solid line) double hump power spectra, cross-spectra, and phase lags computed varying the disc variability N_{var} and disc fraction in the soft band x_s. The double hump power spectra consist of a low-frequency and main hump (L-M configuration). Numbers in square brackets indicate the parameter value for all the other computations.

flow system. Simultaneously to the propagation of fluctuations, if the accretion flow is misaligned with the equatorial plane of the BH, the entire hot flow (but not the disc) experiences Lense-Thirring (LT) precession because of frame dragging close to the BH. This precession produces a QPO signal.

The fluctuations propagate towards the BH on the local viscous time scale. A further assumption is that the characteristic time scale of the fluctuations is (also) set by the local viscous time scale, so that the characteristic frequency of the fluctuations is the local viscous frequency. PROPFLUC assumes that, in the disc, the radial profile of the viscous frequency follows the Shakura & Sunyaev (1973) prescription ($\nu_{v,disc} \propto r^{-3/2}$, Chapter 3). In the flow, the viscous frequency is described by a smoothly-broken power law bending at the bending wave radius $r_{\rm bw}$ (ID12, IK13, Chapters 2 and 3). In PROPFLUC, at each instant in time, the total flux in a certain energy band is a linear combination of fluctuating mass accretion rate at each radius (IK13). The coefficients of this linear combination are set by the emissivity radial profile and depend on the emission mechanisms of the two accreting regions. PROPFLUC assumes multi-temperature blackbody emission in the disc (following the Shakura & Sunyaev 1973 prescription) and a power-law radial emissivity profile in the hot flow (ID12, IK13). In this way, mass accretion rate fluctuations are converted into X-ray flux variability and, because of the propagation, the variability produced at a certain radius is characterized by both fluctuations on time scales around the local viscous time scale and by longer time scale fluctuations propagated from larger radii.

Because fluctuations propagate in a finite time (the viscous time scale), PROPFLUC naturally predicts positive (hard) phase lags between a soft and a hard energy band. The amplitude (and the sign) of the lags depends on the radial dependence of the energy spectrum emitted by the accretion flow and on the selected energy bands (Chapters 3 and 4). The amplitude of the fluctuations is also expected to be a function of radius. In the disc, this dependence is assumed to be a Gaussian peaking at the boundary between disc and hot flow, the truncation radius $r_{\rm o}$ (Chapter 3). In this way, only the disc portion close to the hot flow contributes significantly to the observed variability. In the hot flow, the fluctuation amplitude can be either constant (ID12, IK13, Chapter 3), or a constant plus a narrow Gaussian peaking at the bending wave radius, $r_{\rm bw}$ (Chapter 4). In the latter case, we talk about extra variability in the hot flow. This assumption is made to take into account results from numerical simulations (Fragile & Blaes 2008; Henisey, Blaes & Fragile 2012), showing that the inner part of a tilted accretion flow may produce extra high-frequency variability.

The viscous frequency radial profile, the emissivity radial profile, and the amount of variability injected at each radius of the disc/hot flow system, together determine the shape of the power and cross-spectrum between two energy bands (AU06, Chapters 3 and 4). Constant amplitude variability stirred up and propagating only in the hot flow produces a single hump power spectrum (M configuration, Chapter 4). We also obtain a single hump power spectrum when we consider variability only from the disc (L configuration). Combining variability from the disc and from the hot flow, we obtain a double hump power spectrum (L-M configuration, Chapters 3 and 4). Considering also extra variability in the hot flow, we obtain

a three-hump power spectrum (L-M-H configuration, Chapter 4). For all the configurations, the emissivity profiles in the soft and hard energy band affect the shape of the power spectrum and the lags associated to the different humps. For example, Fig. 5.1 shows double hump (L-M configuration) power spectra, cross-spectral amplitude, and phase lags between a soft and a hard energy band. We obtained the different curves varying the amount of variability propagating from the disc (N_{var}, Fig. 5.1$a-c$) and the fraction of soft band photons emitted from the disc (x_s, Fig. 5.1$d-f$). When the variability coming from the disc tends to zero (N_{var} = 0), the double hump converges to a single hump power spectrum. When N_{var} =1 and x_s varies between 20 and 60% (Fig. 5.1$d-f$), we obtain different phase lag profiles without modifying the shape of the hard power spectrum. This means that the same hard power spectral distribution can produce very different phase lags depending on the energy spectral properties of the source.
The PROPFLUC parameters regulate the viscous frequency profile, the amplitude of the variability, and the emissivity profiles in the disc/hot flow. Tab. 1 in RIK17 shows a brief description of the PROPFLUC parameters. From spectral fitting and flux measurements it is possible to estimate the maximum temperature in the disc T_{max} and the disc fraction in the soft band x_s. These two parameters and the hardness ratio HR together set the emissivity of the disc. The model also accounts for damping of the fluctuations as they propagate and for the propagation speed diverging from the value predicted by the local viscous frequency (parameters D and x_{lag}, respectively, see RIK17). Because PROPFLUC does not include a physical model for QPO modulation, the QPO is assumed to be a Lorentzian. The frequency of the QPO is a weighted radial average of the point particle Lense-Thirring precession frequencies in the hot flow (Liu & Melia 2002; ID12, eq. 1). The QPO characteristics (amplitude, coherence, and phase lag) are *ad hoc* parameters.

5.4 Observations and data analysis

We analyzed data from the Proportional Counter Array (PCA; Jahoda et al. 1996) on board of the *Rossi X-ray Timing Explorer* (RXTE). We used 3 pointed observations: 1) 2 February 1997 (obs. ID 10238-01-03-00, MJD 50482, hard state), 2) 12 August 1996 (obs. ID 10412-01-07-00, MJD 50307, transition from soft to hard state), and 3) 18 June 1996 (obs. ID 10512-01-09-01, MJD 50252, soft state). The three observations contain $\sim$ 3.5, 2.1 and 2.4 ks of data, respectively.
We performed spectral analysis using HEASOFT 6.13. We used Standard2 data (16s time resolution) to extract source and background spectra. For the three analyzed spectra, we created a PCA response matrix, we corrected the energy spectra for background, and we applied a systematic error of 1%. We fitted the energy spectra in the 3-20 keV energy band using XSPEC 12.8.2 (Arnaud 1996) with the abundances of Wilms et al. (2000).
As noted by Wilson & Done (2001), the energy spectrum of the first observation is very

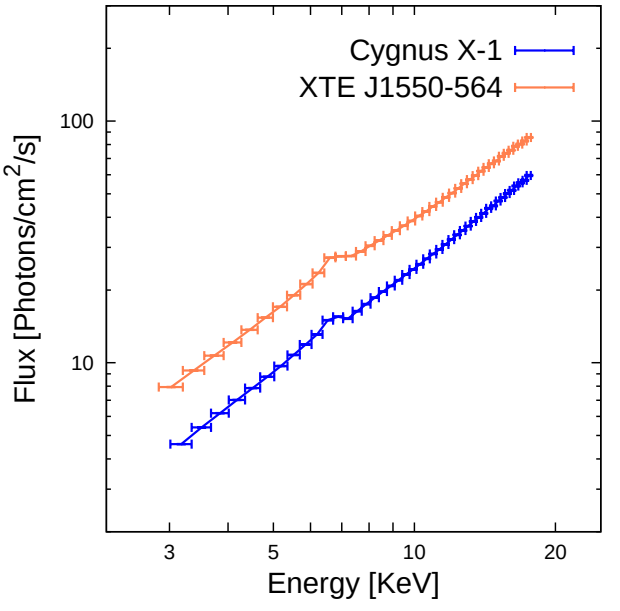

Figure 5.2: Unfolded energy spectrum of Cygnus X-1 (blue line) and XTE J1550-564 (orange line) in the LHS. These two observations are characterized by a very similar energy spectrum.

similar to the spectrum of XTE J1550-564 in the LHS at the beginning of the 1998-1999 outburst. Specifically, there is an evident similarity between the energy spectrum of the first observation and the observation 30188-06-01-01 of XTE J1550-564 (see Fig. 5.2). The latter was selected by RIK17 for testing PROPFLUC. For comparison purposes, we used the same spectral model as that adopted by RIK17 (following Axelsson et al. 2013) for fitting the first observation: TBABSxGABSx(DISKBB+NTHCOMP+RFXCONVxNTHCOMP) (Mitsuda et al. 1984; Zdiarski et al. 1996; Życki et al. 1999; Kolehmainen et al. 2001). We varied the DISKBB normalization, the NTHCOMP spectral index and normalization, the amount of reflection R, we used an inclination of 50°(Sowers et al. 1998), and we fixed all the other model parameters to the best-fit parameters found by Axelsson et al. (2013). We obtained a χ^2_{red} = 0.95 with 38 degrees of freedom. For the second and third observation, we used the model TBABSx(GAUSSIAN+DISKBB+NTHCOMP) (Mitsuda et al. 1984; Życki et al. 1999) obtaining a χ^2_{red} = 0.45 and 0.96 with 36 degrees of freedom, respectively. From our spectral fits we obtained the disc contribution to the soft band x_s and the maximum temperature in the disc $T_{d,max}$ for each of the selected observations. We emphasize that the goal of our spectral fitting is estimating $T_{d,max}$ and x_s (two parameters necessary for PROPFLUC fits), and not to perform a detailed spectral analysis.

For all our observations, we selected the same two energy bands as RIK17: 1.9 - 13.0 keV (soft) and 13.4-20.3 keV (hard). Source and background light curves were extracted from these bands. We computed the count ratio between hard and soft band (i.e. the hardness ratio HR, another information necessary for PROPFLUC fitting) from the background subtracted light curves of each observation.
For all the observations, we combined Single Bit mode (time resolution $\approx$ 125 μs) and Event mode (time resolution $\approx$ 62 and 16 μs for observations 1-2 and 3, respectively) to perform Fourier timing analysis. Leahy-normalized power spectra were computed in the soft and hard band using a time resolution of 1/8192 s and 128 s data segments. This gives a frequency resolution of 1/128 $\approx$ 0.008 Hz and a Nyquist frequency of 4096 Hz. Using the same setting, we computed cross-spectra between soft and hard band. We averaged power and cross-spectra, subtracted the Poisson noise, and applied fractional rms normalization following RIKK16 (Chapter 3).

5.5 Results

We jointly fitted logarithmically binned soft and hard power spectra, and cross-spectra between the two bands with the propagating mass accretion rate fluctuations model PROPFLUC (IK13, Chapters 3 and 4). We used the same resolution for data and model and we fitted data up to 70 Hz. For the first (hard state) and second (intermediate state) observation, we used a double hump power spectrum (L-M configuration). This is obtained combining mass accretion rate fluctuations stirred up in and propagating through the disc and the hot flow. In this configuration, the physical properties of the accretion flow vary sharply at the truncation radius $r_{\rm o}$ and this leads to two different humps in the power spectrum (see Sec. 5.3). For the third (soft state) observation, we fitted the data using only a main hump power spectrum. This can be obtained considering mass accretion rate fluctuations generated in and propagating through a single region (so without abrupt variations in viscous frequency, emissivity radial profile, etc). This single region can be either the hot flow (M configuration) or the disc (L configuration). For all the fits we considered a 10 $M_{\odot}$ BH with dimensionless spin parameter $a_* = 0.5$. We used N_{dec} = 35 rings per radial decade, and the fixed hydrogen column density (n_H = 0.6 $\times$ 10^{22} cm^{-2}, Balucinska-Church et al. 1995).
Fig. 5.3-5.5 show soft and hard power spectrum (a), cross-spectral amplitude (b), phase lag (c), and coherence (d) between these two bands for the three observations we analyzed. Fig. 5.6 shows the PROPFLUC best fit of the first and third observation. The best-fit parameters are listed in Tab. 5.1.

5.5.1 First (hard state) observation: 10238-01-03-00

This hard state observation is characterized by a double hump power spectrum: a low-frequency hump peaking at $\approx$ 0.1 Hz and a high-frequency hump peaking at $\approx$ 3 Hz (Fig.

Table 5.1: PROPFLUC best fit parameters to the first and third observation. The first observation was fitted using the low-frequency and main hump (L-M) and the third observation using only the main hump (M). The subscripts s and h correspond to soft and hard band respectively. The symbol (f) means that the parameter is fixed. The symbol - means that the parameter was not used in the fit.

Observation	(soft state) 10512-01-09-01	(hard state) 10238-01-03-00
Humps	M	L-M
Σ_0	6.48	45.43
$F_{var}[\%]$	41.69	89.96
ζ	1.1	–
λ	0.9	5.8
κ	30.0	19.1
r_i	4.50	4.50
r_{bw}	2.87	10.02
r_o	2489	10.02
γ_s	9.22	5.34
γ_h	14.62	5.91
$(\Delta\gamma)$	5.41	0.58
N_{var}	–	0.66
Δd	–	51.75
$\nu_{v,max}[Hz]$	–	0.43
$T_{d,max}$ [keV]	0.58(f)	0.58(f)
x_s	0.23	0.03(f)
D	1.6	1.0
x_{lag}	1.2	1.1
$M[M_\odot]$	10.0(f)	10.0(f)
a_*	0.5(f)	0.5(f)
$n_H[10^{22}cm^{-2}]$	0.6(f)	0.6(f)
χ^2_{red}	1.31	1.34
dof	352.00	350.00

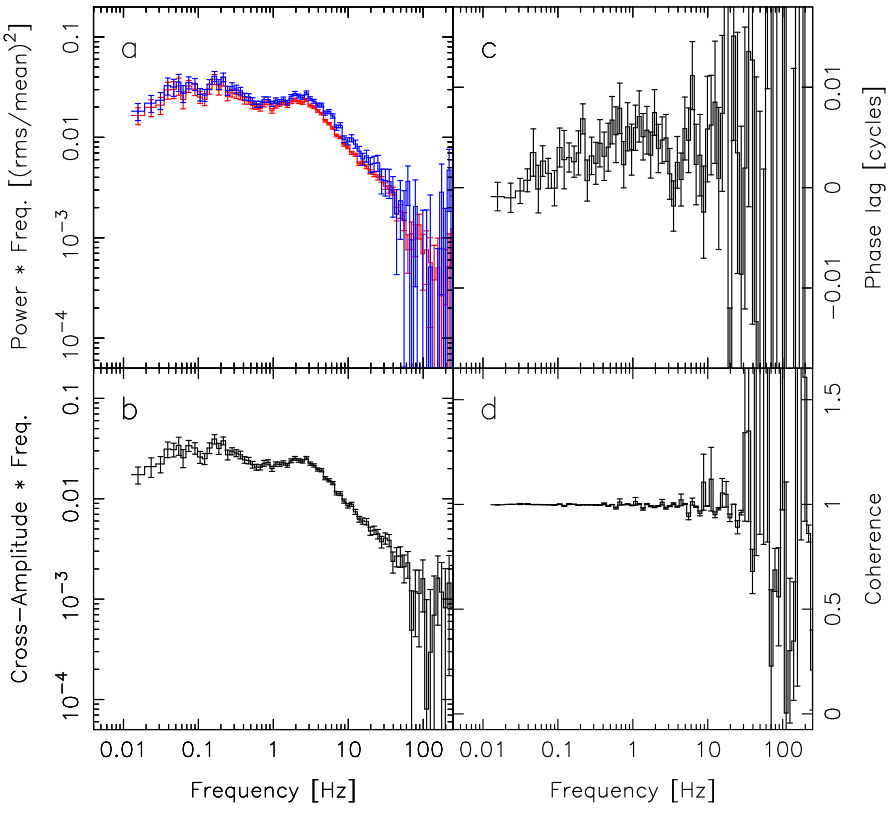

Figure 5.3: Hard (blue line) and soft (red line) power spectrum (a), cross-spectrum amplitude (b), phase lag (c), and intrinsic coherence (d) of the first observation (10238-01-03-00).

5.3a). Hard and soft power have a very similar shape, even if the hard fractional variability is slightly larger at higher frequencies (above $\approx$ 1 Hz). The maximum amplitude of the lags is $\approx$ 0.005 cycles at $\approx$ 1 Hz (Fig. 5.3c) and the coherence is $\approx$ 1 up to $\approx$ 10 Hz (Fig. 5.3d). We fitted the observation using the L-M configuration (low-frequency and main hump) obtaining a reasonable fit (χ^2/dof = 444.80/350 $\approx$ 1.3, Fig. 5.6 and Tab. 5.1). Because of the small disc contribution to the soft band ($x_s \approx 3$ %), the L-M configuration predicts very small phase lags, consistent with the data (Fig. 5.6).

5.5.2 Second (intermediate) observation: 10412-01-07-00

This observation covers part of the transition from soft to hard state in 1996 (Cui et al. 1997). Up to $\approx$ 0.5 Hz, soft and hard power show similar shape and normalization (Fig. 5.4a). Above this frequency, soft and hard power show evident differences. In particular, the soft power is characterized by a single hump peaking at $\approx$ 2 Hz. The hard power shows a narrow

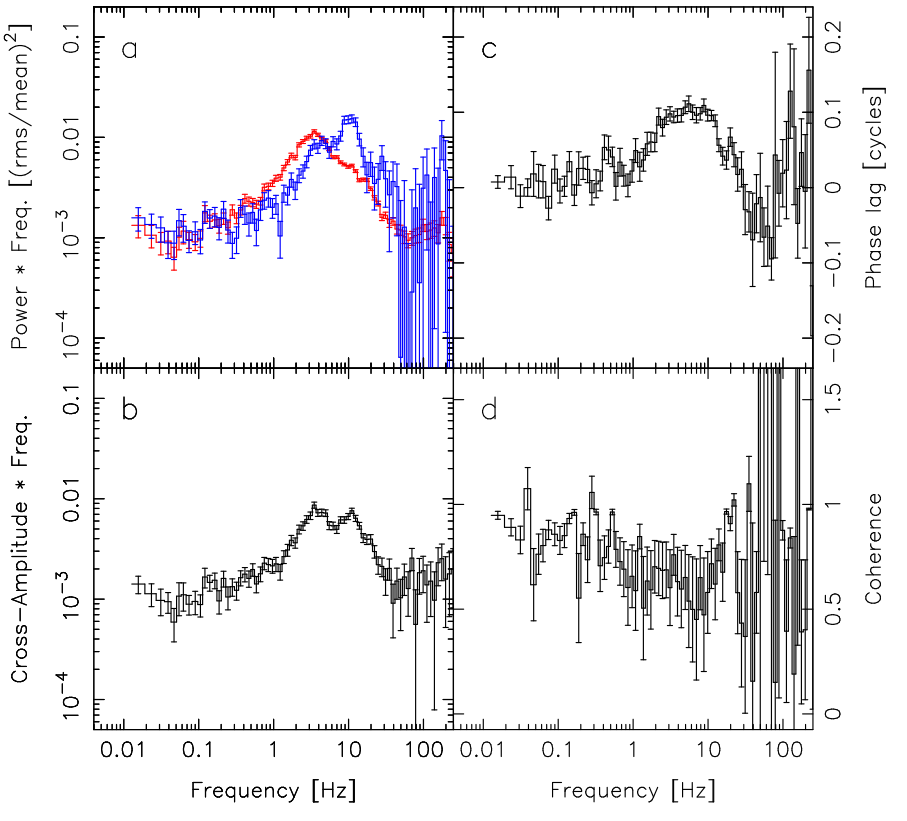

Figure 5.4: Hard (blue line) and soft (red line) power power spectrum (a), cross-spectrum amplitude (b), phase lag (c), and intrinsic coherence (d) of the second observation (10412-01-07-00).

5

feature (QPO) at ≈ 10 Hz on top of a single hump. The single hump in the hard band peaks at higher frequency than in the soft band (≈ 3-5 Hz). In the soft band we do not observe any QPO. The phase lag spectrum is characterized by a "bump" peaking at ≈ 6 Hz with amplitude ≈ 0.1 cycles (20 times higher than in the previous observation, see Fig. 5.4*c*). The coherence also clearly differs from the previous observation (Fig. 5.4*d*): it decreases to ≈ 0.5 around 7 Hz.

We attempted to fit this observation using the L-M configuration, but we did not get a statistically acceptable result. More specifically, the model does not predict the observed bump in the phase lags (≈ 0.1 cycles). Because of the complex shape of the power spectrum (multiple hump power spectrum), we could not obtain an acceptable fit with either the M or L configuration.

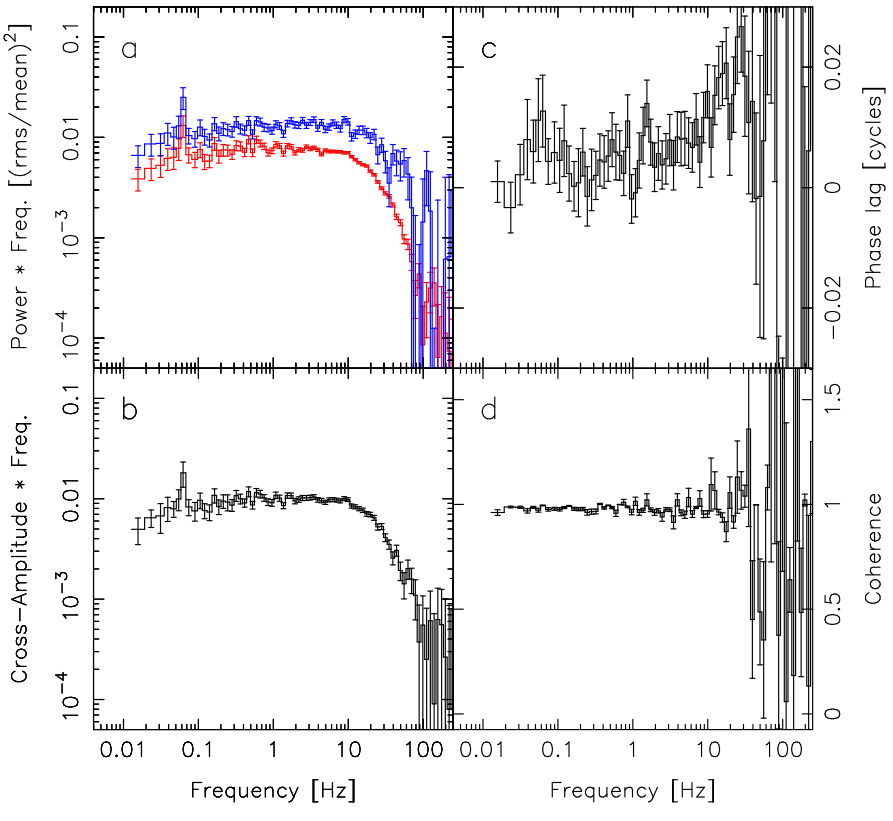

Figure 5.5: Hard (blue line) and soft (red line) power spectrum (a), cross-spectrum amplitude(b), phase lag (c), and intrinsic coherence (d) of the third observation (10512-01-09-01).

5.5.3 Third (soft state) observation: 10512-01-09-01

This soft state observation is characterized by $\sim 1/f$ continuous noise (flicker noise, flat shape in the $\nu P(\nu)$ representation) between ≈ 0.1 and 10 Hz in both the soft and the hard energy band (Fig. 5.5a). Above 10 Hz, the power decreases steeply with frequency. Below 0.1 Hz the power decreases slightly in both the energy bands. In general, hard and soft power have a very similar shape, but different normalizations, with more fractional variability in the hard band at all frequencies. The amplitude of the lags gradually increases with frequency (Fig. 5.5c), up to ≈ 0.02 cycles above 1 Hz. The coherence is ≈ 1 up to ≈ 10 Hz (Fig. 5.5d). This observation also shows a highly coherent, and significant ($> 3\sigma$), QPO at ≈ 0.06 Hz (quality factor Q ≈ 38 in both hard and soft band). This feature is characterized by a hard lag of $0.031^{+0.010}_{-0.003}$ [cycles]. We note that the predicted phase lag at ≈ 0.06 Hz (Fig. 5.6, red line) is slightly smaller than the best-fit value of the QPO lag. This difference is because, in the PROPFLUC prescription, the QPO signal is added to the broad band noise and this noise

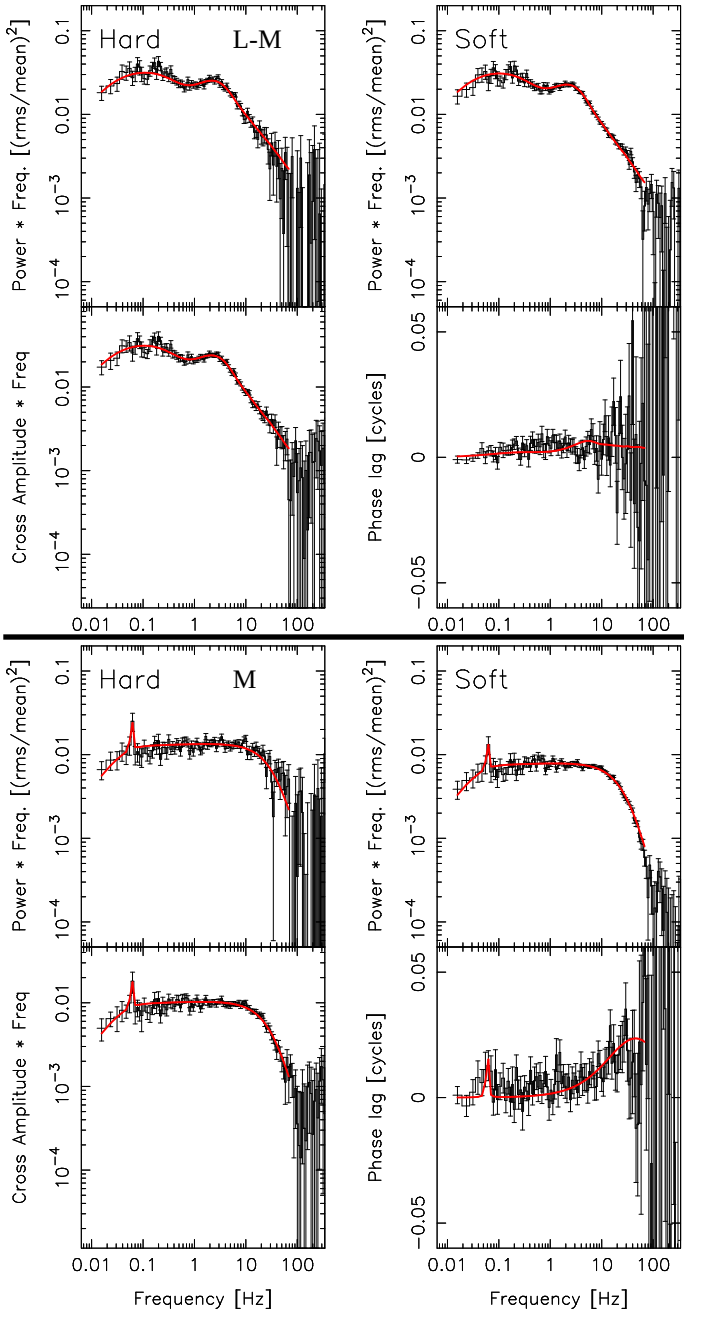

Figure 5.6: Best fit of the first (top) and third (bottom) observation (solid red line) different hump configurations: only main (M) and low-frequency and main (L-M).

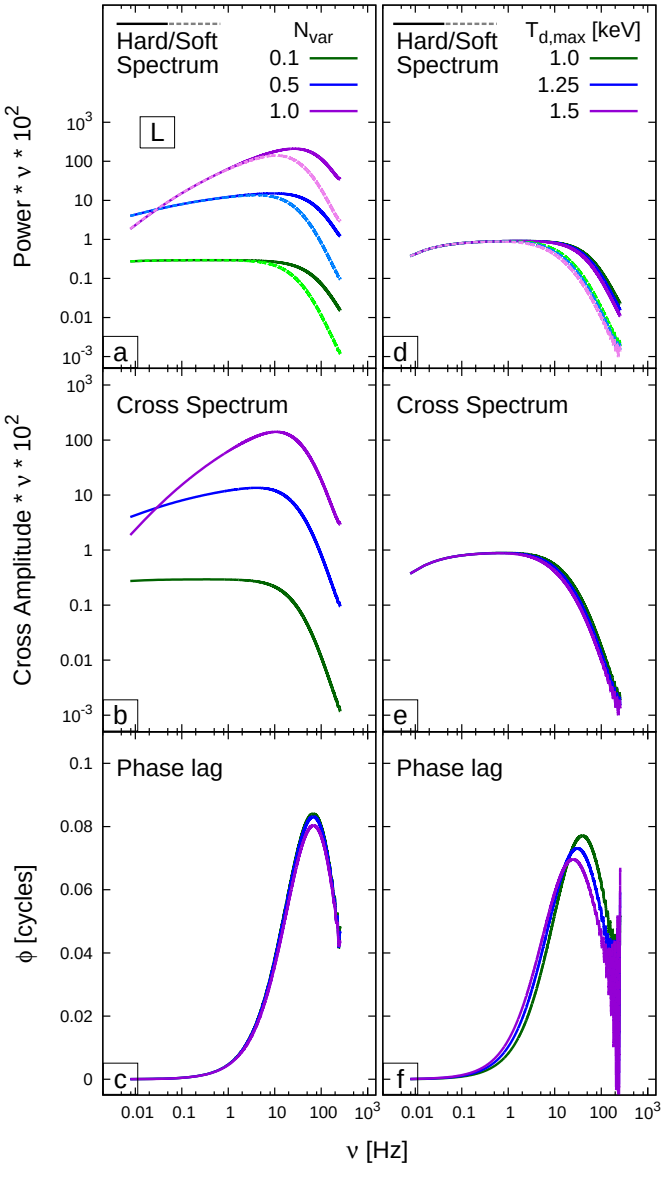

Figure 5.7: Soft (dashed line) and hard (solid line) single hump power spectrum, cross spectra, and phase lags computed varying the disc variability N_{var} and the maximum temperature in the disc $T_{d,max}$. In these computations, the single hump power spectrum is due to mass accretion rate fluctuations stirred up in and propagating only in the disc (L configuration).

dilutes the phase lag purely due to the QPO signal. Since the QPO does not follow any of the defining properties of canonical low-frequency QPO classifications (e.g. Casella et al. 2005), we do not tie its frequency to the LT precession frequency, choosing instead to simply model the feature with a Lorentzian.
We fitted this observation using both the L and M configuration (single hump power spectrum). With the L configuration (only disc variability), we did not obtain an acceptable fit. Even though it is possible to reproduce the shape of the power in one of the two bands in this configuration, we could not reproduce the difference in normalization between hard and soft band. Fig. 5.7 generically demonstrates that the L configuration produces hard and soft power spectra with the same normalization below $\approx$ 10 Hz, contrary to what we observe in the data (Fig. 5.5a). Furthermore, the predicted amplitude of the phase lag in this configuration ($\approx$ 0.08 cycles) is larger than the data ($\approx$ 0.02 cycles). The M configuration, with the disc contribution in the soft band x_s set as a free parameter, produced a better result. We obtained a reasonable fit (χ^2/dof = 462/352 $\approx$ 1.3, Fig. 5.6 and Tab. 5.1) with $x_s \approx 23\%$ (consequently, x_h, the fraction of hard photons contributed by the disc, is smaller than 1%[1]). In this case (like in the L configuration), there is only one varying component (the hot flow), but the hot flow emission in the soft band is diluted by non-variable disc emission.
The shape of the observed power spectrum can also be reproduced using the L-M configuration. In this configuration, the power spectrum at low frequency constrains the radial extension of the varying disc, Δd, instead of the truncation radius, $r_{\rm o}$ (as it was in the M configuration). Using a double hump we did not obtain any significant improvement to the fit. This is because the model underestimates the power spectrum in the hard band at frequencies corresponding to the low-frequency hump (the one due to disc variability). The model also predicts extra phase lags associated with the low-frequency hump that are not observed in the data.

5.6 Discussion

We applied the propagating fluctuations model PROPFLUC to three observations of Cygnus X-1. We jointly fitted power spectra in two energy bands and the cross-spectrum between these bands. The observations were selected in order to test PROPFLUC on a broad variety of states (hard state, soft state, and transition between the two) and to compare our analysis with previous results from AU06 and Chapter 4. Our fits were intended to explore the general agreement between propagating fluctuations model predictions and data; for this reason we did not compute the errors on the best-fit parameters. However, encouraged by the statistically reasonable fits we obtained on the first and third observation, we speculate about the possible

[1]Since the observed hardness ratio, HR, and the PCA response matrix are model inputs, the fraction of hard band emission contributed by the disc component (x_h) is calculated self-consistently within the model from the disc temperature parameter $T_{d,max}$ (i.e. we assume a multi-temperature blackbody disc spectrum, convolve with the instrument response and calculate x_h from x_s, HR, and the folded disc model in the hard and soft bands). See RIKK16 for futher details

geometry of the accreting system suggested by our best-fit values.

5.6.1 First observation

In the first observation the source is in the hard state (Gilfanov et al. 1999). We obtained a reasonable fit using the L-M configuration ($\chi^2/dof \approx 1.3$). This configuration assumes a truncated disc geometry with the hot flow extending radially inside of the disc inner edge. Variability is generated in the region of the disc closest to the truncation radius, and also throughout the inner hot flow (see Chapters 3 and 4). From our fit, we estimate a truncation radius of $\approx 10\ R_{\rm g}$, with the amplitude of fluctuations generated in the disc peaking at the truncation radius and dropping off following a Gaussian profile with width of $\Delta d \approx 52\ R_{\rm g}$. While it is possible to obtain an acceptable fit in this configuration, we cannot exclude that part of the disc is sandwiched by the hot flow (see Sec. 5.6.3). We did not test this scenario and in all our considerations in this section we assume the simple truncated disc geometry.

Our model parameterises the radial surface density profile, and, via mass conservation, the radial dependence of the viscous frequency, with a smoothly broken power-law function. The break radius of this function is assumed to occur at the so-called bending wave radius, which, for a tilted accretion flow, marks the point inside of which the pressure waves that couple the flow (bending waves) cause an oscillatory structure of the tilt angle (Lubow et al. 2002; Fragile et al. 2007; Ingram, Done & Fragile 2009). This radius is given by $r_{bw} \sim 3(H/R)^{-4/5}a_*^{2/5}$, where H/R is the scaleheight of the hot flow and a_* is the dimensionless spin parameter of the BH. In our best-fit model, the bending wave radius $r_{\rm bw}$ is smaller than the hot flow inner radius $r_{\rm i}$, meaning that the viscous frequency is parameterised by a single power-law with no break. Taking this at face value and assuming that the hot flow is indeed tilted as per the Ingram et al. (2009) model, this implies *either* that $r_{\rm bw} < r_{\rm i}$ or $r_{\rm bw} > r_{\rm o}$. This is because of the inherent degeneracy in our parameterisation: the single power-law parameterising the viscous frequency in our best fitting model could be the power-law index appropriate for $r >> r_{\rm bw}$, or the index appropriate for $r << r_{\rm bw}$. From the formula for $r_{\rm bw}$, and assuming a spin value of $a_* = 0.5$, this implies either that $H/R < 0.16$ or $H/R > 0.43$. Alternatively, the single power law obtained from the fit could result from the BH spin axis of Cygnus X-1 being aligned with the inner accretion disc and therefore probably with the binary rotation axis. In this case, the model predicts no break in the surface density profile, and also, there would be no LT precession of the hot flow. This could explain why Type-C QPOs (see Casella et al. 2005 for a description of QPO types) are not observed in Cygnus X-1, assuming the Type-C QPOs observed in other sources result from LT precession.

We note that Axelsson et al. (2005) present evidence that Type-C QPOs may in fact be present in Cygnus X-1, but with unusually low rms and quality factor (see fig. 17 therein). Perhaps, therefore, the tilt angle is merely small in this source rather than zero.

As already mentioned in Sec. 5.4, the energy spectrum of our observation 1 is very similar to that in the first of the XTE J1550-564 observations analyzed in Chapter 4 (see Fig. 5.2). Comparing these two observations, we note that their timing properties are very different

(see Fig. 5.8). The XTE J1550-564 power spectrum is dominated by a strong QPO, while in Cygnus X-1 we do not observe any sharp feature. Both sources show a double hump power spectrum, but the two have rather different characteristics. In XTE J1550-564 both the humps peak at higher frequency, have a smaller amplitude, and a different shape compared to the Cygnus X-1 humps up to $\approx$ 10 Hz. The XTE J1550-564 phase lag profile shows a clear "bump" at $\approx$ 5 Hz, while in the third Cygnus X-1 observation the phase lags are very small (Fig. 5.8*c*). In the propagating fluctuations scenario, the amplitude of the phase lag depends mainly on the emissivity profile in the soft and hard energy bands. These emissivity profiles also affect the shape of the power spectrum, so that similar power spectral shapes in the soft and hard band require similar emissivity profiles in the two bands. If the emissivity indices in two energy bands are equal, the phase lag between these bands is zero. In the XTE J1550-564 observation shown here, the soft and hard power shapes are too similar to produce the observed phase lag "bump" at $\approx$ 5 Hz. This discrepancy can be related to either wrong assumptions in the propagating fluctuations model, or some additional physical mechanism producing variability and not considered in PROPFLUC. In the Cygnus X-1 case, the soft and hard power are also very similar, but the observed phase lags are small enough to be consistent with the model predictions. Since the model seems to work very well for this Cygnus X-1 observation, but very poorly for the XTE J1550-564 observation with a very similar spectrum but with a strong QPO not observed for Cygnus X-1, it seems reasonable to speculate that the misalignment driving the QPO in XTE J1550-564 is also influencing the broad band noise in that source in a manner that our model does not capture. Additional variability stirred up by a mechanism associated with misalignment and not associated with the propagating fluctuations can lead to an incorrect estimate of the emissivities and, consequently, to a different phase lag profile.

It is not unreasonable to consider a difference in alignment between BHs in low mass X-ray binaries (LMXBs) and Cygnus X-1, which has a high mass companion. In a LMXB, a BH initially misaligned at birth will align over a timescale comparable to the accretion lifetime (Fragile et al. 2001; Martin, Tout & Pringle 2008; King & Nixon 2016), suggesting that misalignment is common in LMXBs. The alignment timescale is inversely proportional to the long term mass accretion rate (Fragile et al. 2001), which is difficult to ascertain in LMXB BH transients from the few decades of observations of these systems so far. It may have been be higher, and the alignment time scale correspondingly shorter, in Cygnus X-1 which is a persistent X-ray source with accretion driven at least in part by the OB star stellar wind (Gies et al. 2003 and references therein). It is doubtful, however, if the mass accreted during the life time of Cygnus X-1, which is limited by the lifetime of the OB donor star, could have been sufficient to align an initially strongly misaligned BH.

Another possibility is that the BH spin has always been close to alignment with the binary rotation axis. Asymmetries in the supernova explosion preceding a BH formation can significantly change the orientation of the progenitor spin axis (that is assumed to be equal to the binary rotation axis) and impart a kick to the binary system that affects its proper motion (e.g. Repetto et al. 2012). The proper motion of Cygnus X-1 does not deviate significantly

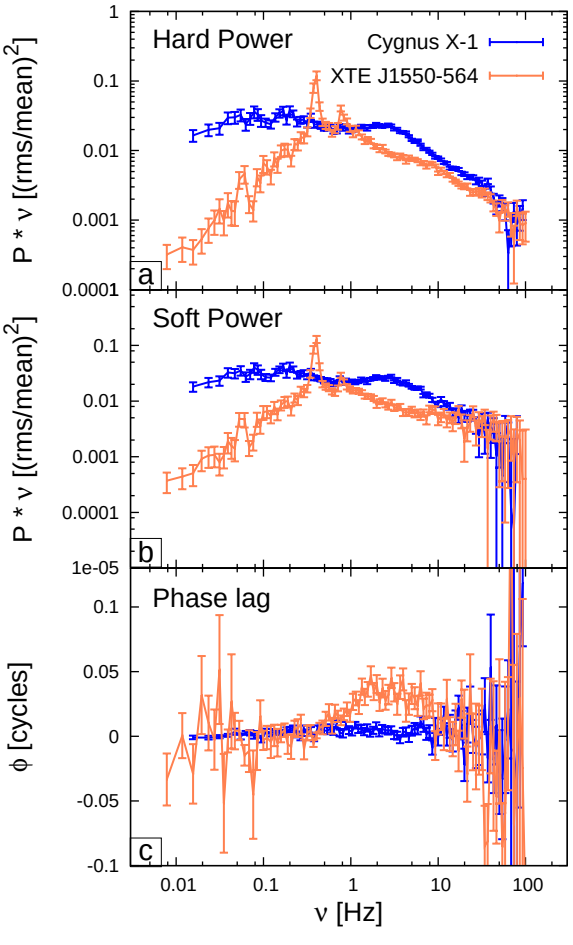

Figure 5.8: Hard power spectrum (a), soft power spectrum (b), and Phase lag (c) between this two energy bands of Cygnus X-1 (blue line) and XTE J1550-564 (orange line) in the hard state. Even if the these two observations are characterized by a very similar energy spectrum, their timing properties are very different.

from the motion of the massive star association Cygnus OB3 that it belongs to (Mirabel & Rodrigues 2002), supporting a formation scenario that does not involve an asymmetric supernova explosion. In this case, the initial BH spin would have already been near-aligned with the binary rotation axis. However, there is also some evidence of misalignment in Cygnus X-1, since reflection spectroscopy implies that the inner disc has a different inclination angle to the binary system (Tomsick et al. 2014). Possibly the exceptional "focused wind/atmosphere Roche lobe overflow" accretion geometry in Cygnus X-1 allows for the inner disc to align with the BH spin even when the binary rotation axis is not.

5.6.2 Second observation

The second observation covers part of the transition from soft to hard state. Because of the complex shape of the power spectrum, we attempted to fit this observation with a double hump power spectrum (L-M configuration). For this observation we could not get a statistically acceptable fit with PROPFLUC. The model does not predict the large phase lags between ≈ 0.5 and 11 Hz.

5.6.3 Third observation

In the third observation the source is in the soft state (Cui et al. 1997). AU06 successfully applied a Monte Carlo mass accretion rate fluctuations model to this observation. They fitted the ratio between power in a hard and soft band (so they did not predict the shape of the two individual power spectra) and the phase lag between those two bands. In our analysis we fitted simultaneously the soft and hard power spectrum, and also the cross-spectrum (so both phase lags and coherence) between the two bands. We obtained a reasonable fit using the M configuration ($\chi^2/dof \approx 1.3$), i.e. considering fluctuations stirred up and propagating only in the hot flow. In computing the Fourier products, we considered longer time segments than those used by AU06 (128s as opposed to 32s), extending the frequency range down to ≈ 0.01 Hz. The shape of the power spectrum between ≈ 0.01 and 0.1 Hz allowed us to constrain the outer edge of the variable region ($r_{\rm o} \approx 2500\ R_{\rm g}$) and to reveal a very low frequency QPO, which does not fit into any of the canonical low-frequency QPO classifications (Casella et al. 2005). The best-fit bending wave radius is again smaller than the inner radius, meaning that the viscous frequency in the hot flow is described by a single power-law, as in our fit to observation 1.

In our fit, no variability is generated in the disc itself ($N_{\rm var} = 0$), and the fraction of soft band emission contributed by the disc component (x_s) is a free parameter. This allows the model to reproduce the difference in normalization between the observed soft and hard power spectra, whilst preserving their almost identical shapes: the stable disc component dilutes the variable flow component more in the soft band than in the hard band (because $x_s > x_h$). Fig. 5.7(d) demonstrates that this dilution is required: considering only emission from a single propagating region (either hot flow or disc) leads to identical soft and hard power spectra up to ≈ 10 Hz, at odds with the observations. Moreover, the fit requires *more* dilution in the soft band than in the hard band; i.e. the stable component is soft. Therefore an alternative model with a variable disc and stable flow will not work. This agrees with Churazov et al. (2001), who constrained stable and variable spectral components of Cygnus X-1 for a 1996 soft state observation. They found that the stable component was in the shape of a disc spectrum, which is consistent with what we find here by requiring more dilution in the soft band than in the hard band.

Since we measure an enormous outer radius for the flow ($r_{\rm o} \approx 2500 R_g$) but the spectrum

clearly requires a strong disc component (requiring a disc inner radius close to the BH, as fitted by Gierlinski et al. 1999), this observation is very much at odds with a truncted disc / hot inner flow geometry. Our fit instead points to a sandwich geometry, in which a stable disc is sandwiched above and below by a variable hot flow / corona, which extends up to large radii and gives rise to the observed rapid variability. This geometry was already suggested by Churazov et al. (2001). Such a geometry implies there must be very strong reflection features in the spectrum, since the covering factor of a sandwich corona is very high. This is consistent with the reflection covering factor of $\Omega/(2\pi)$ =0.7 estimated from the spectral fit of this observation performed by Gierlinski et al. (1999). However, we note that our best-fit value of x_s (23%) is smaller than the one deduced from spectral fitting ($x_s \approx 60\%$). This suggests that the disc emission is not entirely stable, with the variability amplitude in the disc following the same radial dependence of variability amplitude as the corona sandwiching it, but with a lower normalisation.

5.7 Conclusions

Using the propagating fluctuations model PROPFLUC we fitted a soft and a hard state observation of Cygnus X-1. Our analysis suggests a truncated disc geometry in the hard state, with mass accretion rate fluctuations generated in and propagating through both disc and hot flow. The viscous frequency in the hot flow is described by a single power law. This, together with the lack of a type-C QPO, may result because of the alignment of the black hole spin axis with the inner disc and presumably with the binary rotation axis.

The energy spectrum of this hard state observation is very similar to a hard state observation of XTE J1550-564 analyzed with PROPFLUC in Chapter 4. However, the two observations show very different timing properties, in particular, the XTE J1550-564 power spectrum is dominated by a strong QPO and show an unexplained broad phase lag feature around 5 Hz suggesting that an additional mechanism is at work. In Chapter 4 we could not obtain an acceptable fit on this observation with PROPFLUC and they speculated that the mechanism producing the QPO may also affect the broad band noise in a more complex way than what described in the PROPFLUC scenario. The fact that in Cygnus X-1 (that does not show type-C QPOs) we obtained an acceptable fit with PROPFLUC, strengthens this speculation, suggesting that misalignment may be the common cause of both the strong QPO, and the additional variability in XTE J1550-564.

We also obtained an acceptable fit for the soft state observation. In this case we considered fluctuations propagating only in the hot flow with the variable emission diluted by a stable (soft) disc emission. This result, together with more detailed spectral analysis from previous studies (Gierlinski et al. 1999), suggests a sandwich geometry, where the variable hot flow sandwiches a stable disc. PROPFLUC is not designed to properly fit this kind of geometry, however we plan to investigate such configuration in future works.

Bibliography

Altamirano D., Strohmayer T., 2012, ApJ, 754, L23

Arévalo P., Uttley P., 2006, MNRAS, 367, 801

Armitage P. J., Reynolds C. S., 2003, MNRAS, 341, 1041

Arnaud K. A., 1996, in Astronomical Society of the Pacific Conference Series, Vol. 101, Astronomical Data Analysis Software and Systems V, Jacoby G. H., Barnes J., eds., p. 17

Asplund M., Grevesse N., Sauval A. J., Scott P., 2009, ARA&A, 47, 481

Axelsson M., Borgonovo L., Larsson S., 2005, A&A, 438, 999

Axelsson M., Hjalmarsdotter L., Done C., 2013, MNRAS, 431, 1987

Balbus S. A., Hawley J. F., 1998, Reviews of Modern Physics, 70, 1

Balucinska-Church M., Belloni T., Church M. J., Hasinger G., 1995, A&A, 302, L5

Balucinska-Church M., McCammon D., 1992, ApJ, 400, 699

Belloni T., Homan J., Casella P., van der Klis M., Nespoli E., Lewin W. H. G., Miller J. M., Méndez M., 2005, A&A, 440, 207

Belloni T., Méndez M., King A. R., van der Klis M., van Paradijs J., 1997a, ApJ, 488, L109

Belloni T., Mendez M., van der Klis M., Hasinger G., Lewin W. H. G., van Paradijs J., 1996, ApJ, 472, L107

Belloni T., Psaltis D., van der Klis M., 2002, ApJ, 572, 392

Belloni T., van der Klis M., Lewin W. H. G., van Paradijs J., Dotani T., Mitsuda K., Miyamoto S., 1997b, A&A, 322, 857

Belloni T. M., 2010, in Lecture Notes in Physics, Berlin Springer Verlag, Vol. 794, Lecture Notes in Physics, Berlin Springer Verlag, Belloni T., ed., p. 53

Böttcher M., Liang E. P., 1999, ApJ, 511, L37

Bowyer S., Byram E. T., Chubb T. A., Friedman H., 1965, in IAU Symposium, Vol. 23, Astronomical Observations from Space Vehicles, Steinberg J.-L., ed., p. 227

Bradt H. V., Rothschild R. E., Swank J. H., 1993, A&AS, 97, 355

Burrows D. N. et al., 2005, Space Sci. Rev., 120, 165
Campana S., Stella L., 1995, MNRAS, 272, 585
Casella P., Belloni T., Stella L., 2005, ApJ, 629, 403
Churazov E., Gilfanov M., Revnivtsev M., 2001, MNRAS, 321, 759
Cui W., Zhang S. N., Chen W., Morgan E. H., 1999, ApJ, 512, L43
Cui W., Zhang S. N., Focke W., Swank J. H., 1997, ApJ, 484, 383
Dexter J., Fragile P. C., 2011, ApJ, 730, 36
Done C., 2010, ArXiv e-prints
Done C., Gierliński M., Kubota A., 2007, A&A Rev., 15, 1
Dove J. B., Wilms J., Nowak M. A., Vaughan B. A., Begelman M. C., 1998, MNRAS, 298, 729
Ebisawa K. et al., 1994, PASJ, 46, 375
Esin A. A., McClintock J. E., Narayan R., 1997, ApJ, 489, 865
Evans P. A. et al., 2007, A&A, 469, 379
Fender R., Belloni T., Gallo E., 2005, Ap&SS, 300, 1
Fender R. P., Belloni T. M., Gallo E., 2004, MNRAS, 355, 1105
Fender R. P., Homan J., Belloni T. M., 2009, MNRAS, 396, 1370
Feroci M., Matt G., Pooley G., Costa E., Tavani M., Belloni T., 1999, A&A, 351, 985
Fragile P. C., Blaes O. M., 2008, ApJ, 687, 757
Fragile P. C., Blaes O. M., Anninos P., Salmonson J. D., 2007, ApJ, 668, 417
Fragile P. C., Mathews G. J., Wilson J. R., 2001, ApJ, 553, 955
Frank J., King A., Raine D. J., 2002, Accretion Power in Astrophysics: Third Edition. p. 398
Gehrels N. et al., 2004, ApJ, 611, 1005
George I. M., Fabian A. C., 1991, MNRAS, 249, 352
Gierliński M., Done C., 2003, MNRAS, 342, 1083
Gierliński M., Zdziarski A. A., Poutanen J., Coppi P. S., Ebisawa K., Johnson W. N., 1999, MNRAS, 309, 496
Gies D. R. et al., 2003, ApJ, 583, 424
Gilfanov M., 2010, in Lecture Notes in Physics, Berlin Springer Verlag, Vol. 794, Lecture Notes in Physics, Berlin Springer Verlag, Belloni T., ed., p. 17
Gilfanov M., Churazov E., Revnivtsev M., 1999, A&A, 352, 182
Gilfanov M., Churazov E., Revnivtsev M., 2000, in Proceedings of 5-th Sino-German workshop on Astrohpysics, 1999, Eds. Gang Zhao, Jun-Jie Wang, Hong Mei Qiu and Gerhard Boerner, SGSC Conference Series, vol.1, pp.114-123, pp. 114–123
Grinberg V. et al., 2013, A&A, 554, A88
Heil L. M., Vaughan S., Uttley P., 2012, MNRAS, 422, 2620
Henisey K. B., Blaes O. M., Fragile P. C., 2012, ApJ, 761, 18
Homan J., Wijnands R., van der Klis M., Belloni T., van Paradijs J., Klein-Wolt M., Fender R., Méndez M., 2001, ApJS, 132, 377
Ingram A., Done C., 2010, MNRAS, 405, 2447
Ingram A., Done C., 2011, MNRAS, 415, 2323

Ingram A., Done C., 2012, MNRAS, 419, 2369
Ingram A., Done C., Fragile P. C., 2009, MNRAS, 397, L101
Ingram A., van der Klis M., 2013, MNRAS, 434, 1476
Ingram A., van der Klis M., Middleton M., Done C., Altamirano D., Heil L., Uttley P., Axelsson M., 2016, MNRAS, 461, 1967
Ingram A. R., 2016, Astronomische Nachrichten, 337, 385
Jahoda K., Swank J. H., Giles A. B., Stark M. J., Strohmayer T., Zhang W., Morgan E. H., 1996, in Proc. SPIE, Vol. 2808, EUV, X-Ray, and Gamma-Ray Instrumentation for Astronomy VII, Siegmund O. H., Gummin M. A., eds., pp. 59–70
Kalamkar M., Homan J., Altamirano D., van der Klis M., Casella P., Linares M., 2011, ApJ, 731, L2
Kalamkar M., Reynolds M. T., van der Klis M., Altamirano D., Miller J. M., 2015a, ApJ, 802, 23
Kalamkar M., van der Klis M., Heil L., Homan J., 2015b, ApJ, 808, 144
Kalamkar M., van der Klis M., Uttley P., Altamirano D., Wijnands R., 2013, ApJ, 766, 89
Kalberla P. M. W., Burton W. B., Hartmann D., Arnal E. M., Bajaja E., Morras R., Pöppel W. G. L., 2005, A&A, 440, 775
King A., Nixon C., 2016, MNRAS, 462, 464
Klein Wolt M., 2004, PhD thesis, University of Amsterdam
Kolehmainen M., Done C., Díaz Trigo M., 2011, MNRAS, 416, 311
Kotov O., Churazov E., Gilfanov M., 2001, MNRAS, 327, 799
Kubota A., Done C., 2004, MNRAS, 353, 980
Kuulkers E. et al., 2013, A&A, 552, A32
Leahy D. A., Darbro W., Elsner R. F., Weisskopf M. C., Kahn S., Sutherland P. G., Grindlay J. E., 1983, ApJ, 266, 160
Levine A. M., Bradt H., Cui W., Jernigan J. G., Morgan E. H., Remillard R., Shirey R. E., Smith D. A., 1996, ApJ, 469, L33
Liu S., Melia F., 2002, ApJ, 573, L23
Lubow S. H., Ogilvie G. I., Pringle J. E., 2002, MNRAS, 337, 706
Lyubarskii Y. E., 1997, MNRAS, 292, 679
Maccarone T. J., Coppi P. S., Poutanen J., 2000, ApJ, 537, L107
Mangano V., Hoversten E. A., Markwardt C. B., Sbarufatti B., Starling R. L. C., Ukwatta T. N., 2010, GRB Coordinates Network, 11296
Martin R. G., Tout C. A., Pringle J. E., 2008, MNRAS, 387, 188
Matsuoka M. et al., 2009, PASJ, 61, 999
McClintock J. E., Remillard R. A., 2006, Black hole binaries, Lewin W. H. G., van der Klis M., eds., pp. 157–213
Melia F., Misra R., 1993, ApJ, 411, 797
Merloni A., Fabian A. C., Ross R. R., 2000, MNRAS, 313, 193
Merloni A., Fabian A. C., Ross R. R., 2001, X-ray Astronomy: Stellar Endpoints, AGN, and the Diffuse X-ray Background, 599, 770

Miller-Jones J. C. A., Tzioumis A. K., Jonker P. G., Sivakoff G. R., Maccarone T. J., Nelemans G., 2011, The Astronomer's Telegram, 3364
Mirabel I. F., Rodrigues I., 2003, Science, 300, 1119
Misra R., 2000, ApJ, 529, L95
Mitsuda K. et al., 1984, PASJ, 36, 741
Miyamoto S., Kimura K., Kitamoto S., Dotani T., Ebisawa K., 1991, ApJ, 383, 784
Miyamoto S., Kitamoto S., 1989, Nature, 342, 773
Miyamoto S., Kitamoto S., Iga S., Kamodo Y., Hayashida K., Terada K., Negoro H., 1993, in Plasma Physics and Controlled Nuclear Fusion (ITC-4), Guyenne H. T. D., Hunt J. J., eds.
Miyamoto S., Kitamoto S., Mitsuda K., Dotani T., 1988, Nature, 336, 450
Muñoz-Darias T., Coriat M., Plant D. S., Ponti G., Fender R. P., Dunn R. J. H., 2013, MNRAS, 432, 1330
Muñoz-Darias T., Motta S., Stiele H., Belloni T. M., 2011, MNRAS, 415, 292
Muno M. P., Morgan E. H., Remillard R. A., 1999, ApJ, 527, 321
Mushtukov A., Ingram A., van der Klis M., in prep.
Narayan R., Yi I., 1995, ApJ, 452, 710
Negoro H. et al., 2011, The Astronomer's Telegram, 3330
Nolan P. L. et al., 1981, ApJ, 246, 494
Nowak M. A., 1995, PASP, 107, 1207
Nowak M. A., 2000, MNRAS, 318, 361
Nowak M. A., Dove J. B., Vaughan B. A., Wilms J., Begelman M. C., 1999a, Nuclear Physics B Proceedings Supplements, 69, 302
Nowak M. A., Wilms J., Dove J. B., 1999, ApJ, 517, 355
Nowak M. A., Wilms J., Vaughan B. A., Dove J. B., Begelman M. C., 1999b, ApJ, 515, 726
Pottschmidt K. et al., 2003, A&A, 407, 1039
Press W. H., Teukolsky S. A., Vetterling W. T., Flannery B. P., 1992, Numerical recipes in FORTRAN. The art of scientific computing
Rapisarda S., Ingram A., Kalamkar M., van der Klis M., 2016, MNRAS, 462, 4078
Rapisarda S., Ingram A., van der Klis M., 2014, MNRAS, 440, 2882
Reig P., Papadakis I., Kylafis N. D., 2002, A&A, 383, 202
Remillard R. A., McClintock J. E., 2006, ARA&A, 44, 49
Remillard R. A., Muno M. P., McClintock J. E., Orosz J. A., 2002, ApJ, 580, 1030
Repetto S., Davies M. B., Sigurdsson S., 2012, MNRAS, 425, 2799
Revnivtsev M., Churazov E., Postnov K., Tsygankov S., 2009, A&A, 507, 1211
Reynolds M. T., Miller J. M., 2013, ApJ, 769, 16
Rothschild R. E. et al., 1998, ApJ, 496, 538
Shakura N. I., Sunyaev R. A., 1973, A&A, 24, 337
Smith D. A., 1998, IAU Circ., 7008
Sobczak G. J., McClintock J. E., Remillard R. A., Cui W., Levine A. M., Morgan E. H., Orosz J. A., Bailyn C. D., 2000, ApJ, 544, 993
Sowers J. W., Gies D. R., Bagnuolo W. G., Shafter A. W., Wiemker R., Wiggs M. S., 1998,

ApJ, 506, 424
Stella L., Vietri M., 1998, ApJ, 492, L59
Stiele H., Muñoz-Darias T., Motta S., Belloni T. M., 2012, MNRAS, 422, 679
Sunyaev R. A., Titarchuk L. G., 1980, A&A, 86, 121
Sunyaev R. A., Truemper J., 1979, Nature, 279, 506
Svensson R., Zdziarski A. A., 1994, ApJ, 436, 599
Tananbaum H., Gursky H., Kellogg E., Giacconi R., Jones C., 1972, ApJ, 177, L5
Tetarenko B. E., Sivakoff G. R., Heinke C. O., Gladstone J. C., 2016, ApJS, 222, 15
Thorne K. S., Price R. H., 1975, ApJ, 195, L101
Timmer J., Koenig M., 1995, A&A, 300, 707
Titarchuk L., 1994, ApJ, 434, 570
Tomsick J. A. et al., 2014, ApJ, 780, 78
Uttley P., McHardy I. M., 2001, MNRAS, 323, L26
Uttley P., McHardy I. M., Vaughan S., 2005, MNRAS, 359, 345
van der Klis M., 1989, in NATO Advanced Science Institutes (ASI) Series C, Vol. 262, NATO Advanced Science Institutes (ASI) Series C, Ögelman H., van den Heuvel E. P. J., eds., p. 27
van der Klis M., 1995, in NATO Advanced Science Institutes (ASI) Series C, Vol. 450, NATO Advanced Science Institutes (ASI) Series C, Alpar M. A., Kiziloglu U., van Paradijs J., eds., p. 301
van der Klis M., 2004, ArXiv Astrophysics e-prints
van der Klis M., Hasinger G., Stella L., Langmeier A., van Paradijs J., Lewin W. H. G., 1987a, ApJ, 319, L13
van der Klis M., Stella L., White N., Jansen F., Parmar A. N., 1987b, ApJ, 316, 411
Vaughan B. A., Nowak M. A., 1997, ApJ, 474, L43
Vaughan S., Uttley P., Pounds K. A., Nandra K., Strohmayer T. E., 2011, MNRAS, 413, 2489
Veledina A., 2016, ApJ, 832, 181
Walton D. J. et al., 2013, ApJ, 777, L23
Wijnands R., Homan J., van der Klis M., 1999, ApJ, 526, L33
Wijnands R., van der Klis M., 1998, ApJ, 507, L63
Wilkinson T., Uttley P., 2009, MNRAS, 397, 666
Wilms J., Allen A., McCray R., 2000, ApJ, 542, 914
Wilson C. D., Done C., 2001, MNRAS, 325, 167
Zdziarski A. A., Johnson W. N., Magdziarz P., 1996, MNRAS, 283, 193
Zdziarski A. A., Lubiński P., Smith D. A., 1999, MNRAS, 303, L11
Zdziarski A. A., Poutanen J., Paciesas W. S., Wen L., 2002, ApJ, 578, 357
Zhang W., Jahoda K., Swank J. H., Morgan E. H., Giles A. B., 1995, ApJ, 449, 930
Życki P. T., Done C., Smith D. A., 1999, MNRAS, 309, 561


B

Reference list

The bibliographic information of the chapters in this thesis is summarized below. For each chapter, the relative importance of the co-authors is indicated by the order of the author list.

1. **S. Rapisarda**, A. Ingram and M. van der Klis
   Evolution of the hot flow of MAXI J1543-564 (**Chapter 2**)
   Monthly Notices of the Royal Astronomical Society, Volume 440, 2882 (2014)

2. **S. Rapisarda**, A. Ingram, M. Kalamkar and M. van der Klis
   Modelling the cross-spectral variability of the black hole binary MAXI J1659-152 with propagating accretion rate fluctuations (**Chapter 3**)[2]
   Monthly Notices of the Royal Astronomical Society, Volume 462, 4078 (2016)

3. **S. Rapisarda**, A. Ingram and M. van der Klis
   Cross-spectral modelling of the black hole X-ray binary XTE J1550-564: challenges to the propagating fluctuations paradigm (**Chapter 4**)
   Submitted for publication to Monthly Notices of the Royal Astronomical Society

4. **S. Rapisarda**, A. Ingram and M. van der Klis
   Modelling hard and soft state of Cygnus X-1 with propagating mass accretion rate fluctuations (**Chapter 5**)
   Submitted for publication to Monthly Notices of the Royal Astronomical Society

[2]Chapter 3 differs from the paper published on MNRAS in the computed χ^2 values and P_F probability (see Chapter 3, Tab. 3.1). The reason for this difference is a bug in the code that affected the computation of these quantities. The corrected χ^2 values are smaller than the previous values (so the goodness of our fits was initially underestimated). The corrected χ^2 and P_F values do not affect our conclusions. An *erratum* with the corrected values will be sent to MNRAS. The rest of Chapter 3 is identical to the published paper.


R

Summary

This thesis presents applications of mass accretion rate fluctuations models on black hole X-ray binaries. Black hole X-ray binaries are systems consisting of a star, like the Sun, orbiting around a stellar mass black hole. Black holes are *compact objects*. This means that their mass is concentrated in a very small amount of space (a black hole of 10 Solar masses has a diameter of about 30 km). Black holes are the final stage of the evolution of massive stars (about 25 times the mass of the Sun) and their compactness is the result of an unstoppable gravitational collapse. Indeed, when a massive star exhausts the fuel for nuclear burning, the internal pressure can no longer support the layers of the star. The star collapses because of

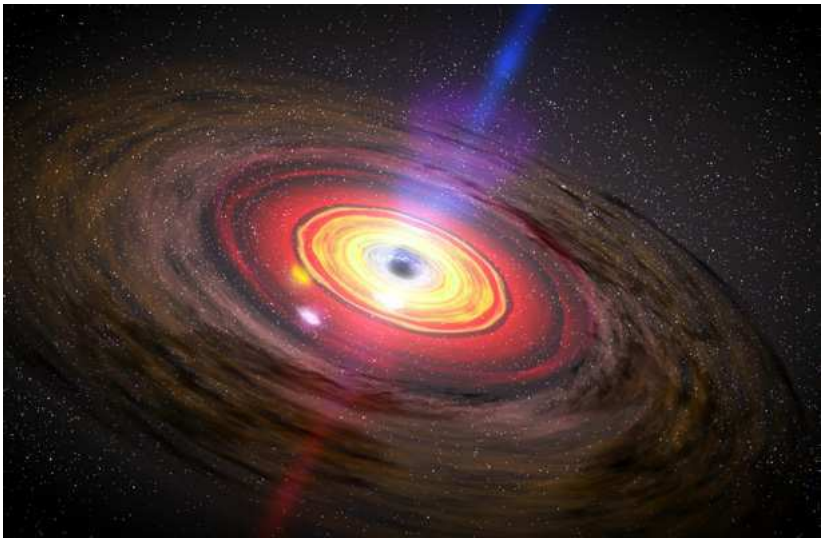

Figure A: Artistic impression of an accretion flow around a black hole. Credit: NASA/Dana /Berry, Sky Works Digital

gravity and, if the core of the star is massive enough (≈ 3 $M_\odot$), there is no force in Nature able to prevent the collapse. The core of the star is squeezed into a single point, the *singularity*, and the star becomes a (stellar mass) black hole.
A black hole has no solid surface, but a virtual boundary called the "event horizon". Inside the event horizon, spacetime is distorted such that even light cannot escape. As a result, events happening inside the horizon cannot be detected by any observer outside of it. Because of their nature (they are very small objects and they do not emit amounts of radiation like emitted by a normal star), stellar mass black holes are difficult to detect. However, they can affect the surrounding environment and their compactness can turn their surroundings into very efficient radiators.
A black hole can be part of a binary system and accrete material from its companion star. The outer layers of the companion star are ripped off by the black hole gravitational attraction and, "falling" onto the black hole, they form an accretion disc around it (see Fig. A). Spiraling towards the black hole, the material in the disc becomes so hot that the flux of the entire system is dominated by X-ray radiation (that is the reason why we refer to these systems as *Black Hole X-ray Binaries*, BHBs). No other region in the universe is like that close to a stellar mass black hole. Effects of general relativity become important. Studying the emission coming from the accretion flow is the key to investigate the behavior of matter in "extreme" conditions and, ultimately, to test predictions of general relativity.
During an outburst, i.e., a period of enhanced accretion lasting from weeks to months, BHBs show variability on both long and short timescales. In this thesis I focused on the short timescale (or rapid) variability (i.e., luminosity fluctuations on timescale from ms to hundreds of seconds). This variability carries information about the region close to the event horizon.

Although the short timescale variability of BHBs has been studied for more than 40 years, its origin is still a matter of debate. One of the physical scenarios that can explain the short timescale variability is *propagating mass accretion rate fluctuations* in the accretion flow (see Fig. B). According to this model, accretion takes place though an optically thin hot flow surrounded by a truncated optically thick accretion disc (*truncated disc model*). The transition between these two regimes occurs at the truncation radius. At each radius of the hot flow, the mass accretion rate (the amount of material accreted per second) stochastically deviates from its average value. The duration of these perturbations (or fluctuations) depends on the radius: fluctuations last longer at large radii and shorter at small radii. These fluctuations propagate towards the black hole, so that each radius of the flow experiences both local fluctuations and fluctuations propagating from large radii. Finally, depending on the emissivity at each radius, fluctuations in mass accretion rate cause luminosity variations in different energy bands. In previous studies, the propagating fluctuations scenario has been claimed to explain many of the rapid variability characteristics observed in BHBs. However, at present, this kind of model has been quantitatively applied on a very small number of sources and observations. In this thesis, in order to test the validity of the propagating fluctuations scenario, we systematically and quantitatively applied the propagating fluctuations model PROPFLUC to four

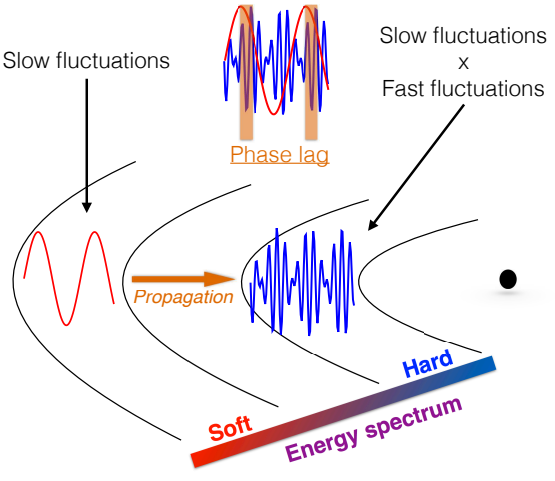

Figure B: Sketch of the propagating mass accretion rate fluctuations mechanism

BHBs. In addition to the propagation of fluctuations, PROPFLUC assumes that the entire hot flow precesses because of frame dragging (Lense-Thirring precession). This precession adds a quasi periodic oscillation (QPO) to the signal (one of the main observables in BHB rapid variability). In Chapter 2 we applied the model PROPFLUC to the black hole candidate MAXI J1543-564. We analyzed the source during the rising phase of its 2011 outburst (hard state) using RXTE data. In particular, we fitted the power spectrum of the source in a single energy band ($\approx$ 3-20 keV) using both a canonical approach (multi-Lorentzian fit) and PROPFLUC. Model predictions showed good agreement with the data and we traced the evolution of the outburst in terms of physical parameters (surface density, truncation radius, and fractional variability).

In a propagating fluctuations scenario, if we consider two different radii of the accretion flow, they both are characterized by slow mass accretion rate fluctuations. Because fluctuations propagate through the accretion flow on a finite timescale, the slow fluctuations that we observe a small radii have a *delay* compared to the ones stirred up at large radii (see Fig. B). If the energy spectrum hardens towards the black hole, we would then expect a *phase lag* between hard and soft band, with the hard emission lagging the soft emission. In order to quantitatively test the phase lag predicted by the model, we updated the code to produce simultaneously the power spectrum in two energy bands and the cross-spectrum (so the phase lag) between these two bands. We also updated PROPFLUC to take into account fluctuations propagating through the optically thick disc into the hot flow. BHBs can show quite complex spectral shapes and previous studies showed the evidence of variability originating from the disc. With the additional assumption of fluctuations propagating from the disc, PROPFLUC can produce more complex power spectral shapes than fluctuations propagating only in the hot flow. Having extended the fitting capabilities of the model, in Chapter 3 we tested this

new version of the code on the black hole MAXI J1659-152 during the rising phase of its 2010 outburst (hard state). In our analysis we used *Swift* data (0.5 - 2.0 keV) to study the source from the very beginning of the outburst and to detect disc (low energy) emission. We fitted 11 observations of the source and, also in this case, we obtained good agreement between model predictions and data. We found that the hypothesis of fluctuations propagating from the disc is statistically justified for most of the observations. We also compared the truncation radius estimated from spectral and timing (with PROPFLUC) analysis. We found that, contrary to the timing results, the estimation from spectral fitting is not consistent with the observed light curve.

Although the results of our previous study were in accordance with the propagating fluctuations model, the quality of the *Swift* data was not sufficient to test the PROPFLUC phase lag predictions well. We therefore performed a more stringent test (Chapter 4) selecting two high quality RXTE observations of the black hole XTE J1550-564 in the hard state (1998 outburst). We also further updated the model in order to take into account damping, different fluctuation propagation speeds, and extra variability in the hot flow (producing the most sophisticated propagating fluctuations model to date). In this case, the model predictions showed important qualitative and quantitative discrepancies with the data. In particular, in the first observation the model could not predict the observed phase lag profile and in the second observation the model failed to reproduce both the power spectral shape in the soft and hard band and the phase lag amplitude. In order to explain these discrepancies we discussed several scenarios not included in the model (reflection, non-linear variations, etc). In particular, we concluded we could not exclude the possibility that the physical mechanism producing the QPO observed in the data also affects the broad band variability in a way that is not taken into account in the model. Contrary to XTE J1550-564, Cygnus X-1 does not show significant sharp QPOs. Previous studies showed that some soft state observations of this source are compatible with the propagating fluctuations scenario. Chapter 5 is dedicated to the analysis of three Cygnus X-1 RXTE observations (in the hard, soft, and intermediate state). In the soft state we found that, assuming a very large variable hot flow and a stable disc, the model predictions agree with data. The result is compatible with a "sandwich" geometry, where the optically thick disc is sandwiched by the optically thin hot flow (as already suggested in previous studies). The hard state observation has an energy spectrum that is very similar to the first observation analyzed in Chapter 4. In this case, we obtained a reasonably good fit assuming a truncated disc geometry. This hard state observation does not show any QPO and, interestingly, the surface density profile in the hot flow obtained from our fit does not show any sharp transition such as observed in XTE J1550-564. These two observational facts may be jointly explained by the spin of the black hole in Cygnus X-1 being aligned with the spin of the binary system. Finally, we could not obtain a statistically acceptable fit for the transition between soft and hard state.

What we have found is that the joint analysis of power spectra in different energy bands and the cross-spectra between those bands provides very much stronger constrains on the physical models than does fitting subsets of the observational information, such as just power spectra

or just time lags. Our analysis revealed that by itself the propagating fluctuations paradigm cannot always quantitatively explain the rapid variability. However, our results do suggest that propagating fluctuations are an important ingredient in the physical processes producing the variability of black hole accretion flows.


S

Samenvatting

Dit werk toetst modellen die een beschrijving geven van variaties in de *massa-accretiesnelheid* (de hoeveelheid materie die per tijdseenheid op een zwart gat valt) aan waarnemingen van röntgen dubbelstersystemen. Röntgen dubbelstersystemen bestaan uit een zonachtige ster en een *compact object* die om een gemeenschappelijk zwaartepunt draaien dat dichtbij het compacte object ligt. Een zwart gat is een voorbeeld van een compact object; zijn massa is geconcentreerd in een zeer klein volume (een zwart gat dat 10 keer zo zwaar is als de zon past bijvoorbeeld in een bol met een diameter van 30 km). Zwarte gaten zijn het evolutionaire eindstadium van zeer zware sterren (ongeveer 25 keer de massa van de zon), en

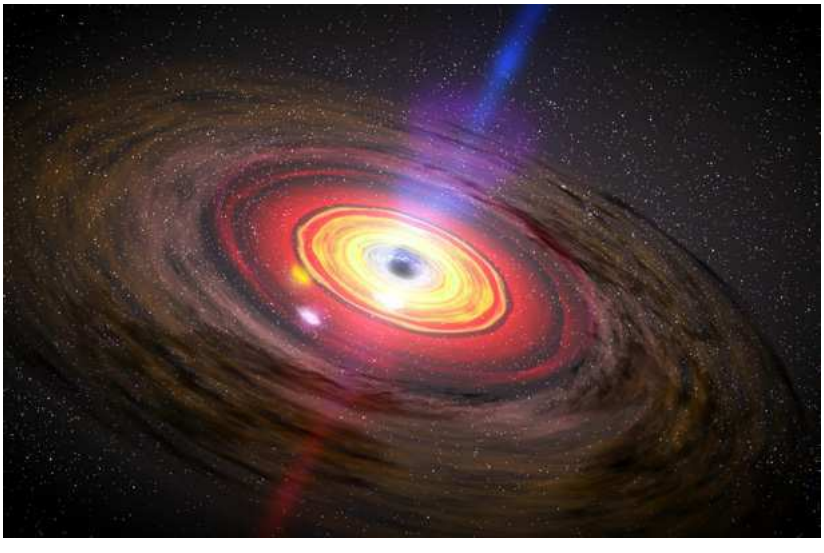

Figuur A: Artistieke impressie van accretieschijf rond een zwart gat. Credit: NASA/Dana /Berry, Sky Works Digital

hun hoge dichtheid is het resultaat van een onomkeerbare ineenstorting ten gevolge van de zwaartekracht. Wanneer een zware ster zijn brandstof voor nucleaire fusieprocessen heeft verbruikt, zullen door de wegvallende druk de buitenste lagen van de ster niet langer ondersteund worden; een ineenstorting is onvermijdelijk. Als de kern van de ster zwaar genoeg is (meer dan drie maal de massa van de zon) zal geen enkele natuurkracht opgewassen zijn tegen de zwaartekracht. De kern van de ster wordt dan samengeperst in een punt, *de singulariteit*, en de ster verandert in een zwart gat.
Een zwart gat heeft geen tastbaar oppervlak, maar een virtuele bolschil die "de waarnemingshorizon" wordt genoemd. Binnen de schil is de ruimtetijd dermate vervormd, dat zelfs licht niet kan ontsnappen. Deze eigenschap leidt ertoe dat gebeurtenissen binnen de waarnemingshorizon niet gecommuniceerd kunnen worden naar een waarnemer die zich buiten de horizon bevindt.
Zwarte gaten zijn moeilijk te detecteren omdat ze zo klein zijn en nauwelijks stralen. Ze kunnen daarentegen de omringende ruimtetijd sterk vervormen doordat ze zo compact zijn. Die vervorming kan er voor zorgen dat een zwart gat indirect toch zichtbaar wordt voor een waarnemer. In een dubbelstersyteem met een donorster, die zonachtig kan zijn, wordt gas van het oppervlak van de ster dat voldoende dichtbij komt van de ster afgetrokken richting het zwarte gat. Het "vallende" gas kan door het behoud van impulsmoment niet direct in het gat vallen, maar vormt een accretieschijf (zie Fig. A). Tijdens het vallen wordt het gas in de schijf zo warm, dat het röntgenstraling uit gaat zenden (dit is de reden dat we deze systemen *röntgen dubbelstersystemen*, BHBs, noemen). Er is geen andere plek in het heelal die lijkt op de ruimte rond een zwart gat. Effecten beschreven door algemene relativiteitstheorie spelen hier naar verwachting een grote rol. Het bestuderen van röntgenstraling afkomstig van accretieschijven rond zwarte gaten stelt ons in staat het gedrag van materie onder extreme omstandigheden te bestuderen, en om uiteindelijk de voorspellingen van de algemene relativiteitstheorie te toetsen.
Tijdens een uitbarsting, in casu een periode van vermeerderde accretie die ongeveer weken to maanden duurt, zijn BHBs variabel over zowel lange en korte tijdschalen. In deze thesis heb ik me gericht op de variabiliteit over korte tijdschalen, oftewel snelle variabiliteit (dat wil zeggen fluctuaties in de lichtsterkte op een tijdschaal van milli- tot enkele honderden seconden). Deze variabiliteit herbergt informatie over het gebied dichtbij de waarnemingshorizon.

Hoewel de korte-tijdschaalvariabiliteit al meer dan 40 jaar wordt bestudeerd, is de oorsprong ervan nog altijd een punt van discussie. Een van de fysische scenario's die korte-tijdschaalvariabiliteit zouden kunnen verklaren is het fenomeen van *fluctuaties van de massa-accretiesnelheid* die zich voortplanten doorheen de accretiestroom (zie Fig. B). Volgens dit model vindt accretie plaats door middel van een optisch dunne hete stroming omringd door een afgeknotte optisch dikke accretieschijf (*het afgeknotte schijf-model*). De overgang tussen deze twee regimes doet zich voor op de zogeheten afknottingsstraal. De massa-accretiesnelheid wijkt langs de straal van de hete stroming stochastisch af van de gemiddelde waarde. De duur van deze perturbaties (of fluctuaties) hangt af van de straal: de fluctuaties duren langer op grotere afstanden en korter op een kleinere straal. Deze fluctuaties planten

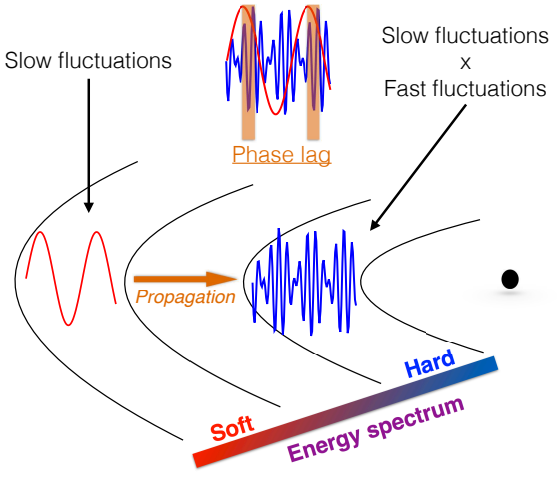

Figuur B: Schets van het propagerende flucuaties scenario

zich voort richting het zwarte gat, zo dat op elke straal de stroming zowel fluctuaties van lokale oorsprong ondervindt als fluctuaties afkomstig van grotere afstanden. Ten slotte veroorzaken de fluctuaties in de massa-accretiesnelheid, afhankelijk van de emissiviteit op elke straal, variaties in de lichtsterkte in verschillende energiebanden. In voorgaande onderzoeken wordt beweerd dat vele van de geobserveerde snelle variabiliteitseigenschappen in BHB's, kunnen worden verklaard met het 'propagerende fluctuaties scenario'. Op dit moment echter, is slechts op een zeer beperkt aantal bronnen en observaties dit soort model quantitatief toegepast geweest. Om de validiteit van het propagerende fluctuaties-scenario te testen, hebben we in deze thesis het propagerende fluctuatie-model PROPFLUC systematisch en quantitatief toegepast op vier BHBs. Naast de voorplanting van de fluctuaties, veronderstelt PROPFLUC dat de volledige hete stroming een precessiebeweging ondergaat vanwege 'frame dragging', ook wel het Lense-Thirring effect genoemd. Deze precessie voegt een quasi-periodieke oscillatie (QPO) toe aan het signaal (een van de voornaamste observabelen in snelle variabiliteit van BHBs). In hoofdstuk 2 passen we het PROPFLUC model toe op het mogelijke zwarte gat MAXI J1543-564. We hebben deze bron geanalyseerd voor de stijgende fase van zijn uitbarsting in 2011 (de harde toestand), daarbij gebruikmakend van RXTE data. In het bijzonder hebben we het power spectrum van deze bron gefit in een enkele energieband ($\approx$ 3-20 keV), gebruikmakend van zowel de klassieke benadering (een multi-Lorenzische fit) en PROPFLUC. Voorspellingen van het model toonden een goede overeenkomst met de gegevens en we volgden de evolutie van de uitbarsting in termen van zijn fysische parameters (d.w.z. oppervlakte dichtheid, afknottingsstraal en verhoudingsgewijze variabiliteit).

Wanneer we in het kader van het propagerende fluctuaties-scenario twee verschillende stralen beschouwen in de accretiestroom, dan wordt de stroom op beide punten gekarakteriseerd door een trage fluctuaties in de massa-accretiesnelheid. Omdat de fluctuaties zich binnen

een eindig tijdsbestek door de accretiestroom voortplanten, zijn de trage fluctuaties die we waarnemen van een kleinere straal *vertraagd* ten opzichte van degene die zijn ontstaan op een grotere straal (see Fig. B). Als het energiespectrum verhardt richting het zwarte gat, dan verwachten we een faseverschil tussen de harde en zachte componenten; waarbij de harde emissie vertraagd is ten opzichte van de zachte emissie. Om dit faseverschil - dat door het model wordt voorspeld - kwantitatief te testen, hebben we de code bijgewerkt zodat we tegelijkertijd het powerspectrum in twee energiebanden en het cross-spectrum (en dus het faseverschil) tussen deze energiebanden kunnen reproduceren. We hebben PROPFLUC bijgewerkt zodanig dat het ook de fluctuaties die propageren van de optisch dikke schijf richting de hete stroming in acht neemt. BHBs kunnen complexe spectrale vormen opleveren en voorgaande studies hebben bewijs geleverd voor variabiliteit in de schijf. In combinatie met de extra aanname dat de fluctuaties zich voortplanten in de schijf kan PROPFLUC complexere spectra genereren dan wanneer er enkel gekeken wordt naar fluctuaties die zich voortplanten in de hete stroming. Na de fitmogelijkheden van het model te hebben uitgebreid, hebben we in Hoofdstuk 3 deze nieuwe versie getest op het zwarte gat MAXI J1659-152 tijdens de stijgende fase van zijn uitbarsting in 2010 (de harde toestand). We maakten gebruik van *Swift* data (0.5 - 2.0 keV) om de uitbarsting van de bron vanaf het allereerste begin te bestuderen en om (laag-energetische) emissie van de schijf te detecteren. We hebben 11 observaties gefit en verkregen goede overeenkomsten tussen het model en de data. De hypothese over propagerende fluctuaties in de schijf bleek statistisch gerechtvaardigd voor het merendeel van de observaties. We hebben eveneens de waardes voor de afknottingsstraal vergeleken, verkregen met behulp van spectrale en temporale analyse technieken. In tegenstelling tot de resultaten van de temporale analyse, vonden we dat de waarde verkregen via het fitten van de spectra niet consistent is met de waargenomen lichtcurve.

Hoewel de resultaten van de vorige studie consistent waren met het propagerende fluctuatiemodel, was de kwaliteit van de *Swift* data niet voldoende om de faseverschilvoorspellingen van PROPFLUC te testen. We hebben daarom een meer nauwgezette test uitgevoerd (Hoofdstuk 4), waarbij we twee hoge-kwaliteit RXTE observaties hebben geselecteerd van het zwarte gat XTE J1550-564 in de harde toestand (1998 uitbarsting). Daarnaast hebben we de code verder uitgebreid zodat deze demping, verschillende voortplantingssnelheden van de fluctuaties en extra variabiliteit in de hete stroming in acht neemt (resulterend in het meest geavanceerde propagerende fluctuatie-model tot nog toe). In dit geval concludeerden we dat de voorspellingen van het model belangrijke kwalitatieve en kwantitatieve discrepanties vertoont ten opzichte van de data. In het bijzonder slaagde het model er niet in het profiel van het geobserveerde faseverschil te voorspellen voor de eerste observatie; en voor de tweede observatie faalde het model in het reproduceren van zowel de vorm van het powerspectrum in de zachte en harde (energie)band, als de amplitude van het faseverschil. Om deze discrepanties te verklaren bespraken we enkele scenarios welke niet zijn opgenomen in het model (reflectie, non-lineaire variaties, et cetera). In het bijzonder concludeerden we dat we niet de konden uitsluiten dat het fysisch mechanisme welke de QPO veroorzaakt, ook invloed heeft op de breed band variabiliteit, op een manier die niet model door het model wordt beschre-

ven. In tegenstelling tot XTE J1550-564, toont Cygnus X-1 geen significante scherpe QPOs. Voorgaande studies toonden dat sommige observaties in de zachte toestand van deze bron in overeenstemming zijn met het propagerende fluctuaties-scenario. Hoofdstuk 5 is gewijd aan de analyse van drie Cygnus X-1 RXTE observaties (in de harde, de zachte, en de tussenliggende toestand). In de zachte toestand zagen we dat, onder de veronderstelling dat er een zeer grote variabele hete stroming aanwezig is en een stabiele schijf, de voorspellingen van het model overeenkomen met de data. Het resultaat is consistent met de "sandwich" geometrie, waarbij de optisch dikke schijf omsloten wordt door de optisch dunne hete stroming (wat ook gesuggereerd wordt in voorgaande studies). De observatie van de harde toestand heeft een energiespectrum dat bijzonder goed overeenkomt met de eerste observatie die in Hoofdstuk 4 is geanalyseerd. In dit geval vonden we een redelijk goede fit, gegeven de aanname dat de geometrie dat van een afgeknotte schijf is. In deze observatie (van de harde toestand) vinden we echter geen QPO en bovendien toont het oppervlaktedichtheidsprofiel in de hete stroming, welke voortkomt uit de onze fit, geen scherpe transitie zoals is waargenomen voor XTE J1550-564. Deze twee feiten uit waarnemingen zijn mogelijk gezamenlijk te verklaren door het feit dat de spin van het zwarte gat in Cygnus X-1 in dezelfde richting draait als de spin van het dubbelstersysteem. Tot slot, waren we niet in staat om een statistisch acceptabele fit te verkrijgen voor de transitie tussen de zachte en harde toestand.

Wat we gevonden hebben is dat het simultaan analyseren van de powerspectra in verschillende energiebanden en de cross-spectra tussen deze banden de fysische modellen beter kan aanscherpen, dan dat het fitten van subgroepen van waarnemingen, zoals enkel powerspectra of enkel tijdsverschilmetingen. Onze analyse heeft onthuld dat het propagerende fluctuatiesparadigma op zich niet altijd de snelle variabiliteit kwantitatief kan verklaren. Echter, onze resultaten suggereren wel dat de propagerende fluctuaties een belangrijk onderdeel zijn van het fysische proces dat de variabiliteit in de accretiestromen van een zwart gat voortbrengt.